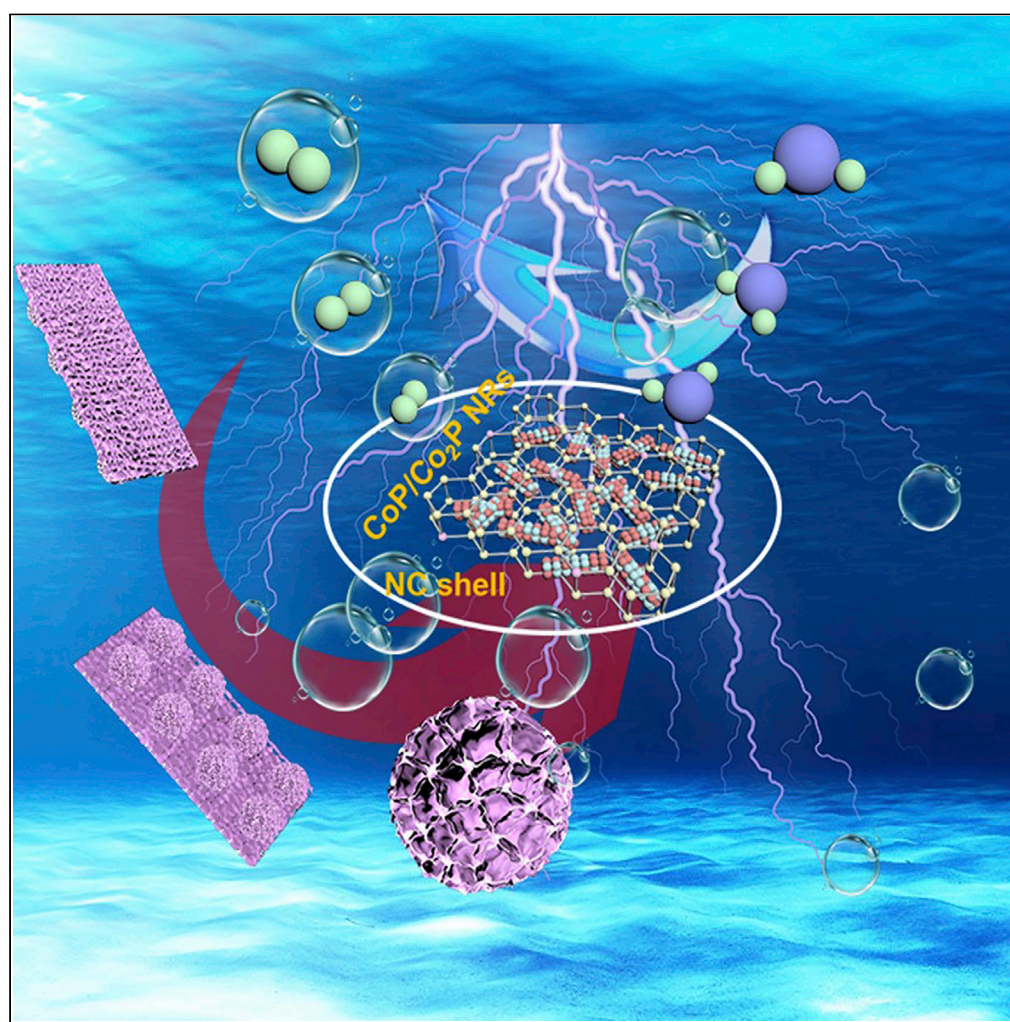


Article

Ultrafine CoP/Co₂P Nanorods Encapsulated in Janus/Twins-type Honeycomb 3D Nitrogen-Doped Carbon Nanosheets for Efficient Hydrogen Evolution

Baocang Liu, Bo Cao, Yan Cheng, ..., Xiaolei Sun, Yaping Du, Jun Zhang

nmjp219@163.com (P.J.)
gaorui@imu.edu.cn (R.G.)
ypdu@nankai.edu.cn (Y.D.)
cejzhang@imu.edu.cn (J.Z.)

HIGHLIGHTS

A nitride-hydroxide cobalt is reported as precursor for CoP/Co₂P@NC/Ti electrode

Janus- or twins-type morphology of CoP/Co₂P@NC/Ti electrode can be well controlled

The Janus-type CoP/Co₂P@NC/Ti electrode exhibits very low overpotential for HER

Coupling effects between CoP/Co₂P and NC matrix contributes to enhanced performance

Liu et al., iScience 23, 101264
July 24, 2020 © 2020 The Authors.
<https://doi.org/10.1016/j.isci.2020.101264>

Article

Ultrafine CoP/Co₂P Nanorods Encapsulated in Janus/Twins-type Honeycomb 3D Nitrogen-Doped Carbon Nanosheets for Efficient Hydrogen EvolutionBaocang Liu,^{1,6} Bo Cao,^{1,6} Yan Cheng,¹ Peng Jing,^{1,*} Jian Zhao,³ Rui Gao,^{1,*} Anthony. O'Mullane,⁴ Huaiyong Zhu,⁴ Kaiqiang Liu,⁵ Xiaolei Sun,² Yaping Du,^{2,7,*} and Jun Zhang^{1,*}

SUMMARY

In this study, we report a Janus- or twins-type honeycomb 3D porous nitrogen-doped carbon (NC) nanosheet array encapsulating ultrafine CoP/Co₂P nanorods supported on Ti foil (CoP/Co₂P@NC/Ti) as a self-supported electrode for efficient hydrogen evolution. The synthesis and formation mechanism of 3D porous NC nanosheet array assembled into a honeycomb layer with ultrafine CoP/Co₂P single-crystal nanorods encapsulated is systematically presented. The CoP/Co₂P@NC/Ti electrode exhibits low overpotentials (η_{10}) of 31, 49, and 64 mV at a current density of -10 mA cm^{-2} in 0.5 M H₂SO₄, 1.0 KOH, and 1.0 M PBS, respectively, exceeding the overwhelming majority of the documented transition metal phosphide-based electrocatalysts. Density functional theory calculation reveals that the superior electrocatalytic performance for hydrogen evolution reaction could be ascribed to the strong coupling effects of the reactive facets of CoP and Co₂P with the 3D porous NC nanosheet, making it exhibit a more thermo-neutral hydrogen adsorption free energy.

INTRODUCTION

Water splitting via electrolysis has been regarded as a promising technology to produce hydrogen to mitigate the dependence on fossil fuels (You and Sun, 2018; Turner, 2004). To date, many non-Pt catalysts for hydrogen evolution reaction (HER), such as transition-metal chalcogenides (Zhang et al., 2016a, Lu et al., 2016; Chen et al., 2016a; Staszak-Jirkovský et al., 2016), carbides (Li et al., 2016; Lu et al., 2019; Fan et al., 2015), nitrides (Zhang et al., 2016b; Cao et al., 2013), phosphides (Pu et al., 2017; Chung et al., 2017; Shi and Zhang, 2016), metal alloys (Zhang et al., 2017a), and heteroatom-doped nanocarbons (Zhang et al., 2016c; Qu et al., 2017) have been reported. However, the catalytic performance of these electrocatalysts is far from being able to compete with Pt activity (Boppella et al., 2019), which limits their application in HER. Transition metal phosphides (TMPs), especially cobalt phosphide (CoP or Co₂P), have attracted great attention because of their acid-base stability over a wide pH range of 0–14 (Wang et al., 2017a). Various cobalt phosphide materials with different morphologies and structures, such as nanoparticles (Vigil et al., 2016), nanorods (Zhu et al., 2015), nanowires (Xu et al., 2018), nanosheets (Liu et al., 2017a; Li et al., 2018a), nanotubes (Du et al., 2014), polyhedrons (Wu et al., 2017), metal-organic framework-derived porous nanostructures (Chai et al., 2020), and Co₂P nanorods (Doan-Nguyen et al., 2015; Zhang et al., 2020; Liu et al., 2018), have been developed. These materials have been engineered to maximize the number of active sites for optimal electrocatalytic performance toward the goal of HER. Meanwhile, bimetallic phosphides (NiCoP, Yu et al., 2016; Zhang et al., 2017b, CoFeP, Tan et al., 2016; Chen et al., 2019; MoWP, Wang et al., 2016, etc.), Co/CoP heterostructure (Wang et al., 2017b; Xue et al., 2017), B- or N-doped CoP (Cao et al., 2020; Zhou et al., 2018), and CoP with exposed high-energy crystal planes (Zhang et al., 2017c) demonstrated enhanced HER electrocatalytic performance owing to the appropriately optimized adsorption free energy of H on the surface (ΔG_{H^*}). However, the catalytic stability of bare TMPs is insufficient under high overpotential and strong alkaline conditions. To address this issue, TMPs encapsulated into nitrogen-doped carbon (NC) has been developed, which exhibits better activity and stability than the naked ones (Ma et al., 2017). Within this unique structure, the TMP core can be effectively protected by NC in the liquid electrolytes, and the synergistic effect between TMPs and NC can also create nonmetallic active sites and facilitate the electrocatalytic reaction (Ma et al., 2018).

¹School of Chemistry and Chemical Engineering, Inner Mongolia Key Lab of Nanoscience and Nanotechnology, Inner Mongolia Engineering and Technology Research Center for Catalytic Conversion and Utilization of Carbon Resource Molecules, Inner Mongolia University, Hohhot 010021, P.R. China

²Key Laboratory of Advanced Energy Materials Chemistry, Tianjin Key Lab for Rare Earth Materials and Applications, Center for Rare Earth and Inorganic Functional Materials, School of Materials Science and Engineering & National Institute for Advanced Materials, Nankai University, Tianjin 300350, P. R. China

³School of Chemistry and Chemical Engineering, Tianjin University of Technology, Tianjin, P. R. China

⁴School of Chemistry, Physics and Mechanical Engineering, Queensland University of Technology, Brisbane, QLD 4001, Australia

⁵Key Laboratory of Applied Surface and Colloid Chemistry, School of Chemistry and Chemical Engineering, Shaanxi Normal University, Xi'an 719119, P. R. China

⁶These authors contributed equally

⁷Lead Contact

*Correspondence: nmjp219@163.com (P.J.), gaorui@imu.edu.cn (R.G.), ypcdu@nankai.edu.cn (Y.D.), cejzhang@imu.edu.cn (J.Z.)

<https://doi.org/10.1016/j.isci.2020.101264>



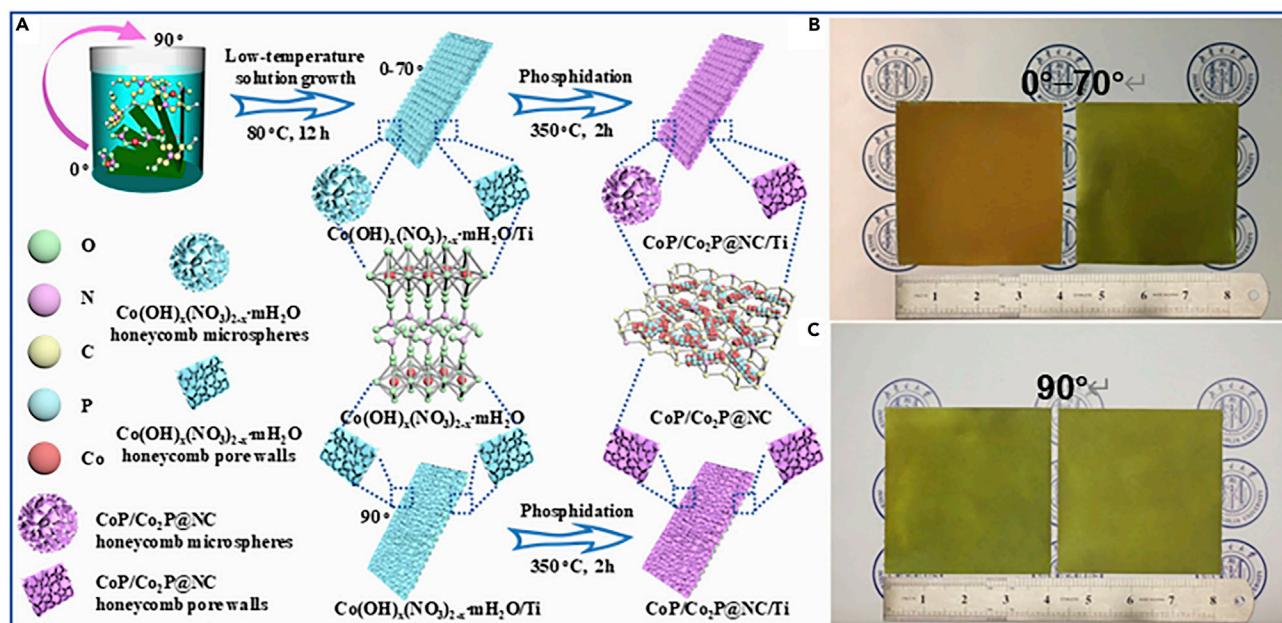


Figure 1. Synthesis of CoP/Co₂P@NC/Ti Self-Supported Electrode

(A) Schematic illustration shows the construction of a series of nitrogen-doped carbon (NC) nanosheet array constituting CoP and Co₂P single-crystal nanorods (CoP/Co₂P@NC) on Ti foil with different angles placed in solution during the growth process.

(B) Optical photographs show the Co(OH)_x(NO₃)_{2-x}·mH₂O honeycomb microspheres (left) and Co(OH)_x(NO₃)_{2-x}·mH₂O honeycomb pore walls (right) on two sides of an inch-sized Ti foil (0°–70°).

(C) Optical photographs show the Co(OH)_x(NO₃)_{2-x}·mH₂O honeycomb pore walls on two sides of an inch-sized Ti foil (90°).

To further improve the electrocatalytic performance, another issue is providing good contact between chemically synthesized catalysts and the electrode surface, which determines the interface resistance, and therefore the performance of the electrocatalyst. Directly growing electrocatalysts on a current collector is desirable to ensure good contact and thereby improve the performance of electrocatalyst (Tian et al., 2014). At present, various TMPs have been deposited on current-collecting substrates via a two-step approach: depositing metal precursors onto substrates and then converting them into the corresponding phosphides by a low-temperature phosphidation reaction to achieve self-supported electrocatalysts as effective HER cathodes (Jiang et al., 2014; Sun et al., 2020). However, during synthesis, urea as a precipitating agent and noxious NH₄F as an etchant are often used to increase the loading of metal phosphides, control their morphologies and structures, and enhance the adhesion force between the metal phosphides and current collectors (Tang et al., 2017). Meanwhile, the electrocatalyst is normally adhered to one side of the current collector, which may lead to low utilization of current collectors and restrict further improvement of catalytic performance (Tang et al., 2016). Hence, the challenge is to develop effective approaches that can simultaneously (1) grow the active phases on both sides of the current collectors and control the size and exposed facets of the final metal phosphides to increase the exposed sites with high activity, (2) optimize the morphology to assure that the active sites are accessible, (3) improve the adhesion affinity between active phases and current collectors to achieve low charge transfer resistance and prevent loss of catalyst, (4) eliminate the use of toxic reagents, and (5) tune the electronic structure of active phases to increase the intrinsic activity of active sites.

Herein, we report a novel approach to prepare Janus- or twins-type 3D porous NC nanosheet arrays assembled into a honeycomb layer with CoP/Co₂P single-crystal nanorods encapsulated on both sides of an inch-size Ti foil (CoP/Co₂P@NC/Ti) as an efficient self-supported electrode for HER. It is constructed through a facile low-temperature-solution approach by growing a large-scale Janus- or twins-type honeycomb lamellar cobalt nitrate-hydroxide (Co(OH)_x(NO₃)_{2-x}·mH₂O (0 < x < 2)) on an inch-sized Ti foil followed by phosphidation (as illustrated in Figure 1). Amazingly, the type and size of honeycomb Co(OH)_x(NO₃)_{2-x}·mH₂O precursor deposited on two sides of a Ti foil can be easily tuned by adjusting the placement of titanium plates in growing process, and this unusual precursor can effectively regulate the morphology, structure, and crystalline phase of phosphatized product during phosphidation. In CoP/

Co₂P@NC/Ti electrode, the large honeycomb pores as well as the mesopores within the walls can act as diffusion channels for electrolyte to increase the active sites. Meanwhile, the nanorods of CoP and Co₂P are confined within the honeycomb pore walls and the NC matrix can protect them from agglomeration and corrosion. More importantly, the interaction between different facets in CoP/Co₂P and the NC shell is a key factor for optimizing the value of ΔG_{H^*} . These features ensure the high catalytic activity of the obtained optimal electrocatalyst toward the HER process, surpassing those of most previously reported cobalt phosphide electrocatalysts, and excellent durability of the optimal electrocatalyst.

RESULTS

Preparation of Honeycomb Porous Precursors and Electrodes

The scanning electron microscopic (SEM) images (Figures 2A–2L) illustrate the interesting finding mentioned in Figure 1. By adjusting the placement of Ti foil, two types of architectures can be fabricated, namely, a Janus-type structure (0°–70°) where the morphology of a precursor deposited on one side of a Ti foil is different from that on the other side and a twin-type structure (90°) where the morphology of the precursor deposited on the two sides of Ti foil is identical. When the Ti foil was tilted and then immersed in the reactant solution, the morphology of the lamellar precursor that formed on the two sides of Ti foil was different. On one side, microspheres (~2.7–6.3 μm in average diameter) of the honeycomb structure cover the Ti foil surface (Figures 2A–2E). On the other side, a layer of the honeycomb structure formed on the Ti foil surface, whereas the pores of the honeycomb structure are perpendicular to the foil surface (Figures S1A–S1E). Similarly, when Ti foil is vertical in the solution, two sides are covered by a layer of the honeycomb structure (Figures 2F and S1F). It should be noted that a honeycomb structure with pore walls of ~12–25 nm thickness with a smooth surface is the basic unit for the morphology of the precursor formed on both sides (Figures 2G–2K and S1G–S1K). The precursors were prepared via a low-temperature-solution (80°C) process in the presence of triethanolamine (TEOA) (as illustrated in Scheme S1): a precursor of lamellar nitrate-hydroxide cobalt (Co(OH)_x(NO₃)_{2-x}·mH₂O) was proposed for the first time (Figure S2). During preparation, TEOA, as an organic ligand, was used to induce the formation of highly porous honeycomb structures. Interestingly, only honeycomb structured Co(OH)_x(NO₃)_{2-x}·mH₂O precursor microspheres were formed in the absence of the Ti foil (Figure S3). This indicates that the honeycomb structured layer can only form when deposition takes place on the foil, whereas the formation of the microspheres does not require direct contact with the foil. Therefore, the nucleation and growth of honeycomb structure on the Ti foil may be easier than the formation of honeycomb microspheres. Thus, in our approach, the honeycomb structured layer always forms on both sides of the foil; however, honeycomb microspheres are formed nearly exclusively on the top of the layer. To confirm this conclusion, the morphology evolution of Co(OH)_x(NO₃)_{2-x}·mH₂O with different time of low-temperature-solution reaction are studied (Figure S4). It can be found that the honeycomb structured layer forms on both sides of the foil during the initial stage of reaction and the honeycomb microspheres are gradually formed on the top of the layer with reaction time lasting. As it is well known, the way of nucleation and growth is closely related to the concentration of reactants. As seen in Scheme S1, at initial stage of reaction, the concentrations of reactants are same on both sides of Ti foil, thus the heterogeneous nucleation and growth of Co(OH)_x(NO₃)_{2-x}·mH₂O precursor will occur on the upper and lower surfaces of the Ti foil simultaneously with the formation of honeycomb structured layer. As reaction time was prolonged, the reactants near the Ti foil surface are continuously consumed and the reactants in bulk solution will diffuse toward the Ti foil surface. However, the diffusion rate to upper surface should be obviously faster than that to lower surface due to gravity, and the concentration of reactants near the upper surface is higher, which leads to the faster growth rate of Co(OH)_x(NO₃)_{2-x}·mH₂O precursor on the upper surface. When the upper surface is fully covered by honeycomb structured layer, the homogeneous growth of Co(OH)_x(NO₃)_{2-x}·mH₂O precursor occurs and the honeycomb microspheres appear on the upper surface. However, the concentration of reactants near the lower surface still could not reach the concentration at which homogeneous nucleation could occur. Therefore, a Janus-type structure will form when Ti foil is placed at 0–70°. Knowledge regarding the formation of different honeycomb structures may be useful for controlling the morphology and thickness of the precursor deposition on a Ti foil to achieve optimal HER activity after phosphidation. The corresponding elemental distribution mapping experiments reveal the homogeneous distribution of Co, C, N, and O elements in the lamellar nitrate-hydroxide cobalt precursor (Figures S5 and S6). Samples of the Co(OH)_x(NO₃)_{2-x}·mH₂O honeycomb structure and honeycomb microspheres were scratched off from the Ti foil and imaged with transmission electron microscope (TEM, Figure S7). The corresponding fast Fourier transform (FFT) images show closely arranged diffraction rings indicating the polycrystalline characteristics of the nitrate-hydroxide cobalt pore walls of the honeycomb layer and microsphere.

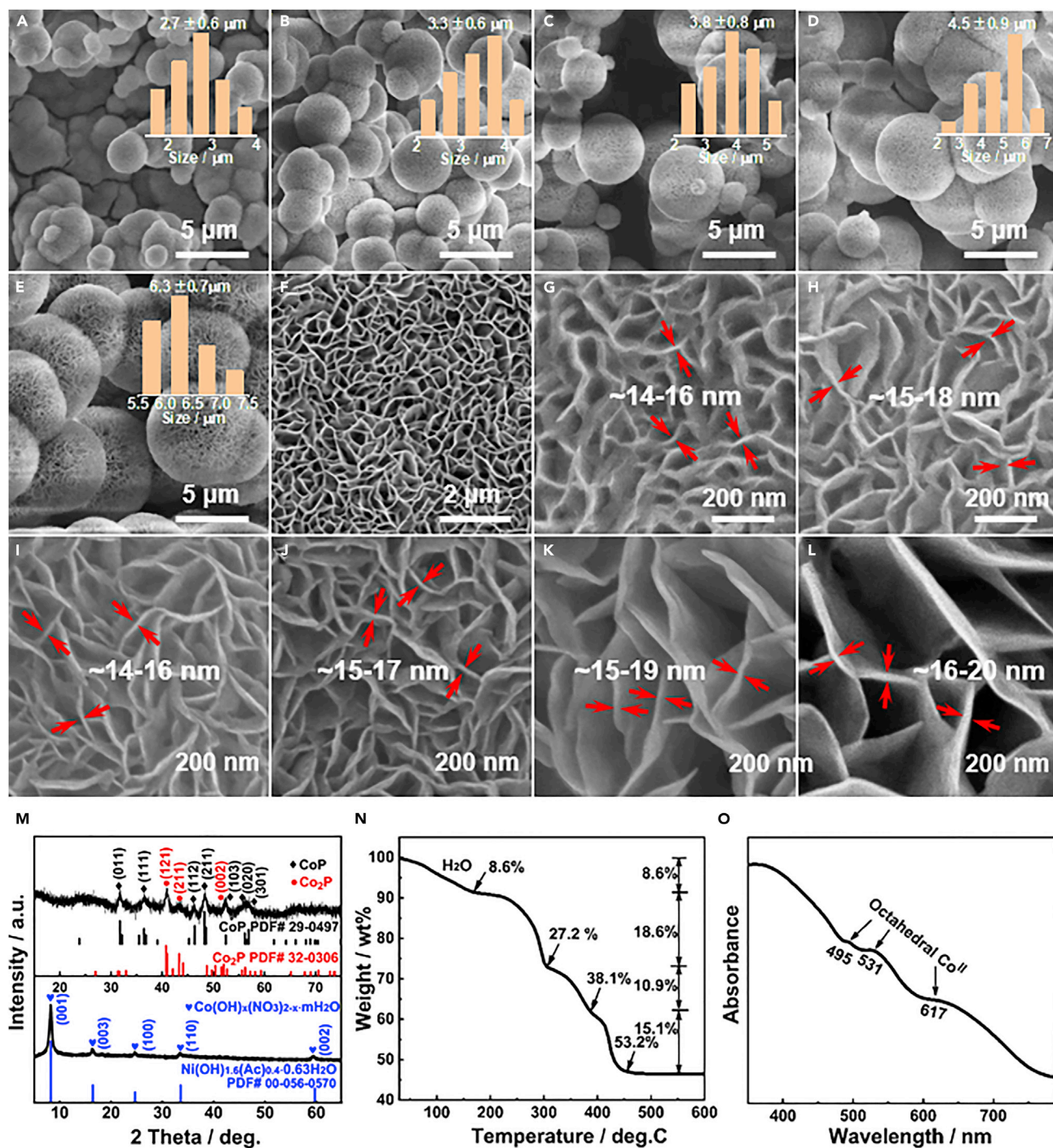


Figure 2. Characterization of Lamellar Nitrate-Hydroxide Cobalt Precursor

(A–F) SEM images of lamellar nitrate-hydroxide cobalt precursor of honeycomb structured microspheres for 0°, 10°, 30°, 50°, and 70° and honeycomb structured layer for 90°; inserts of (A–E) show the corresponding particle size distribution chart of precursor microspheres.

(G–L) Precursors with thin pore walls ($\sim 14\text{--}20 \text{ nm}$ thickness) for 0°–90°.

(M) XRD patterns of the lamellar nitrate-hydroxide cobalt precursor and cobalt phosphides scratched from Ti foils (black diamonds represent the diffraction peaks from CoP; red circles correspond to the diffraction peaks from Co₂P; blue hearts signify the lamellar nitrate-hydroxide cobalt precursor).

(N) TGA curve of lamellar nitrate-hydroxide cobalt precursor.

(O) UV-visible spectrum of lamellar nitrate-hydroxide cobalt precursor.

The X-ray diffraction (XRD) pattern of the precursor matches well with those of lamellar $\text{Ni}(\text{O}-\text{H})_{1.6}(\text{Ac})_{0.4} \cdot 0.63\text{H}_2\text{O}$ (ICDD PDF No. 00-056-0570) (Figure 2M). Thermogravimetric analysis (TGA) of the precursor (Figure 2N) shows that weight losses occurred at four stages (30–160°C, 225–300°C, 340–390°C, and 414–451°C), corresponding to the loss of free water, the dehydroxylation of the brucite-like layers, the decomposition of interlayer nitrate anions, and the decomposition of TEOA, respectively (Guo et al., 2014). UV-visible spectrum of the precursor displays three light absorption bands at 495, 531, and 617 nm (Figure 2O). These bands indicate the presence of hydroxylated cobalt (II). X-ray photoelectron spectroscopy (XPS) shows the superficial elemental composition and the states of the precursor (Figure S8). On the basis of the TGA, UV-visible spectra, and XPS results (Figures 2N, 2O, and S8), we determine that the lamellar nitride-hydroxide cobalt precursor exists in the form of $\text{Co}(\text{OH})_x(\text{NO}_3)_{2-x} \cdot m\text{H}_2\text{O}$ with ligand molecules of TEOA. The precursor of honeycomb layer is a dense deep green film, and the precursor of honeycomb microspheres formed a dense yellow film covering two sides of a Ti foil (Figure S9). On the contrary, when using urea as precipitant and NH_4F as etching agent instead of TEOA for the synthesis under the same reaction conditions, we obtained purple $\text{Co}(\text{OH})\text{F}$ film covering only one side of the foil with the other side blank (Figure S10). The film turned black after phosphidation.

After low-temperature phosphidation, the $\text{CoP}/\text{Co}_2\text{P}@ \text{NC}/\text{Ti}-\text{X}-\text{Y}$ (X denotes the placement angle of Ti foil in the synthesis process of $\text{Co}(\text{OH})_x(\text{NO}_3)_{2-x} \cdot m\text{H}_2\text{O}/\text{Ti}$ precursor, wherein, $X = 0, 10^\circ, 30^\circ, 50^\circ, 70^\circ, \text{ and } 90^\circ$; Y denotes phosphidation temperature, wherein $Y = 300^\circ\text{C}, 350^\circ\text{C}, 400^\circ\text{C}, \text{ and } 500^\circ\text{C}$) can be obtained. Clearly, both morphology and integrated nature of $\text{CoP}/\text{Co}_2\text{P}@ \text{NC}/\text{Ti}-\text{X}-\text{Y}$ with rough and plicated surface remained (Figures 3A–3F and S11A–S11F). The average diameter of microspheres diminished from $\sim 2.7\text{--}6.3$ to $\sim 2.3\text{--}5.6$ μm , and the thickness of the pore walls of the honeycomb structure increased slightly to about 23–35 nm (Figures 3G–3L and S11G–S11L). In honeycomb pore walls, a mixture of highly dispersed CoP and Co_2P crystals with a rod-like shape (7–10 nm thick and ca. 40–80 nm long) can be observed in an NC matrix ($\text{CoP}/\text{Co}_2\text{P}@ \text{NC}$) (Figures 4A–4H and S12). The XRD pattern of $\text{CoP}/\text{Co}_2\text{P}@ \text{NC}-10-350$ displays the diffraction peaks of orthorhombic CoP (ICDD PDF No. 29-0497) and Co_2P (ICDD PDF No. 32-0306), further suggesting the formation of cobalt phosphides after low-temperature ($<500^\circ\text{C}$) phosphidation (Figure 2M). In addition, a broad peak at $\sim 26.0^\circ$ corresponding to the (002) lattice planes of carbon implies that the NC matrix derived from the pyrolysis of the organic TEOA ligand is formed. This is confirmed by Raman spectra where two narrow peaks at 1,361 and 1,561 cm^{-1} were observed, which belong to the D-band and G-band of carbon, respectively (Figure S13). The corresponding elemental distribution mapping images clearly indicate the homogeneous distribution of Co, P, C, N, and O elements in $\text{CoP}/\text{Co}_2\text{P}@ \text{NC}$, confirming the uniform dispersion of CoP and Co_2P nanorods in the honeycomb layer and honeycomb microspheres (Figures 3M and S14). The O species may result from surface oxidation of $\text{CoP}/\text{Co}_2\text{P}@ \text{NC}-10-350$ when the sample was exposed to air.

High-resolution transmission electron microscopic (HRTEM) images of CoP and Co_2P nanocrystals taken from the different regions of the scratched $\text{CoP}/\text{Co}_2\text{P}@ \text{NC}$ specimen (Figures 4C–4H) display well-resolved lattice fringes with interplanar distances of 0.197, 0.221, and 0.254 nm that are indexed to the (112) and (200) lattice planes of CoP and the (121) lattice plane of Co_2P , respectively. Successive lattice fringes with the same orientation pervade each crystal, manifesting the single-crystal nature of the nanorods. The results suggest that the nitrate-hydroxide cobalt precursor is converted into mixed CoP and Co_2P phases. The low-magnification high-angle annular dark field scanning transmission electron microscopic (HAADF-STEM) image (Figure 4I) shows numerous bright rods in nanosheet representing the CoP and Co_2P , further revealing that rod-like CoP and Co_2P crystals are embedded in honeycomb pore walls. The highly-magnified HAADF-STEM images and corresponding energy-dispersive X-ray (EDX) elemental mapping images show that C, N, Co, P, and O elements are evenly distributed within the $\text{CoP}/\text{Co}_2\text{P}@ \text{NC}$ pore walls (Figures 4I–4P). It is also confirmed by the EDX spectrum (Figure 4Q). Hence, the carbon- and nitrogen-containing lamellar cobalt precursor is crucial for achieving electrode materials with ultrafine CoP and Co_2P nanorods that are well dispersed in an NC matrix. The NC effectively prevents aggregation and oxidation of CoP and Co_2P nanocrystals, maintaining them in small and dispersed crystals, so that the electrochemically active components of CoP and Co_2P nanocrystals are stabilized where a large external surface area of the crystals are exposed. In addition, the strong coupling effect of $\text{CoP}/\text{Co}_2\text{P}$ nanocrystals with the NC matrix may promote the electrocatalytic performances (Zhuang et al., 2016). The influence of the phosphidation temperature on the structure evolution of $\text{CoP}/\text{Co}_2\text{P}@ \text{NC}$ is also studied. SEM analysis shows that $\text{CoP}/\text{Co}_2\text{P}@ \text{NC}-10-300$ and $\text{CoP}/\text{Co}_2\text{P}@ \text{NC}-10-400$, obtained by the phosphidation at temperatures of 300°C and 400°C, respectively, maintain their original honeycomb structure, although a slight variation in surface roughness and pore wall thickness is observed (Figures S15A–S15H). When the phosphidation temperature was raised

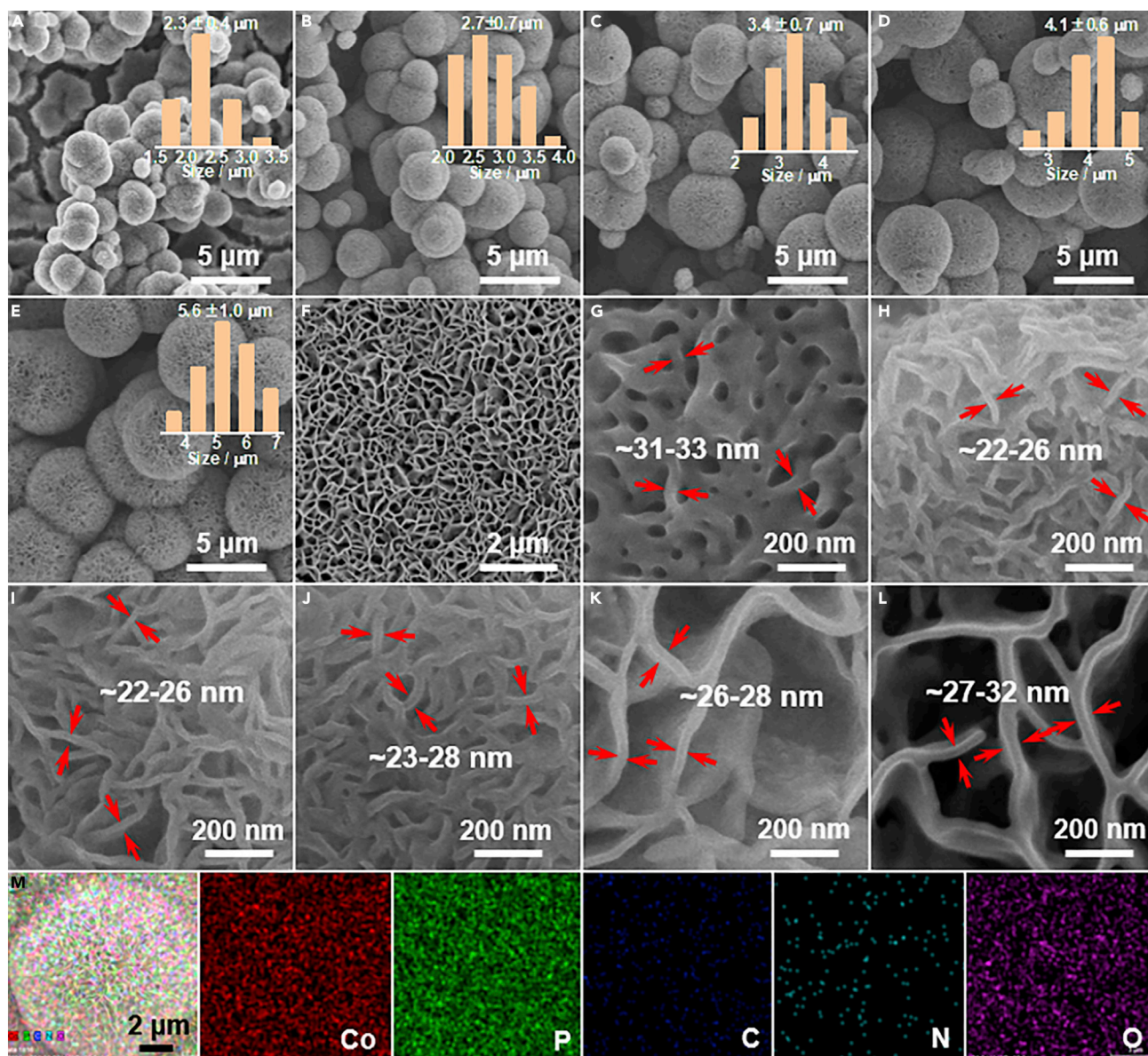


Figure 3. Characterization of CoP/Co₂P@NC Honeycomb Structured Microspheres/Layers

(A–L) (A–F) SEM images of CoP/Co₂P@NC of honeycomb structured microspheres for 0°, 10°, 30°, 50°, and 70° and honeycomb structured layer for 90°; inserts of (A–E) show the corresponding particle size distribution chart of CoP/Co₂P@NC microspheres. (G–L) CoP/Co₂P@NC honeycomb microspheres with thick pore walls (~22–33 nm thickness) for 0°–90°.

(M) The EDX elemental mapping images of CoP/Co₂P@NC microsphere on Ti foil showing the distributions of elements Co, P, C, N, and O.

to 500°C, collapses of the honeycomb pore walls are observed (Figures S15I–S15L). In the XRD patterns of CoP/Co₂P@NC-10-300 and CoP/Co₂P@NC-10-400 samples, CoP crystals are observed (Figure S16), but the CoP crystals existed only after the phosphidation at 500°C, and the Co₂P phase vanished.

The XPS survey scan of CoP/Co₂P@NC/Ti-10-350 electrode (Figure S17A) suggests the existence of Co, P, N, C, and O elements. The Co 2p_{3/2} spectrum exhibits two main peaks at 778.8 and 781.6 eV, respectively, and a satellite at 784.9 eV, attributed to the Co–P in CoP, oxidized Co species, and the satellite peak, respectively. The peak assignments in Co 2p_{1/2} spectrum are similar to those of Co 2p_{3/2} (Figure S17B). The oxidized Co species arise from the unavoidable contact of the surface of CoP or Co₂P with air. The high-resolution spectrum for P 2p displays two peaks at 129.4 and 130.3 eV assigned to P 2p_{3/2} and P

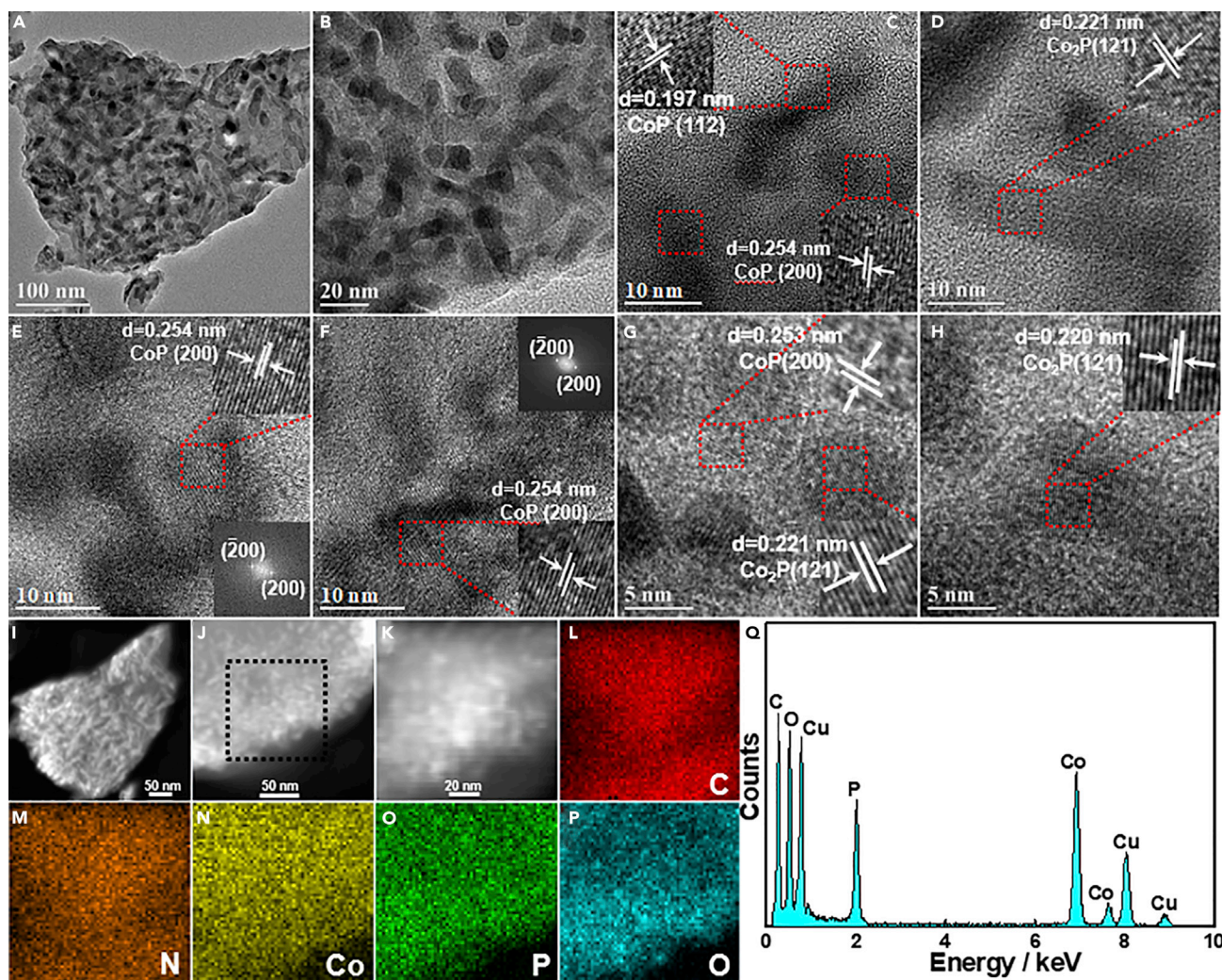


Figure 4. Characterization of CoP/Co₂P@NC-10-350

(A and B) TEM images of the pore wall in CoP/Co₂P@NC-10-350 specimen scratched from Ti foil.

(C–H) HRTEM images of CoP and Co₂P nanorods dispersed in NC porous matrix at different regions of the pore walls in CoP/Co₂P@NC-10-350 specimen; insets in (E) and (F) show the corresponding fast Fourier transform (FFT) images.

(I–K) STEM images of pore wall in CoP/Co₂P@NC-10-350 specimen.

(L–P) The corresponding EDX elemental mapping images of C, N, Co, P, and O in CoP/Co₂P@NC-10-350 specimen.

(Q) EDX spectrum of CoP/Co₂P@NC-10-350 specimen.

$2p_{1/2}$, respectively (Pan et al., 2018). The peak at 134.0 eV is due to oxidized phosphorous species, such as PO_4^{3-} or P_2O_5 (Figure S17C). Comparing the peaks with those of metallic Co $2p_{3/2}$ (778.1–778.2 eV) and elemental P (130.2 eV), consistent with previous report (Liu et al., 2014), we note that the Co $2p_{3/2}$ binding energy exhibits a positive shift, whereas the P 2p displays a negative shift. It suggests that the Co and P in the CoP/Co₂P@NC/Ti-10-350 electrode have a partial positive charge (δ^+) and negative charge (δ^-), respectively, implying the electron transformation from Co to P. The electron-deficient Co and electron-rich P can function as the hydride-acceptor and proton-acceptor centers, respectively, which facilitates the HER (Popczun et al., 2013). The XPS spectrum of O 1s shows three feature peaks at 529.4, 530.9, and 532.7 eV, which are assigned to lattice oxygen, adsorbed oxygen on CoO_x and the adsorption of hydroxyl oxygen on the surface, respectively (Figure S18D). The fitted C 1s spectrum presents a major peak at 284.7 eV and two satellite peaks at 285.54 and 286.6 eV, assigned to the C-C, C-N, and C-C in the NC nanowall matrix, respectively (Figure S18E) (Deng et al., 2014). The high-resolution N 1s XPS spectrum shows peaks at 399.8 eV corresponding to pyrrolic N species and 401.3 eV indexed to quaternary N species (Figure S18F) (Jiao et al., 2016), which further verifies the formation of an NC pore wall matrix with encapsulated

CoP/Co₂P nanorods. The pyrrolic N species can improve the electrocatalytic HER activity by interacting with H⁺ (Pan et al., 2018), whereas the quaternary N species facilitates the activation of the adjacent carbon and generates more non-metallic active sites (Yang et al., 2017).

A Useful Structural Feature of the Catalysts

Previously reported CoP synthesized via low-temperature phosphidation usually yielded round particles (Li et al., 2018b), which are obviously different from the CoP and Co₂P nanorods produced in this study. It is worth noting that the crystal growth orientation of rods is different from those of round particles. The diffraction spots in the FFT images (inset images in Figures 4E and 4F) can be indexed to the (200) planes of CoP, rather than the (011), (211), (112), or (111) facets previously reported for CoP nanoparticles synthesized using other precursors under similar phosphidation conditions. This result indicates that the crystal growth orientation of cobalt phosphide nanorods could be regulated by the morphology and chemical composition of the precursor. The electrocatalytic performance of CoP and Co₂P nanocrystals depends substantially on the crystal orientation and is discussed below.

To verify the conclusion further, the CoP/Co₂P@NC/Ti-10-350 (Cl) electrode was also prepared by phosphidation of another precursor Co(OH)_x(Cl)_{2-x}·mH₂O, obtained by using CoCl₂·6H₂O as cobalt source in the precursor preparation (Figures S18 and S19). The corresponding TEM images reveal that the sample mainly contains irregular-shaped CoP and Co₂P nanocrystals in the CoP/Co₂P@NC walls and only the (211) and (111) lattice planes of CoP can be observed (Figures S19K–S19L). We also synthesized CoP nanowires using urea as a precipitant and NH₄F as an etching agent for comparison (Figure S20). The TEM and HRTEM images (Figures S20B–S20D) show that the CoP nanowires with diameters of ~30–40 nm and lengths of ~100–200 nm are composed of ~5- to 6-nm CoP crystals rather than single-crystal CoP nanorods. Evidently, the Co(OH)_x(NO₃)_{2-x}·mH₂O precursor is preferred for the formation of single-crystal CoP and Co₂P nanorods with (200) planes of CoP and (121) planes of Co₂P as the predominant facets.

HER Electrocatalytic Performance

The HER electrocatalytic activities of CoP/Co₂P@NC/Ti-X-Y electrodes were evaluated in N₂-saturated acidic (0.5 M H₂SO₄), neutral (1.0 M PBS), and alkaline (1.0 M KOH) aqueous solutions (experimental details are provided in Supplemental Information). For comparison, bare Ti foil, commercial Pt/C (20 wt %), and CoP-NWs/Ti were also tested. Linear sweep voltammograms of these samples recorded in 0.5 M H₂SO₄ are shown in Figure 5A. The CoP/Co₂P@NC/Ti-10-350 electrode displays excellent catalytic activity with overpotentials as low as 31 mV required to achieve current densities of 10 mA cm⁻². This overpotential is slightly higher than that of a Pt/C electrode (26 mV) but much lower than those of bare Ti foil, CoP/Co₂P@NC/Ti-0-350 (72 mV), CoP/Co₂P@NC/Ti-30-350 (33 mV), CoP/Co₂P@NC/Ti-50-350 (37 mV), CoP/Co₂P@NC/Ti-70-350 (47 mV), CoP/Co₂P@NC/Ti-90-350 (97 mV), and the CoP NWs/Ti electrode without the NC nanowall matrix (106 mV) (Table S1). When correlating the catalytic activity to structural features, some key insights can be obtained. Polycrystalline CoP nanowires require much higher overpotential than CoP/Co₂P@NC/Ti-10-350, although there is no resistance/limitation for diffusion to the nanowires. The structure of samples CoP/Co₂P@NC/Ti-X-Y is similar, where the CoP/Co₂P nanorods are embedded in NC matrix. These samples exhibited much lower overpotentials than CoP NWs/Ti. Therefore, the wrapped NC matrix, where there are abundant active sites, appears to be a key factor for superior HER performance. The HER activity of CoP/Co₂P@NC/Ti-10-350 electrode surpasses that of overwhelming majority of very recently reported TMP-based HER electrocatalysts in acidic aqueous medium (Table S2). In addition, the crystallinity of the cobalt phosphides in the electrode also affects the performance. CoP/Co₂P@NC/Ti-10-350 has better crystallinity than CoP/Co₂P@NC/Ti-10-300 (Figure S16) and shows a lower overpotential, whereas the pore structure of the two samples is similar (Figure S21).

Figure 5B displays the Tafel plots for cobalt phosphide electrodes and Pt/C. The Tafel slope for the CoP/Co₂P@NC/Ti-10-350 electrode was 44 mV dec⁻¹ and lower than that for CoP/Co₂P@NC/Ti-0-350 (53 mV dec⁻¹), CoP/Co₂P@NC/Ti-30-350 (46 mV dec⁻¹), CoP/Co₂P@NC/Ti-50-350 (45 mV dec⁻¹), CoP/Co₂P@NC/Ti-70-350 (50 mV dec⁻¹), CoP/Co₂P@NC/Ti-90-350 (50 mV dec⁻¹), CoP-NWs/Ti (55 mV dec⁻¹), and other TMP-based HER electrocatalysts reported recently (Figure 5B, Tables S1 and S2). A smaller Tafel slope is more beneficial for practical application as it would lead to a remarkably increased HER rate with a decrease in overpotential (Liu et al., 2017b). We also assessed the intrinsic catalytic activities of CoP/Co₂P@NC/Ti-X-Y, CoP-NWs/Ti, and Pt/C electrodes for the HER in 0.5 M H₂SO₄ medium by measuring the turnover frequency (TOF) at an overpotential of 100 mV (Figure S22). As shown in

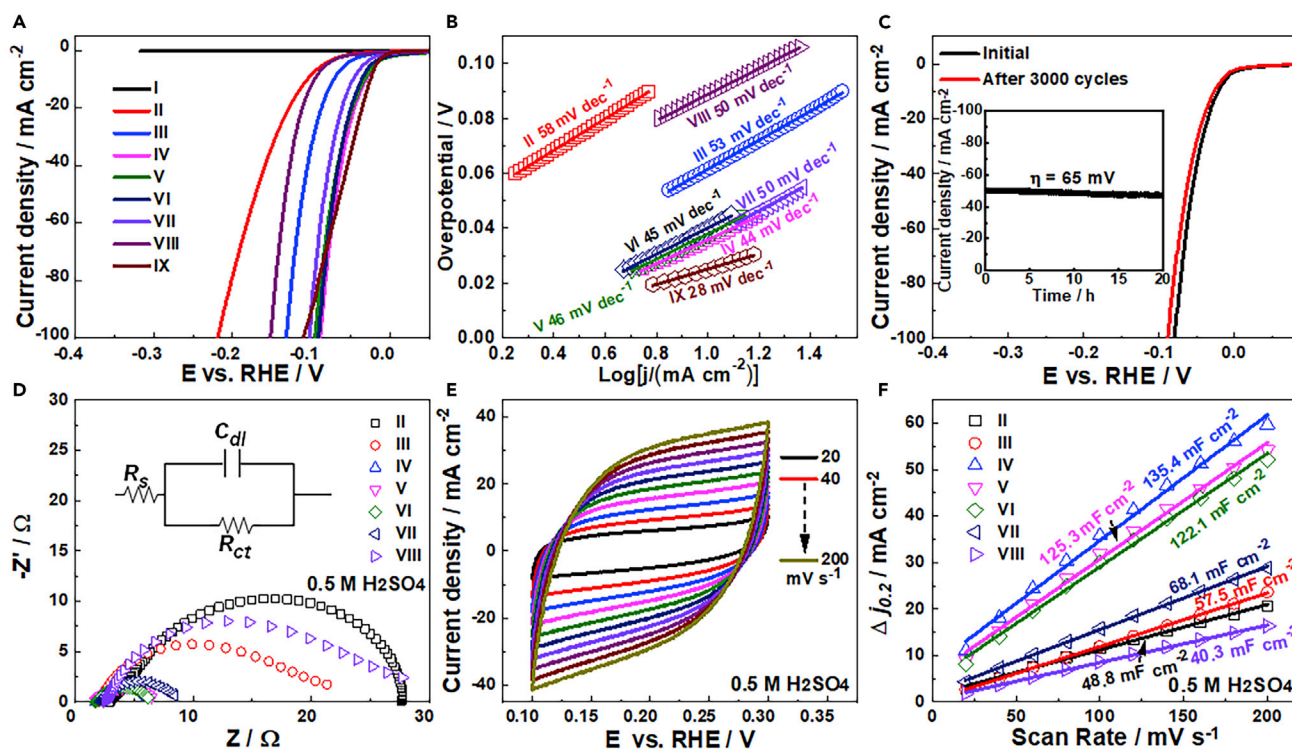


Figure 5. HER Performance of CoP/Co₂P@NC/Ti-10-350 in 0.5 M H₂SO₄

(A and B) (A) Linear sweep voltammogram (LSV) curves and (B) Tafel plots of different samples in 0.5 M H₂SO₄. (C) LSV curves of CoP/Co₂P@NC/Ti-10-350 electrode before and after 3000 CV cycles from +0.10 to −0.25 V versus RHE in 0.5 M H₂SO₄ (inset shows the chronoamperometry i-t curves of CoP/Co₂P@NC/Ti-10-350 at the overpotential of 65mV in 0.5 M H₂SO₄). (D) Nyquist plots of the electrochemical impedance spectra of different samples at $\eta = -65$ mV in 0.5 M H₂SO₄. (E) CVs performed at various scan rates in the region 0.1–0.3 V versus RHE for CoP/Co₂P@NC/Ti-10-350 in 0.5 M H₂SO₄. (F) The capacitive current densities at +0.20 V as a function of scan rate for different samples ($\Delta j = j_a - j_c$). (I) bare Ti foil, (II) CoP-NWs/Ti, (III) CoP/Co₂P@NC/Ti-0-350, (IV) CoP/Co₂P@NC/Ti-10-350, (V) CoP/Co₂P@NC/Ti-30-350, (VI) CoP/Co₂P@NC/Ti-50-350, (VII) CoP/Co₂P@NC/Ti-70-350, (VIII) CoP/Co₂P@NC/Ti-90-350, and (IX) Pt/C.

Figure S22B, CoP/Co₂P@NC/Ti-10-350 electrode achieves a TOF of 0.61 s^{−1} at an overpotential of 100 mV, much smaller than that for Pt/C (1.80 s^{−1}) and greater than that for CoP-NWs/Ti electrode (0.14 s^{−1}), suggesting the intrinsic superior HER activity of CoP/Co₂P@NC/Ti-10-350. In fact, this value is also higher than those of reported CoP-based electrocatalysts at the same overpotential, such as CoP/Ti (0.24 s^{−1}) (Zhang et al., 2018), CoP/CC (0.11 s^{−1}) (Zhang et al., 2017c), and CoP NWs/Ti (0.14 s^{−1}) (Gao et al., 2017). An important criterion for a heterogeneous catalyst is its long-term stability. The stability of the CoP/Co₂P@NC/Ti-10-350 electrode was tested first via an accelerated degradation test (ADT) using cyclic voltammetry (CV) at 100 mV·s^{−1} in a potential range of +0.1 to −0.25 V versus reversible hydrogen electrode (RHE). The polarization curve shows a negligible drift after 3,000 continuous cycles, and the overpotentials required to achieve current densities of 10 and 100 mA cm^{−2} merely increase by 7 and 9 mV, respectively (Figure 5C). The time-dependent catalytic current density curve was also measured (inset image in Figure 5C) and shows that the electrocatalytic activity was almost unchanged after 20 h. After long-term testing, we observed small cracks in the honeycomb layer, whereas the CoP/Co₂P@NC/Ti-10-350 electrode retained its integral configuration (Figures S23A–S23F). However, the structure and chemical composition remained unchanged (Figures S23G–S23I and S24–S26). These results demonstrate that the honeycomb structured CoP/Co₂P@NC/Ti-10-350 electrode is stable during long-term operation in acidic medium.

To further understand how the structural features of the electrocatalysts influence their performance, we conducted measurements at various potentials in 0.5 M H₂SO₄ solution. The Nyquist plots of different electrodes at $\eta = 65$ mV in 0.5 M H₂SO₄ solution are presented in Figure 5D. The corresponding R_s and R_{ct} in 0.5 M H₂SO₄ solution for these electrodes were calculated and listed in Table S3. The resistances for CoP/Co₂P@NC/Ti-10-350 electrode are R_s of 1.75 Ω and R_{ct} of 4.35 Ω at the catalyst/electrolyte interface, smaller

than the values recorded for CoP-NWs/Ti and other CoP/Co₂P@NC/Ti-X-Y electrodes, reflecting better contact between the current collectors and the CoP/Co₂P@NC/Ti-10-350 catalyst, resulting in rapid charge transfer kinetics (Chen et al., 2016b). The superior charge transfer ability can promote the transfer of electrons to H_{ads} and is beneficial for minimizing concomitant ohmic losses, thus contributing significantly to enhance the electrocatalytic activity. The effective electrochemical active surface areas (ECSAs) can be estimated from the double-layer capacitances (C_{dl}) at solid-liquid interface. C_{dl} was measured by CV at various scan rates in a non-faradic region from 0.1–0.3 V versus RHE (Figures 5E and S27). The C_{dl} is linearly proportional to the ECSAs (ECSAs = C_{dl}/C_s, where C_s is the capacitance of an atomically smooth planar surface of the material per unit area under identical electrolyte conditions and the average value is 40 μF cm⁻²), which can be calculated by the slope of the linear relationship between the current density against the scan rate (Figure 5F) (Yang et al., 2016). The CoP/Co₂P@NC/Ti-10-350 electrode presents the highest C_{dl} of 135.4 mF·cm⁻² when compared with CoP/Co₂P@NC/Ti-0-350 (48.8 mF cm⁻²), CoP/Co₂P@NC/Ti-30-350 (125.3 mF cm⁻²), CoP/Co₂P@NC/Ti-50-350 (122.1 mF cm⁻²), CoP/Co₂P@NC/Ti-70-350 (68.1 mF cm⁻²), and CoP/Co₂P@NC/Ti-90-350 (40.3 mF cm⁻²). Meanwhile, this value is over than sextuple that of CoP-NWs/Ti (48.8 mF cm⁻²). These results indicate that the CoP/Co₂P@NC/Ti-10-350 electrode has the largest number of electrocatalytic active sites among these samples. Given that the C_{dl} varies with the ECSA, the C_{dl}-normalized current density may reflect the intrinsic HER activity (Figure S28). It was found that the C_{dl}-normalized HER activity for CoP/Co₂P@NC/Ti-10-350 electrode is higher than that of CoP-NWs/Ti, indicating that combining CoP and NC can realize the improvement of intrinsic HER activity of active sites. The synergistic effects between CoP and N dopants can activate carbon atoms adjacent to the N dopants and generate more non-metallic active sites on NC, thus boosting the HER activity of CoP/Co₂P@NC/Ti-10-350.

Another challenging requirement for a good noble-metal-free HER catalyst is high catalytic activity and operation stability over a wide pH range. Therefore, we investigated the HER activity of the CoP/Co₂P@NC/Ti-10-350 electrode in alkaline and neutral media. It delivers excellent HER activity in 1.0 M KOH and 1.0 M phosphate buffer saline (PBS) solution (Figures 6A and 6D, and Table S1). The onset overpotentials of CoP/Co₂P@NC/Ti-10-350 electrode is only 18 and 30 mV in 1.0 M KOH and 1.0 M PBS solution, respectively. To achieve the cathode current densities of 10, 20, and 100 mA·cm⁻² in alkaline solution, the CoP/Co₂P@NC/Ti-10-350 electrode only requires overpotentials of approximately 49, 68, and 116 mV, respectively (Figure 6A), outperforming those of CoP-NWs/Ti (91, 117, and 239 mV). In fact, the HER activity of CoP/Co₂P@NC/Ti-10-350 favorably compares with that of most the reported TMP-based HER electrocatalysts tested in alkaline solution (Table S4). In addition, the CoP/Co₂P@NC/Ti-10-350 electrode also exhibits excellent electrocatalytic performance in neutral medium where only small overpotentials of 64 and 96 mV are required to afford current densities of 10 and 20 mA·cm⁻² for CoP/Co₂P@NC/Ti-10-350 electrode (Figure 6D). The overpotentials are lower than those of CoP-NWs/Ti (225 and 308 mV) and most of the previously reported TMP-based electrocatalysts (Table S5). The mass-normalized HER activities of CoP/Co₂P@NC/Ti-X-Y electrodes show that the mass activity of CoP/Co₂P@NC/Ti-10-350 electrode in acidic, alkaline, and neutral solutions are also better than those of other electrodes (Figure S29). This result suggests that the CoP/Co₂P@NC/Ti-10-350 electrode possesses high intrinsic activity. The Tafel slopes measured with CoP/Co₂P@NC/Ti-10-350 electrode in alkaline and neutral solutions are 51 and 98 mV dec⁻¹, respectively (Figures 6B and 6E). Similar to acidic conditions, the CoP/Co₂P@NC/Ti-10-350 electrode also exhibits faster HER kinetics and activity through smaller Tafel slope, compared with the CoP-NWs/Ti electrode and other reported HER electrocatalysts (Table S4 and Table S5). In addition, The HER activity of CoP/Co₂P@NC/Ti-10-350 (Cl) electrode was also evaluated for comparison. As shown in Figure S30, the CoP/Co₂P@NC/Ti-10-350 (Cl) electrode exhibits overpotentials of 53, 73, and 92 mV at a current density of -10 mA cm⁻² in 0.5 M H₂SO₄, 1.0 M KOH, and 1.0 M PBS solutions, respectively, slightly larger than CoP/Co₂P@NC/Ti-10-350 electrode. The differences in HER activities may result from different morphology, size, and predominant facets of Co₂P and CoP nanorods in the CoP/Co₂P@NC walls.

The long-term durability of CoP/Co₂P@NC/Ti electrode was also tested in alkaline and neutral media. After an ADT test the polarization curves of CoP/Co₂P@NC/Ti-10-350 electrode only exhibited a slight decay, where the overpotential increased by 16 mV for achieving -100 mA·cm⁻² in alkaline solution (Figure 6C). An insignificant increase of the overpotential at a current density of 50 mA·cm⁻² was observed after an ADT test in neutral medium (Figure 6F). The long-term durability test shows that the current density decreases by only 9% and 8% after 20 h of electrolysis in alkaline and neutral media, respectively (inset images in Figures 6C and 6F). These results demonstrate the excellent catalytic stability of CoP/Co₂P@NC/Ti-10-350

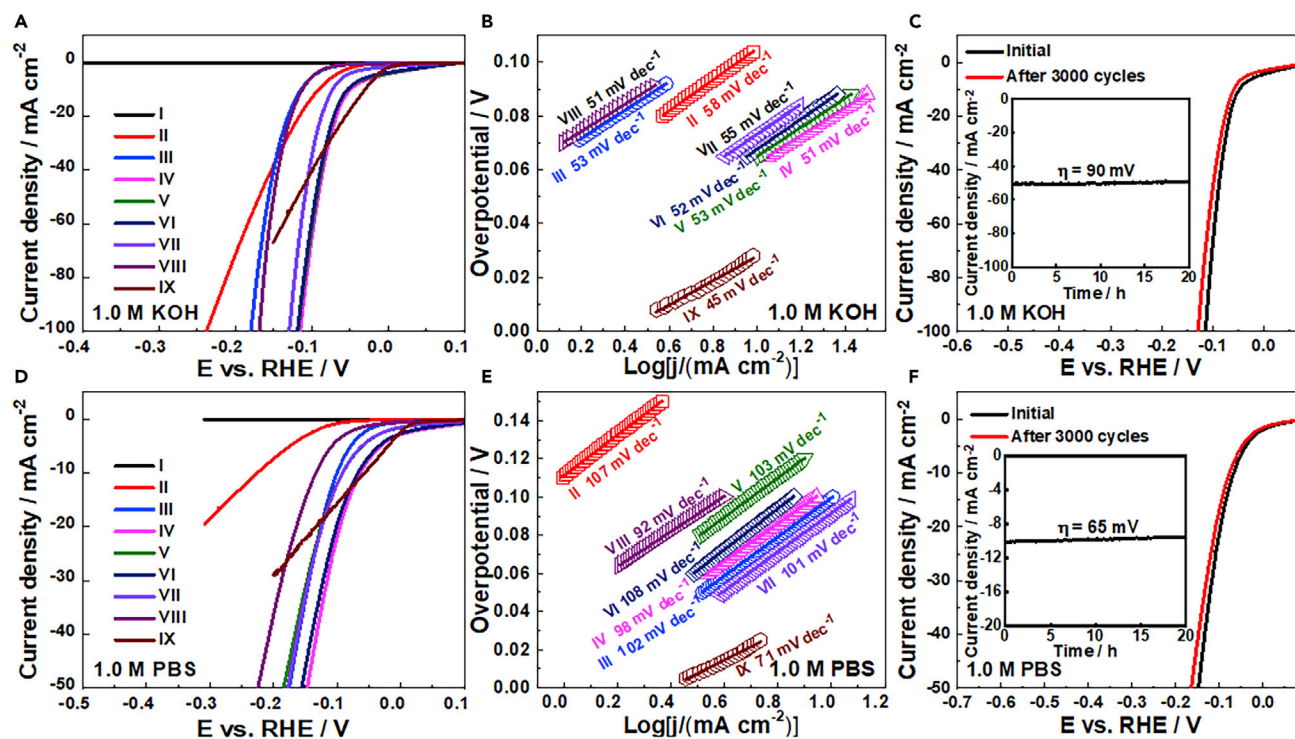


Figure 6. HER Performance of CoP/Co₂P@NC/Ti-10-350 in 1.0 M KOH and 1.0 M PBS Solutions

Linear sweep voltammogram (LSV) curves of (I) bare Ti foil, (II) CoP-NWs/Ti, (III) CoP/Co₂P@NC/Ti-0-350, (IV) CoP/Co₂P@NC/Ti-10-350, (V) CoP/Co₂P@NC/Ti-30-350, (VI) CoP/Co₂P@NC/Ti-50-350, (VII) CoP/Co₂P@NC/Ti-70-350, (VIII) CoP/Co₂P@NC/Ti-90-350, and (IX) Pt/C in (A) 1.0 M KOH and (D) 1.0 M PBS solutions; The corresponding Tafel slopes in (B) 1.0 M KOH and (E) 1.0 M PBS solutions; LSV curves of CoP/Co₂P@NC/Ti-10-350 electrode before and after 3,000 CV cycles from +0.10 to -0.25 V versus RHE in (C) 1.0 M KOH and (F) 1.0 M PBS solutions. Inset images in (C) and (F) show the chronoamperometry *i*-*t* curves of CoP/Co₂P@NC/Ti-10-350 at overpotentials of 90 and 65 mV in 1.0 M KOH and 1.0 M PBS solutions, respectively.

electrode in alkaline and neutral solutions. Hence, CoP/Co₂P@NC/Ti-10-350 electrode is a promising electrocatalyst for the HER over a broad pH range.

Density Functional Theory Calculations

A series of density functional theory (DFT) calculations were carried out by building the relevant theoretical models (Figures S31, S32, and 7A) to gain insight into the high HER activity of the CoP/Co₂P@NC/Ti-10-350 electrode. It has been proved that the adsorption free energy of H (ΔG_{H}^*) is an appropriate parameter for evaluating the HER activity of a catalyst. A catalyst that gives $\Delta G_{\text{H}}^* \approx 0$ is considered as a promising candidate to catalyze the HER process, as it can achieve a fast proton/electron transfer step as well as a fast hydrogen release process (Liu et al., 2015). As the CoP/Co₂P@NC/Ti electrode is composed of CoP (200) facets along with a small fraction of exposed facets of (112) and (211) planes as well as the exposed facets of Co₂P (121) planes, we calculated the ΔG_{H}^* value on the (100), (112), and (211) planes of CoP@NC and the (121) plane of Co₂P@NC. For comparison, calculations for these planes encapsulated with carbon (CoP(100), CoP(112), and CoP(211)@C), (Co₂P (121), CoP(100), CoP(112), CoP(211), and Co₂P(121)@C) were also conducted. The calculated free energy profiles of the HER on different cobalt phosphide catalysts are presented in Figure 7B. The computational results show that the (100) surface of CoP and (121) surface of Co₂P give large exothermic ΔG_{H}^* values of -0.89 eV and -0.67 eV, respectively, which are lower than the relevant ΔG_{H}^* on the (211) and (112) planes of CoP (-0.51 and -0.20 V). The surfaces of CoP (100) and Co₂P (121) planes should therefore exhibit a low HER activity performance because of the foreseeable difficulty of hydrogen release.

After being dispersed in a carbon matrix, the ΔG_{H}^* values of the obtained CoP(112)@C and CoP(211)@C are surprisingly large and endothermic, with values of 1.03 and 1.01 eV, respectively. In contrast, the Co₂P(121)@C and CoP(100)@C have low endothermic ΔG_{H}^* values of 0.15 and 0 eV, respectively, which are more favorable to catalyze the HER process. This change could be caused by the strong coupling effect between C atoms and Co₂P(121) and CoP(100) in the CoP/Co₂P@NC/Ti electrode. The ΔG_{H}^* values of CoP(112)@NC (0.19 eV) and

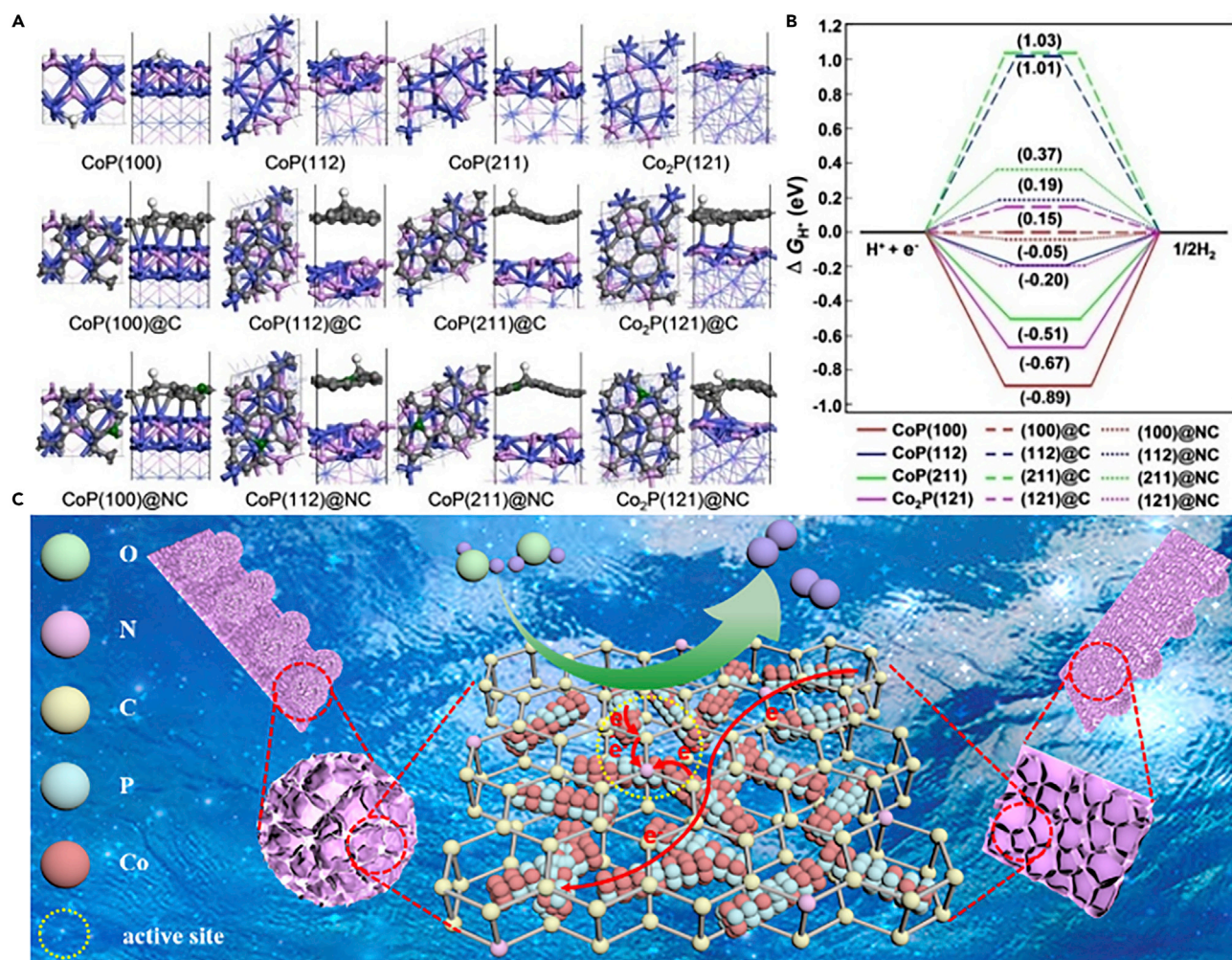


Figure 7. DFT Calculations and Schematic Illustration for CoP/Co₂P@NC/Ti

(A) The top and side view structures of H atom adsorptions on the different surface models; the Co, P, C, N, and H atoms are given in blue, pink, gray, green, and white, respectively.

(B) The calculated free energy profiles of the HER on different cobalt phosphide catalysts.

(C) Schematic illustration shows structural features and strong synergistic effects for modulating the local electronic structure of CoP/Co₂P@NC/Ti electrode for enhancing electrocatalytic HER.

CoP(211)@NC (0.37 eV) are much smaller than those of CoP(112)@C and CoP(211)@C, indicating that the N dopants introduced into the carbon matrix can reduce the value of ΔG_{H^*} and improve the electrocatalytic HER performance. Introducing N dopants in Co₂P(121)@C leads to a small exothermic ΔG_{H^*} of -0.20 V for Co₂P(121)@NC, which is still suitable for promoting the HER. In particular, due to the chemical bonding between CoP(100) and the NC matrix, the CoP(100)@NC exhibits an optimal ΔG_{H^*} value of -0.05 eV. These calculation results suggest that the CoP/Co₂P@NC/Ti electrode should possess the highest catalytic activity for HER, which is in good agreement with the experimental results. Thus the DFT calculations corroborate that the CoP/Co₂P@NC/Ti electrode composed of the CoP nanocrystals with (200) facets as the predominately exposed surface (and a fraction of (112) and (211) exposed planes) and Co₂P nanocrystals with the (121) plane as the predominately exposed surface should be highly efficient HER electrocatalysts. The calculation results also indicate that for the CoP/Co₂P@NC/Ti electrode, the C atoms above CoP(100) and Co₂P(121) adjacent to the N dopants are the most effective active sites, and that their HER activities should be higher than those of the C atoms above CoP(211) and CoP(112) adjacent to the N dopants.

Based on the aforementioned results, as illustrated in Figure 7C, several reasons are proposed to explain the superior electrocatalytic performance of the CoP/Co₂P@NC/Ti electrode for HER. The enhanced

electrocatalytic activity and durability of the CoP/Co₂P@NC/Ti electrode may be attributed to its unique open structure and interface bonding between the predominately exposed facets of cobalt phosphides and the NC matrix. First, the honeycomb structure provides highly open macropores with a mesoporous pore wall of NC matrix. CoP and Co₂P nanocrystals are dispersed in the matrix and readily accessible via the macro- and mesopores. This structure has a large interfacial contact area, which acts as the effective ECSA for HER, and facilitates the diffusion of hydrogen evolution-relevant species (e.g., H⁺, OH⁻, and H₂O) in electrolyte to the ECSA, and the transport of electrolyte ions, reaction intermediates, and products (e.g., H₂). The chemical bonding between the dispersed CoP and Co₂P nanocrystals with the NC matrix and the thickness of the honeycomb pore walls prevent agglomeration of the nanocrystals and thus loss of the ECSA, and provide stability to the electrocatalyst. The DFT simulation indicates that the synergistic effect of the high proportion of exposed facets of CoP (200) and the Co₂P (121) planes with the NC matrix of thin honeycomb pore walls can reduce the ΔG_{H^*} values to promote the adsorption of initial H* and yield super-active catalytic sites in thin honeycomb pore walls, which greatly enhances the HER activity. Second, the strong adhesion of the directly growing CoP/Co₂P@NC honeycomb layer and honeycomb microspheres to the Ti foil is beneficial for the electron transport within the current collectors and avoiding the sheltering of active sites, resulting in good mechanical and catalytic stability. Third, the NC matrix prevents the aggregation and undesired large-scale surface oxidation of the CoP and Co₂P nanocrystals (Huang et al., 2019).

DISCUSSION

In summary, we found that a honeycomb structured precursor of nitrate-hydroxide cobalt can be grown simultaneously on both sides of a Ti foil by dipping it in a mixture of Co(NO₃)₂·6H₂O and triethanolamine. Subsequent phosphidation converts the coated foil into Janus- or twin-type CoP/Co₂P@NC/Ti electrodes composed of NC nanosheet arrays assembled into a honeycomb layer with CoP/Co₂P single-crystal nanorods encapsulated. The morphology, structure, crystalline phase, and HER performance of these electrodes can be regulated by controlling the angle of Ti foils immersed in the precursor solution during the growth process. The electrode exhibits excellent electrocatalytic activity and good stability, outperforming most previously reported non-noble-metal HER electrodes. The unique open hierarchical porous structure of this catalyst and nanorods of CoP and Co₂P single crystals dispersed in the NC matrix of thin pore walls of honeycomb structure generate the largest effective ECSAs. The (200) planes of CoP crystals and (121) planes of Co₂P crystals interact with the NC matrix, resulting in the most efficient electrocatalytic sites for the HER. The synthesis approach can create the structural properties. The relationship between synthesis and structures, structure properties, and performance can be useful for the design of a large variety of bifunctional self-supported electrodes with transition metal oxides, nitrides, carbides, and phosphides for various electrocatalytic applications.

Limitations of the Study

In this work, we developed an efficient method to fabricate inch-size CoP/Co₂P-based 3D self-supported electrode for HER. Although excellent catalytic performance was explained by DFT calculations, advanced *in situ* techniques are required to reveal the synergistic effects between CoP/Co₂P and NC matrix for enhanced HER performance.

METHODS

All methods can be found in the accompanying [Transparent Methods supplemental file](#).

SUPPLEMENTAL INFORMATION

Supplemental Information can be found online at <https://doi.org/10.1016/j.isci.2020.101264>.

ACKNOWLEDGMENTS

This work was supported by NSFC (21661023, 21601096, 21802076, 21962013, and 21971129), Natural Science Foundation of Inner Mongolia Autonomous Region of China (2018BS05007), Application Program from Inner Mongolia Science and Technology Department (2016), Program of Higher-level Talents of IMU (21300-5185111), and Cooperation Project of State Key Laboratory of Baiyun Obo Rare Earth Resource Researches and Comprehensive Utilization (2017Z1950). We also gratefully acknowledge the financial support from the National Key R&D Program of China (2017YFA0208000), the National Natural Science Foundation of China (No. 21971117, 21522106), 111 Project (B18030) from China, the Open Funds

(RERU2019001) of the State Key Laboratory of Rare Earth Resource Utilization, the funding from Tianjin Key Lab for Rare Earth Materials and Applications (ZB19500202), and the Functional Research Funds for the Central Universities, Nankai University (63186005).

AUTHOR CONTRIBUTIONS

B.L., J.Zhang, and P.J. conceived the idea and designed the experiments. J.Zhang directed the project. B.C. and Y.C. carried out the experiments and the data analysis. R.G. carried out the DFT calculations. B.L. and B.C. wrote the original draft. J.Zhang, Y.D., and H.Z. corrected the manuscript. Y.D., X.S., A.O'M., H.Z., K.L., and J.Zhao assisted the analysis of the experiments data and the preparation of the manuscript. All authors contributed to the discussion and analysis of the data, as well as the editing of the manuscript.

DECLARATION OF INTERESTS

The authors declare no competing interests.

Received: April 29, 2020

Revised: May 21, 2020

Accepted: June 8, 2020

Published: July 24, 2020

REFERENCES

- Boppella, R., Tan, J., Yang, W., and Moon, J. (2019). Homologous CoP/NiCoP heterostructure on N-doped carbon for highly efficient and pH-universal hydrogen evolution electrocatalysis. *Adv. Funct. Mater.* 29, 1807976.
- Cao, B., Veith, G.M., Neuefeind, J.C., Adzic, R.R., and Khalifah, P.G. (2013). Mixed close-packed cobalt molybdenum nitrides as non-noble metal electrocatalysts for the hydrogen evolution reaction. *J. Am. Chem. Soc.* 135, 19186–19192.
- Cao, E., Chen, Z., Wu, H., Yu, P., Wang, Y., Xiao, F., Chen, S., Du, S., Xie, Y., Wu, Y., and Ren, Z. (2020). Boron-induced electronic-structure reformation of CoP nanoparticles drives enhanced pH-universal hydrogen evolution. *Angew. Chem. Int. Ed.* 59, 4154–4160.
- Chai, L., Hu, Z., Wang, X., Xu, Y., Zhang, L., Li, T.-T., Hu, Y., Qian, J., and Huang, S. (2020). Stringing bimetallic metal-organic framework-derived cobalt phosphide composite for high-efficiency overall water splitting. *Adv. Sci.* 7, 1903195.
- Chen, P., Xu, K., Tao, S., Zhou, T., Tong, Y., Ding, H., Zhang, L., Chu, W., Wu, C., and Xie, Y. (2016a). Phase-transformation engineering in cobalt diselenide realizing enhanced catalytic activity for hydrogen evolution in an alkaline medium. *Adv. Mater.* 28, 7527–7532.
- Chen, G.-F., Ma, T.Y., Liu, Z.-Q., Li, N., Su, Y.-Z., Davey, K., and Qiao, S.-Z. (2016b). Efficient and stable bifunctional electrocatalysts Ni/Ni²⁺M³⁺ (M = P, S) for overall water splitting. *Adv. Funct. Mater.* 26, 3314–3323.
- Chen, J., Liu, J., Xie, J.-Q., Ye, H., Fu, X.-Z., Sun, R., and Wong, C.-P. (2019). Co-Fe-P nanotubes electrocatalysts derived from metal-organic frameworks for efficient hydrogen evolution reaction under wide pH range. *Nano Energy* 56, 225–233.
- Chung, D.Y., Jun, S.W., Yoon, G., Kim, H., Yoo, J.M., Lee, K.-S., Kim, T., Shin, H., Sinha, A.K., Kwon, S.G., et al. (2017). Large-Scale Synthesis of carbon-shell-coated FeP nanoparticles for robust hydrogen evolution reaction electrocatalyst. *J. Am. Chem. Soc.* 139, 6669–6674.
- Deng, J., Ren, P., Deng, D., Yu, L., Yang, F., and Bao, X. (2014). Highly active and durable non-precious-metal catalysts encapsulated in carbon nanotubes for hydrogen evolution reaction. *Energy Environ. Sci.* 7, 1919–1923.
- Doan-Nguyen, V.V.T., Zhang, S., Trigg, E.B., Agarwal, R., Li, J., Su, D., Winey, K.I., and Murray, C.B. (2015). Synthesis and X-ray characterization of cobalt phosphide (Co₂P) nanorods for the oxygen reduction reaction. *ACS Nano* 9, 8108–8115.
- Du, H., Liu, Q., Cheng, N., Asiri, A.M., Sun, X., and Li, C.M. (2014). Template-assisted synthesis of CoP nanotubes to efficiently catalyze hydrogen-evolving reaction. *J. Mater. Chem. A* 2, 14812–14816.
- Fan, X., Zhou, H., and Guo, X. (2015). WC Nanocrystals grown on vertically aligned carbon nanotubes: an efficient and stable electrocatalyst for hydrogen evolution reaction. *ACS Nano* 9, 5125–5134.
- Gao, W., Yan, M., Cheung, H.-Y., Xia, Z., Zhou, X., Qin, Y., Wong, C.-Y., Ho, J.C., Chang, C.-R., and Qu, Y. (2017). Modulating electronic structure of CoP electrocatalysts towards enhanced hydrogen evolution by Ce chemical doping in both acidic and basic media. *Nano Energy* 38, 290–296.
- Guo, X., Wang, L., Yue, S., Wang, D., Lu, Y., Song, Y., and He, J. (2014). Single-crystalline organic-inorganic layered cobalt hydroxide nanofibers: facile synthesis, characterization, and reversible water-induced structural conversion. *Inorg. Chem.* 53, 12841–12847.
- Huang, X., Xu, X., Li, C., Wu, D., Cheng, D., and Cao, D. (2019). Vertical CoP nanoarray wrapped by N,P-doped carbon for hydrogen evolution reaction in both acidic and alkaline conditions. *Adv. Energy Mater.* 9, 1803970.
- Jiang, P., Liu, Q., Liang, Y., Tian, J., Asiri, A.M., and Sun, X. (2014). A cost-effective 3D hydrogen evolution cathode with high catalytic activity: FeP nanowire array as the active phase. *Angew. Chem. Int. Ed.* 53, 12855–12859.
- Jiao, L., Zhou, Y.-X., and Jiang, H.-L. (2016). Metal-organic framework-based CoP/reduced graphene oxide: high-performance bifunctional electrocatalyst for overall water splitting. *Chem. Sci.* 7, 1690–1695.
- Li, J.-S., Wang, Y., Liu, C.-H., Li, S.-L., Wang, Y.-G., Dong, L.-Z., Dai, Z.-H., Li, Y.-F., and Lan, Y.-Q. (2016). Coupled molybdenum carbide and reduced graphene oxide electrocatalysts for efficient hydrogen evolution. *Nat. Commun.* 7, 11204.
- Li, H., Zhao, X., Liu, H., Chen, S., Yang, X., Lv, C., Zhang, H., She, X., and Yang, D. (2018a). Sub-1.5 nm ultrathin CoP nanosheet aerogel: efficient electrocatalyst for hydrogen evolution reaction at all pH values. *Small* 14, 1802824.
- Li, H., Li, Q., Wen, P., Williams, T.B., Adhikari, S., Dun, C., Lu, C., Itanze, D., Jiang, L., Carroll, D.L., et al. (2018b). Colloidal cobalt phosphide nanocrystals as trifunctional electrocatalysts for overall water splitting powered by a zinc-air battery. *Adv. Mater.* 30, 1705796.
- Liu, Q., Tian, J., Cui, W., Jiang, P., Cheng, N., Asiri, A.M., and Sun, X. (2014). Carbon nanotubes decorated with CoP nanocrystals: a highly active non-noble-metal nanohybrid electrocatalyst for hydrogen evolution. *Angew. Chem. Int. Ed.* 53, 6710–6714.
- Liu, Y., Yu, G., Li, G.-D., Sun, Y., Asefa, T., Chen, W., and Zou, X. (2015). Coupling Mo₂C with

nitrogen-rich nanocarbon leads to efficient hydrogen-evolution electrocatalytic sites. *Angew. Chem. Int. Ed.* 54, 10752–10757.

Liu, T., Liu, D., Qu, F., Wang, D., Zhang, L., Ge, R., Hao, S., Ma, Y., Du, G., Asiri, A.M., et al. (2017a). Enhanced electrocatalysis for energy-efficient hydrogen production over CoP catalyst with nonelectroactive Zn as a promoter. *Adv. Energy Mater.* 7, 1700020.

Liu, B., Zhao, Y.-F., Peng, H.-Q., Zhang, Z.-Y., Sit, C.-K., Yuen, M.-F., Zhang, T.-R., Lee, C.-S., and Zhang, W.-J. (2017b). Nickel-cobalt diselenide 3D mesoporous nanosheet networks supported on Ni foam: an all-pH highly efficient integrated electrocatalyst for hydrogen evolution. *Adv. Mater.* 29, 1606521.

Liu, C., Ma, Z., Cui, M., Zhang, Z., Zhang, X., Su, D., Murray, C.B., Wang, J.X., and Zhang, S. (2018). Favorable core/shell interface within Co₂P/Pt nanorods for oxygen reduction electrocatalysis. *Nano Lett.* 18, 7870–7875.

Lu, Q., Yu, Y., Ma, Q., Chen, B., and Zhang, H. (2016). 2D transition-metal-dichalcogenide-nanosheet-based composites for photocatalytic and electrocatalytic hydrogen evolution reactions. *Adv. Mater.* 28, 1917–1933.

Lu, X.F., Yu, L., Zhang, J., and Lou, X.W. (2019). Ultrafine dual-phased carbide nanocrystals confined in porous nitrogen-doped carbon dodecahedrons for efficient hydrogen evolution reaction. *Adv. Mater.* 31, 1900699.

Ma, Y.-Y., Wu, C.-X., Feng, X.-J., Tan, H.-Q., Yan, L.-K., Liu, Y., Kang, Z.-H., Wang, E.-B., and Li, Y.-G. (2017). Highly efficient hydrogen evolution from seawater by a low-cost and stable CoMoP@C electrocatalyst superior to Pt/C. *Energy Environ. Sci.* 10, 788–798.

Ma, J., Wang, M., Lei, G., Zhang, G., Zhang, F., Peng, W., Fan, X., and Li, Y. (2018). Polyaniline derived N-doped carbon-coated cobalt phosphide nanoparticles deposited on N-doped graphene as an efficient electrocatalyst for hydrogen evolution reaction. *Small* 14, 1702895.

Pan, Y., Sun, K., Liu, S., Cao, X., Wu, K., Cheong, W.-C., Chen, Z., Wang, Y., Li, Y., Liu, Y., et al. (2018). Core-shell ZIF-8@ZIF-67-derived CoP nanoparticle-embedded N-doped carbon nanotube hollow polyhedron for efficient overall water splitting. *J. Am. Chem. Soc.* 140, 2610–2618.

Popczun, E.J., McKone, J.R., Read, C.G., Biacchi, A.J., Wiltrout, A.M., Lewis, N.S., and Schaak, R.E. (2013). Nanostructured nickel phosphide as an electrocatalyst for the hydrogen evolution reaction. *J. Am. Chem. Soc.* 135, 9267–9270.

Pu, Z., Amiin, I.S., Kou, Z., Li, W., and Mu, S. (2017). RuP₂-based catalysts with platinum-like activity and higher durability for the hydrogen evolution reaction at all pH values. *Angew. Chem. Int. Ed.* 56, 11559–11564.

Qu, K., Zheng, Y., Zhang, X., Davey, K., Dai, S., and Qiao, S.Z. (2017). Promotion of electrocatalytic hydrogen evolution reaction on nitrogen-doped carbon nanosheets with secondary heteroatoms. *ACS Nano* 11, 7293–7300.

Shi, Y., and Zhang, B. (2016). Recent advances in transition metal phosphide nanomaterials: synthesis and applications in hydrogen evolution reaction. *Chem. Soc. Rev.* 45, 1529–1541.

Staszak-Jirkovský, J., Malliakas, C.D., Lopes, P.P., Danilovic, N., Kota, S.S., Chang, K.-C., Genorio, B., Strmcnik, D., Stamenkovic, V.R., Kanatzidis, M.G., and Markovic, N.M. (2016). Design of active and stable Co-Mo-Sx chalcogenides as pH-universal catalysts for the hydrogen evolution reaction. *Nat. Mater.* 15, 197–203.

Sun, H., Yan, Z., Liu, F., Xu, W., Cheng, F., and Chen, J. (2020). Self-supported transition-metal-based electrocatalysts for hydrogen and oxygen evolution. *Adv. Mater.* 32, 1806326.

Tan, Y., Wang, H., Liu, P., Shen, Y., Cheng, C., Hirata, A., Fujita, T., Tang, Z., and Chen, M. (2016). Versatile nanoporous bimetallic phosphides towards electrochemical water splitting. *Energy Environ. Sci.* 9, 2257–2261.

Tang, C., Gan, L., Zhang, R., Lu, W., Jiang, X., Asiri, A.M., Sun, X., Wang, J., and Chen, L. (2016). Ternary Fe_xCo_{1-x}P nanowire array as a robust hydrogen evolution reaction electrocatalyst with Pt-like activity: experimental and theoretical insight. *Nano Lett.* 16, 6617–6621.

Tang, C., Zhang, R., Lu, W., He, L., Jiang, X., Asiri, A.M., and Sun, X. (2017). Fe-doped CoP nanoarray: a monolithic multifunctional catalyst for highly efficient hydrogen generation. *Adv. Mater.* 29, 1602441.

Tian, J., Liu, Q., Asiri, A.M., and Sun, X. (2014). Self-supported nanoporous cobalt phosphide nanowire arrays: an efficient 3D hydrogen-evolving cathode over the wide range of pH 0–14. *J. Am. Chem. Soc.* 136, 7587–7590.

Turner, J.A. (2004). Sustainable hydrogen production. *Science* 305, 972–974.

Vigil, J.A., Lambert, T.N., and Christensen, B.T. (2016). Cobalt phosphide-based nanoparticles as bifunctional electrocatalysts for alkaline water splitting. *J. Mater. Chem. A* 4, 7549–7554.

Wang, X.-D., Xu, Y.-F., Rao, H.-S., Xu, W.-J., Chen, H.-Y., Zhang, W.-X., Kuang, D.-B., and Su, C.-Y. (2016). Novel porous molybdenum tungsten phosphide hybrid nanosheets on carbon cloth for efficient hydrogen evolution. *Energy Environ. Sci.* 9, 1468–1675.

Wang, Y., Kong, B., Zhao, D., Wang, H., and Selomulya, C. (2017a). Strategies for developing transition metal phosphides as heterogeneous electrocatalysts for water splitting. *Nano Today* 15, 26–55.

Wang, H., Min, S., Wang, Q., Li, D., Casillas, G., Ma, C., Li, Y., Liu, Z., Li, L.-J., Yuan, J., et al. (2017b). Nitrogen-doped nanoporous carbon membranes with Co/CoP janus-type nanocrystals as hydrogen evolution electrode in both acidic and alkaline environments. *ACS Nano* 11, 4358–4364.

Wu, C., Yang, Y., Dong, D., Zhang, Y., and Li, J. (2017). In situ coupling of CoP polyhedrons and carbon nanotubes as highly efficient hydrogen evolution reaction electrocatalyst. *Small* 13, 1602873.

Xu, K., Cheng, H., Lv, H., Wang, J., Liu, L., Liu, S., Wu, X., Chu, W., Wu, C., and Xie, Y. (2018). Controllable surface reorganization engineering on cobalt phosphide nanowire arrays for efficient alkaline hydrogen evolution reaction. *Adv. Mater.* 30, 1703322.

Xue, Z.-H., Su, H., Yu, Q.-Y., Zhang, B., Wang, H.-H., Li, X.-H., and Chen, J.-S. (2017). Janus Co/CoP nanoparticles as efficient Mott-Schottky electrocatalysts for overall water splitting in wide pH range. *Adv. Energy Mater.* 7, 1602355.

Yang, L., Wang, K., Du, G., Zhu, W., Cui, L., Zhang, C., Sun, X., and Asiri, A.M. (2016). Cobalt phosphide nanowall arrays supported on carbon cloth: an efficient monolithic non-noble-metal hydrogen evolution catalyst. *Nanotechnology* 27, 475702.

Yang, F., Chen, Y., Cheng, G., Chen, S., and Luo, W. (2017). Ultrathin nitrogen-doped carbon coated with CoP for efficient hydrogen evolution. *ACS Catal.* 7, 3824–3831.

You, B., and Sun, Y. (2018). Innovative strategies for electrocatalytic water splitting. *Acc. Chem. Res.* 51, 1571–1580.

Yu, J., Li, Q., Li, Y., Xu, C.-Y., Zhen, L., David, V.P., and Wu, J. (2016). Ternary metal phosphide with triple-layered structure as a low-cost and efficient electrocatalyst for bifunctional water splitting. *Adv. Funct. Mater.* 26, 7644–7651.

Zhang, X., Lai, Z., Tan, C., and Zhang, H. (2016a). Solution-processed two-dimensional MoS₂ nanosheets: preparation, hybridization, and applications. *Angew. Chem. Int. Ed.* 55, 8816–8838.

Zhang, Y., Ouyang, B., Xu, J., Chen, S., Rawat, R.S., and Fan, H.J. (2016b). 3D porous hierarchical nickel-molybdenum nitrides synthesized by RF plasma as highly active and stable hydrogen-evolution-reaction electrocatalysts. *Adv. Energy Mater.* 6, 1600221.

Zhang, J., Qu, L., Shi, G., Liu, J., Chen, J., and Dai, L. (2016c). N,P-codoped carbon networks as efficient metal-free bifunctional catalysts for oxygen reduction and hydrogen evolution reactions. *Angew. Chem. Int. Ed.* 55, 2230–2234.

Zhang, R., Wang, X., Yu, S., Wen, T., Zhu, X., Yang, F., Sun, X., Wang, X., and Hu, W. (2017a). Ternary NiCo₂P_x nanowires as pH-universal electrocatalysts for highly efficient hydrogen evolution reaction. *Adv. Mater.* 29, 1605502.

Zhang, C., Huang, Y., Yu, Y., Zhang, J., Zhuo, S., and Zhang, B. (2017b). Sub-1.1 nm ultrathin porous CoP nanosheets with dominant reactive {200} facets: a high mass activity and efficient electrocatalyst for the hydrogen evolution reaction. *Chem. Sci.* 8, 2769–2775.

Zhang, R., Tang, C., Kong, R., Du, G., Asiri, A.M., Chen, L., and Sun, X. (2017c). Al-doped CoP nanoarray: a durable water-splitting electrocatalyst with superhigh activity. *Nanoscale* 9, 4793–4800.

Zhang, R., Ren, X., Hao, S., Ge, R., Liu, Z., Asiri, A.M., Chen, L., Zhang, Q., and Sun, X. (2018). Selective phosphidation: an effective strategy toward CoP/CeO₂ interface engineering for superior alkaline hydrogen evolution electrocatalysis. *J. Mater. Chem. A* 6, 1985–1990.

Zhang, Y., Li, N., Zhang, Z., Li, S., Cui, M., Ma, L., Zhou, H., Su, D., and Zhang, S. (2020). Programmable synthesis of multimetallic phosphide nanorods mediated by core/shell structure formation and conversion. *J. Am. Chem. Soc.* *142*, 8490–8497.

Zhou, Q., Shen, Z., Zhu, C., Li, J., Ding, Z., Wang, P., Pan, F., Zhang, Z., Ma, H., Wang, S., and

Zhang, H. (2018). Nitrogen-doped CoP electrocatalysts for coupled hydrogen evolution and sulfur generation with low energy consumption. *Adv. Mater.* *30*, 1800140.

Zhu, Y.-P., Liu, Y.-P., Ren, T.-Z., and Yuan, Z.-Y. (2015). Self-supported cobalt phosphide mesoporous nanorod arrays: a flexible and bifunctional electrode for highly active

electrocatalytic water reduction and oxidation. *Adv. Funct. Mater.* *25*, 7337–7347.

Zhuang, M., Ou, X., Dou, Y., Zhang, L., Zhang, Q., Wu, R., Ding, Y., Shao, M., and Luo, Z. (2016). Polymer-embedded fabrication of Co₂P nanoparticles encapsulated in N,P-doped graphene for hydrogen generation. *Nano Lett.* *16*, 4691–4698.

iScience, Volume 23

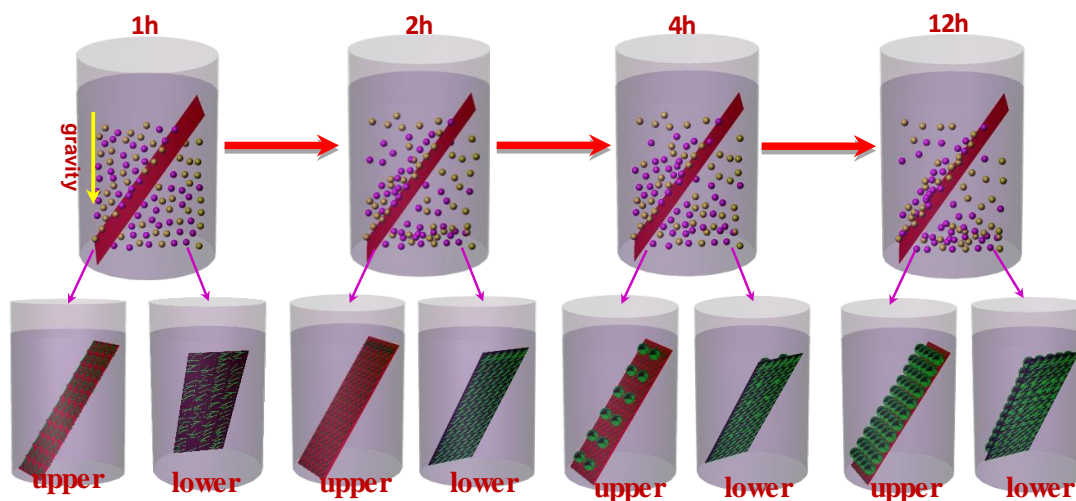
Supplemental Information

Ultrafine CoP/Co₂P Nanorods Encapsulated in Janus/Twins-type Honeycomb 3D Nitrogen-Doped Carbon Nano- sheets for Efficient Hydrogen Evolution

Baocang Liu, Bo Cao, Yan Cheng, Peng Jing, Jian Zhao, Rui Gao, Anthony. O'Mullane, Huaiyong Zhu, Kaiqiang Liu, Xiaolei Sun, Yaping Du, and Jun Zhang

Supplemental Information

1. Supplemental Figures



Scheme S1. Schematic illustration shows the growth process of honeycomb structure precursor grown on the two sides of Ti foil obtained at different reaction intervals during the deposition. Related to Figure 1.

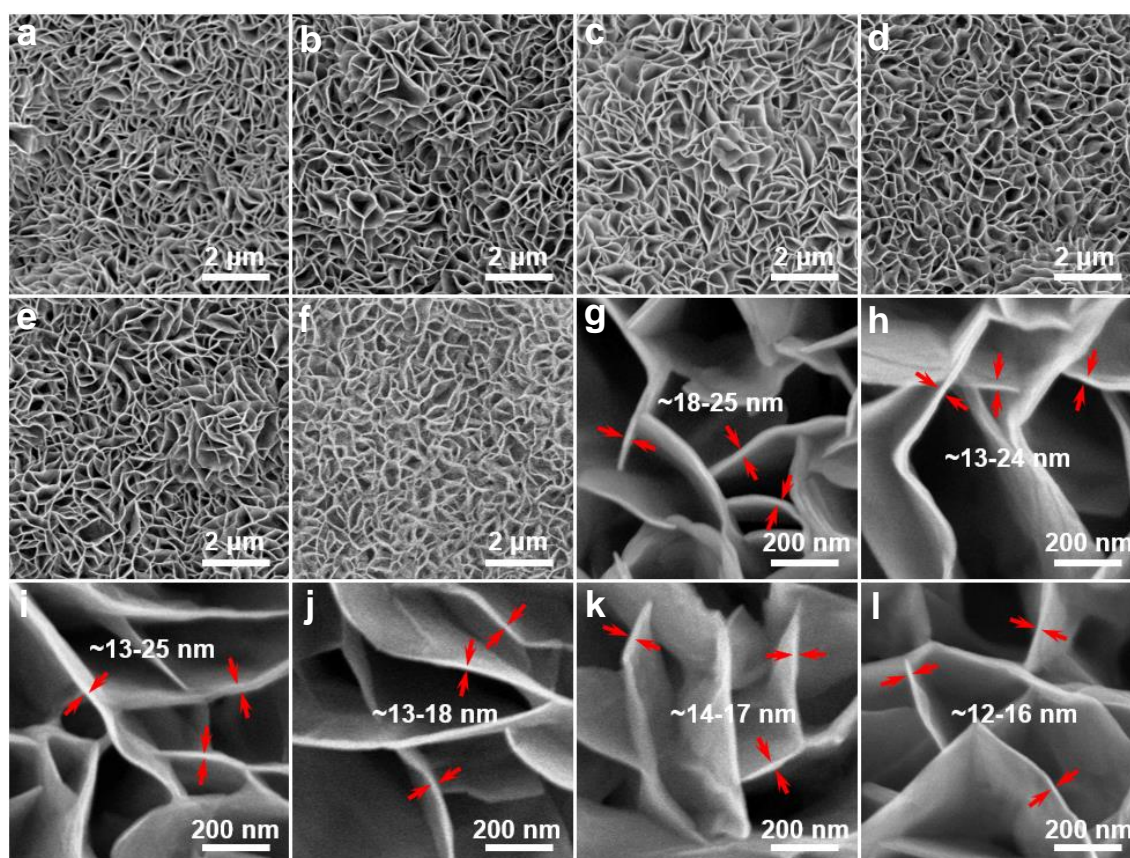


Figure S1. (a-f) SEM images of lamellar nitrate-hydroxide cobalt precursor of honeycomb structured layers for 0°, 10°, 30°, 50°, 70°, and 90°; (g-l) precursors with thin pore walls (~12-25 nm thickness) for 0° - 90°. Related to Figure 2.

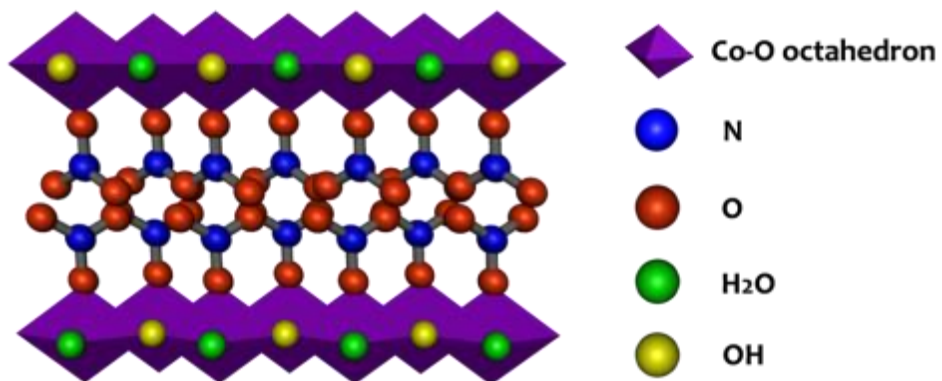


Figure S2. Schematic illustration of the structure of lamellar nitride-hydroxide cobalt ($\text{Co}(\text{OH})_x(\text{NO}_3)_{2-x} \cdot m\text{H}_2\text{O}$), in which H atoms are not shown. Related to Figure 2.

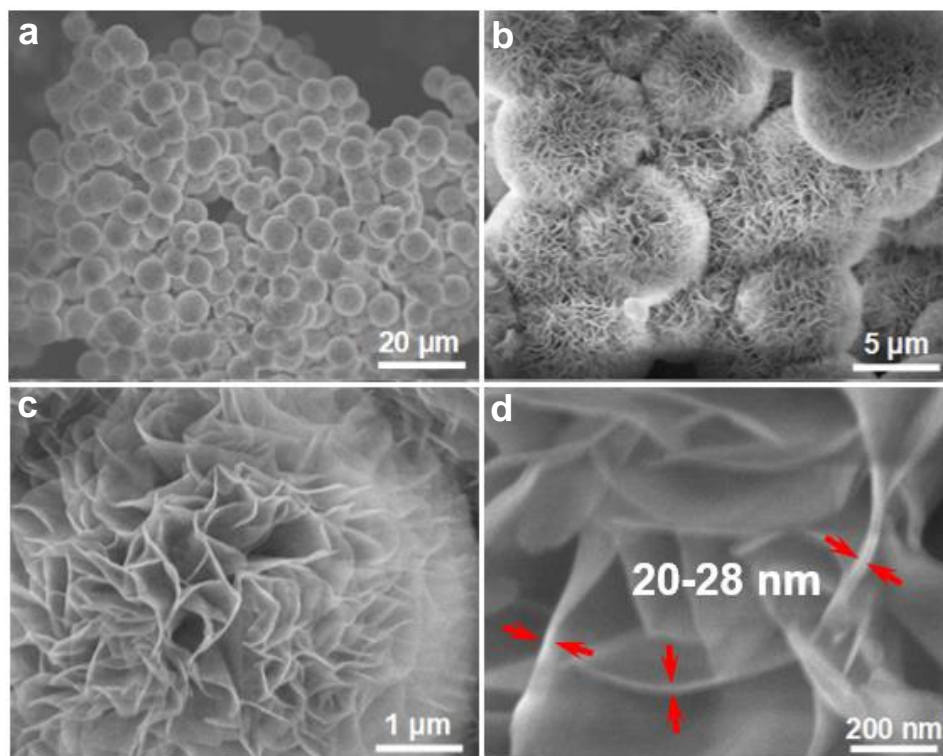


Figure S3. (a-d) SEM images of $\text{Co}(\text{OH})_x(\text{NO}_3)_{2-x} \cdot m\text{H}_2\text{O}$ precursor synthesized by low-temperature-solution strategy without using Ti foil. Related to Figure 2.

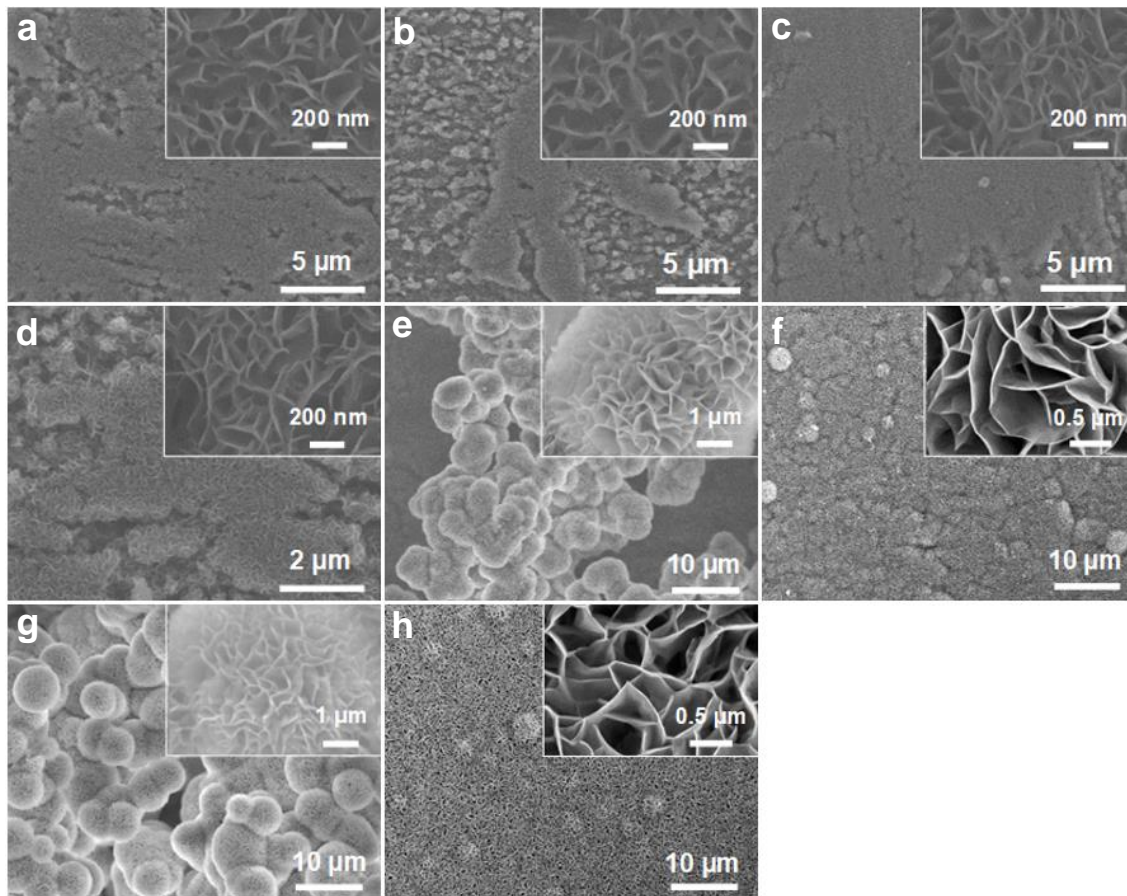


Figure S4. SEM images of honeycomb structure precursor grown on the two sides of Ti foil obtained at different reaction intervals during the deposition: (a) 1 h (upper surface), (b) 1 h (lower surface), (c) 2 h (upper surface), (d) 2 h (lower surface), (e) 4 h (upper surface), (f) 4 h (lower surface), (g) 12 h (upper surface), and (h) 12 h (lower surface). The placement angle of Ti foil in solution is 70° during the growth process. Related to Figure 2.

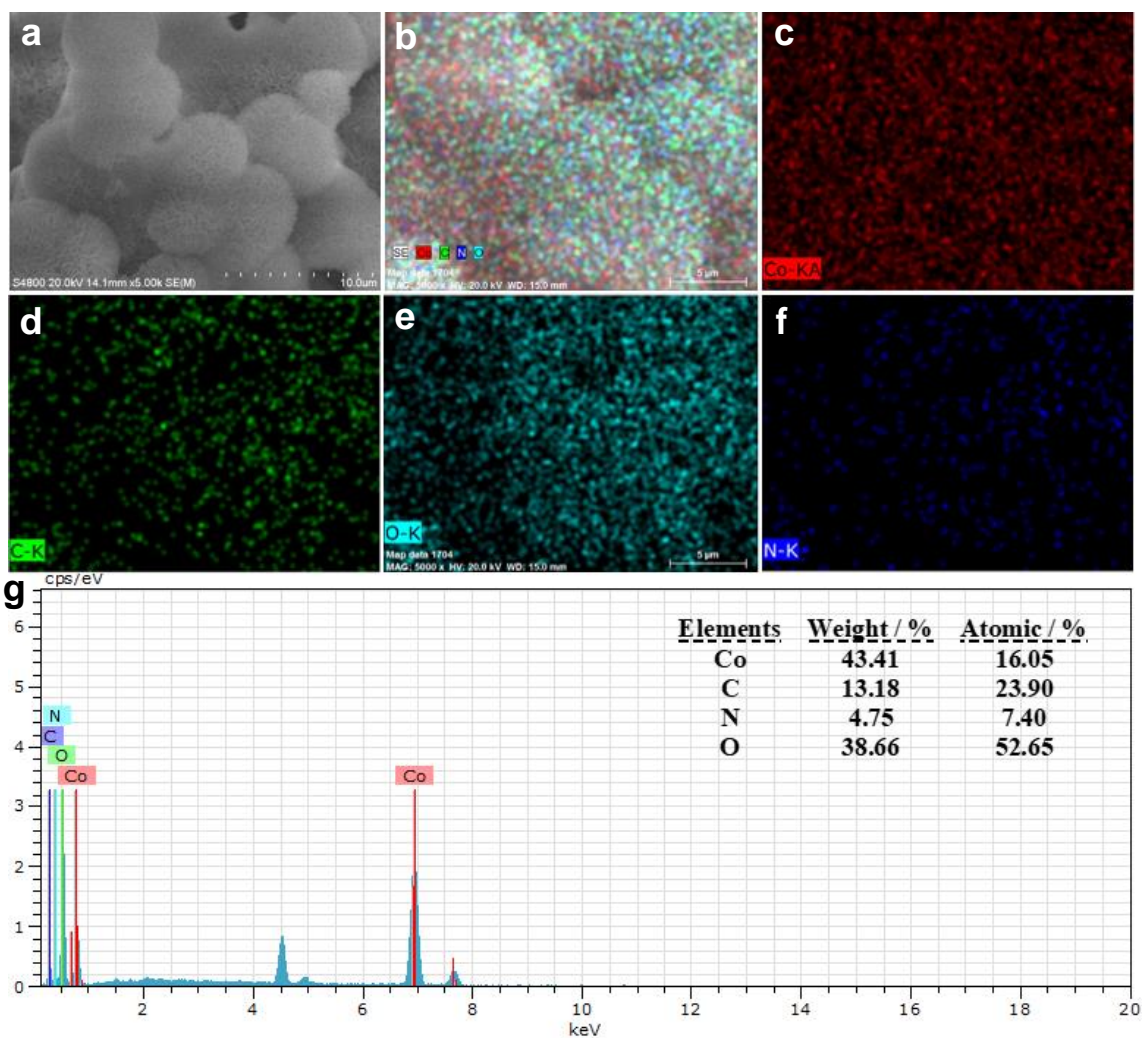


Figure S5. (a) SEM image of lamellar nitride-hydroxide cobalt precursor honeycomb microspheres; (b-f) the EDX elemental mapping images of the precursor microspheres showing the distributions of elements Co, C, O, and N; (g) EDX spectrum of the precursor microspheres. Related to Figure 2.

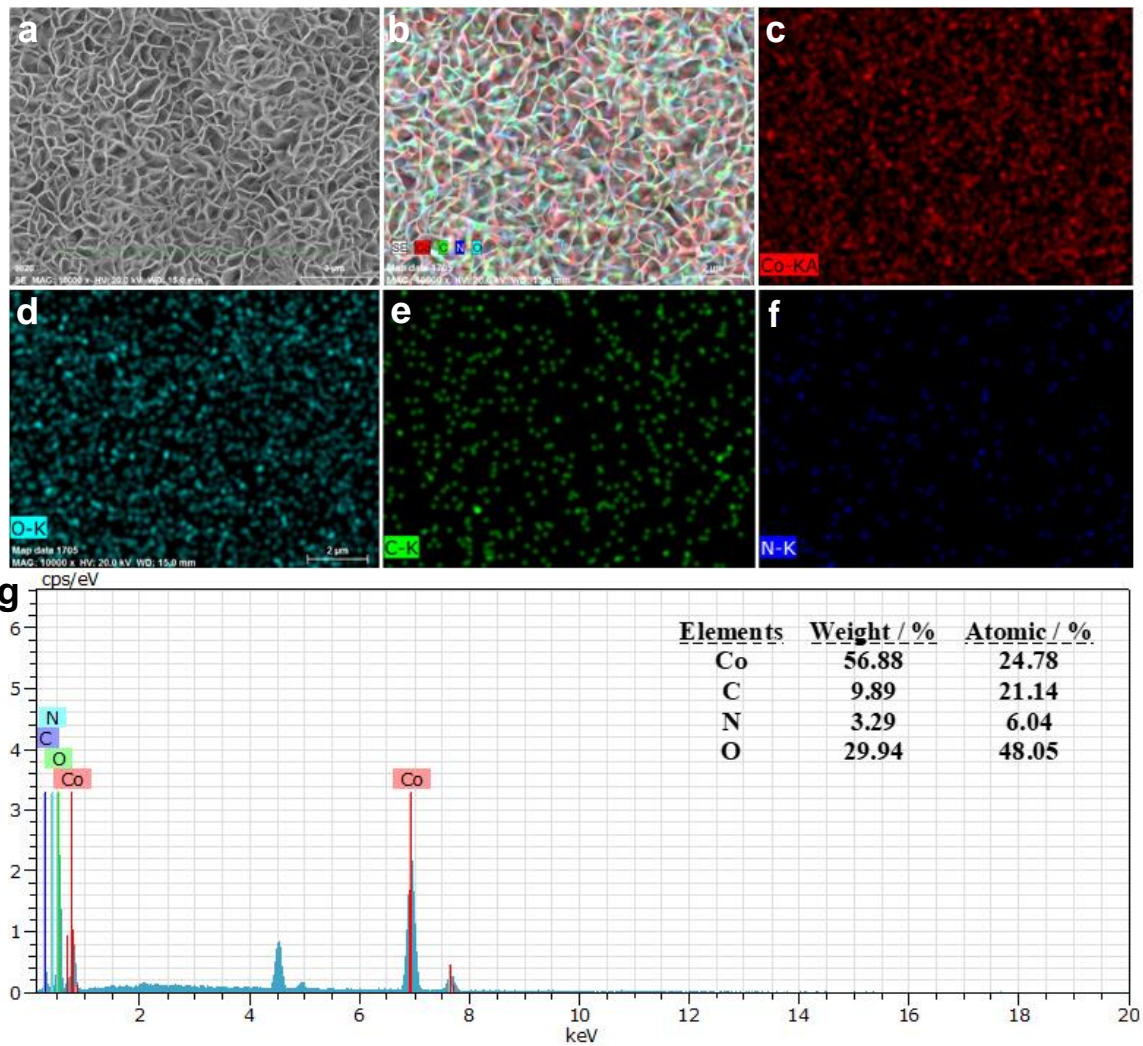


Figure S6. (a) SEM image of lamellar nitride-hydroxide cobalt precursor honeycomb layer; (b-f) the EDX elemental mapping images of the precursor layer showing the distributions of elements Co, C, O, and N; (g) EDX spectrum of the precursor layer. Related to Figure 2.

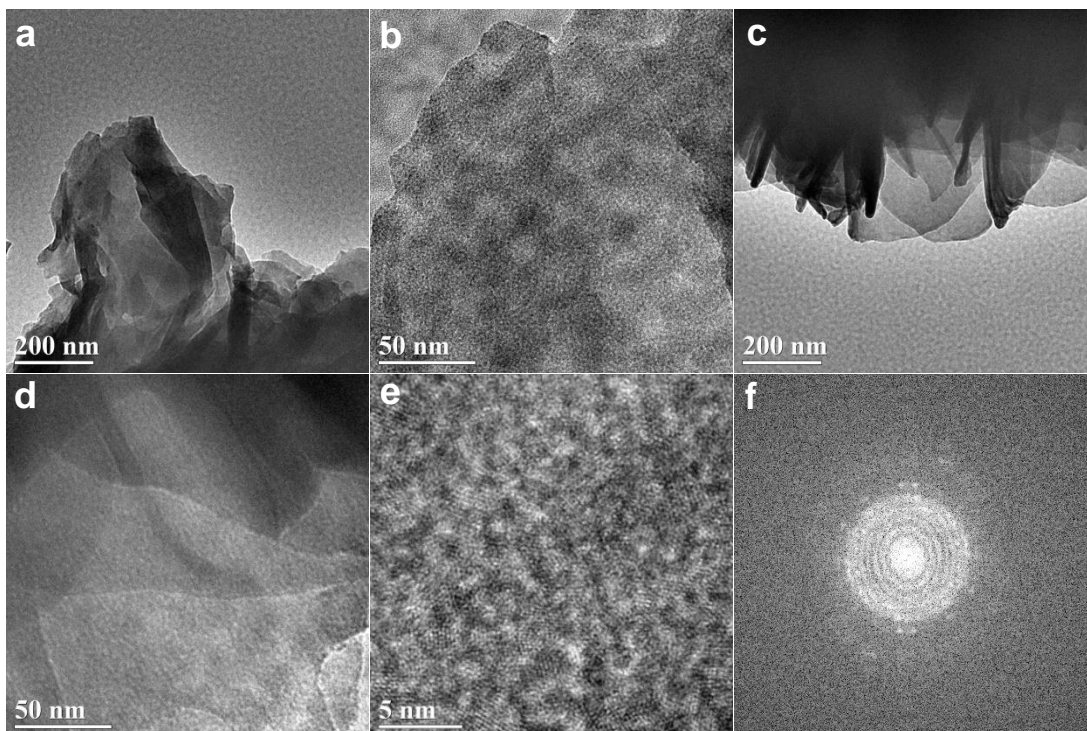


Figure S7. (a and b) TEM images of $\text{Co(OH)}_x(\text{NO}_3)_{2-x} \cdot m\text{H}_2\text{O}$ honeycomb layer scratched down from Ti foil; (c and d) TEM images of the scratched $\text{Co(OH)}_x(\text{NO}_3)_{2-x} \cdot m\text{H}_2\text{O}$ honeycomb microspheres; (e) HRTEM image of $\text{Co(OH)}_x(\text{NO}_3)_{2-x} \cdot m\text{H}_2\text{O}$ microspheres; (f) the corresponding fast transformation Fourier image. FFT image of the honeycomb layer is given and the image of honeycomb microspheres is the same and not shown. Related to Figure 2.

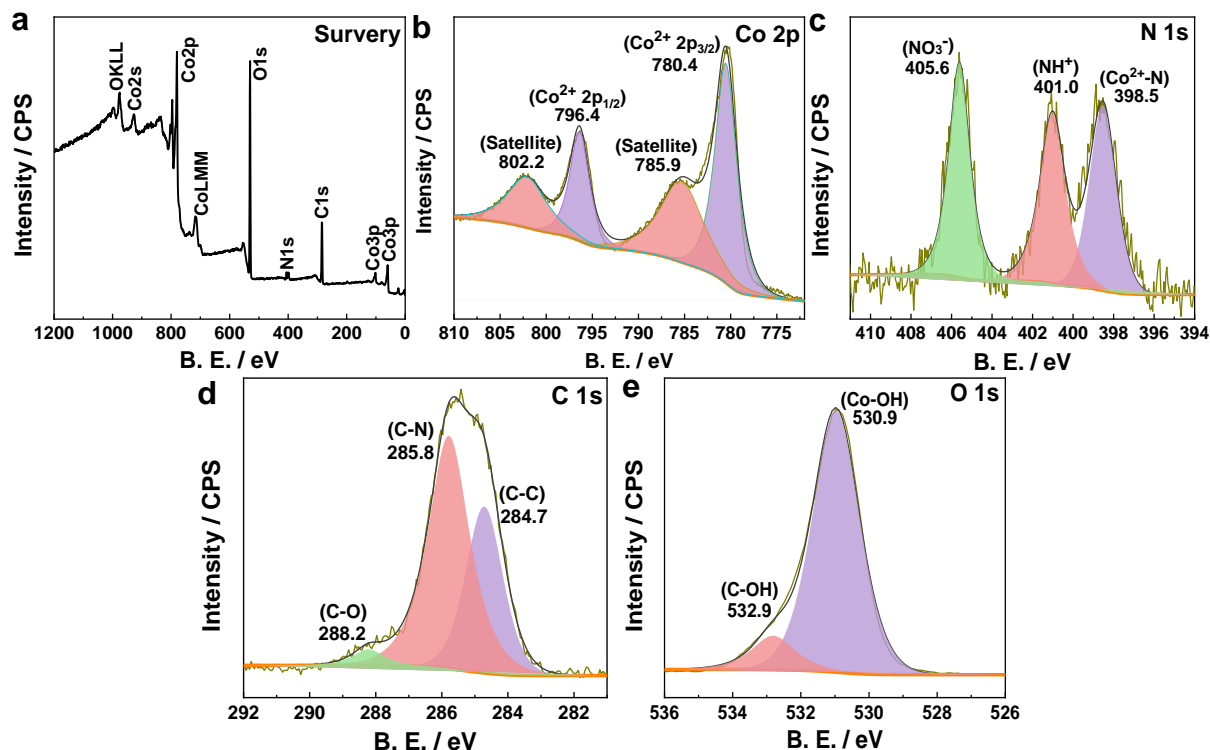


Figure S8. XPS of lamellar nitride-hydroxide cobalt precursor: (a) XPS survey scan and high resolution XPS spectra of (b) Co 2p, (c) N 1s, (d) C 1s, and (e) O 1s. Related to Figure 2.

X-ray photoelectron spectroscopy (XPS) of the precursor reveals the presence of Co, O, C, and N elements (Fig. S8a). In the Co 2p spectrum (Fig. S8b), the peak value differences between 780.4 and 796.4 eV is 16.0 eV in line with the spin orbit splitting values of Co 2p_{3/2} and Co 2p_{1/2}, suggesting that cobalt exists in the form of Co²⁺ (Zhang et al., 2017). The high-resolution XPS spectrum of the N1s core level exhibits three peaks at 405.6, 401.0, and 398.5 eV; they can be assigned to N-O, quaternary N, and Co²⁺-N species in NO₃⁻, protonated TEOA, and the TEOA cobalt complex, respectively (Fig. S8c). In the C 1s spectrum (Fig. S8d), two peaks at 285.2 and 288.2 eV can be attributed to carbon in C-N and C-O (Silva et al., 2013), confirming the presence of TEOA in the precursor. For O1s XPS spectrum (Fig. S8e), the peaks at 530.9 eV and 532.9 eV are observed, which are attributed to the -OH groups in cobalt hydroxide and TEOA, respectively.

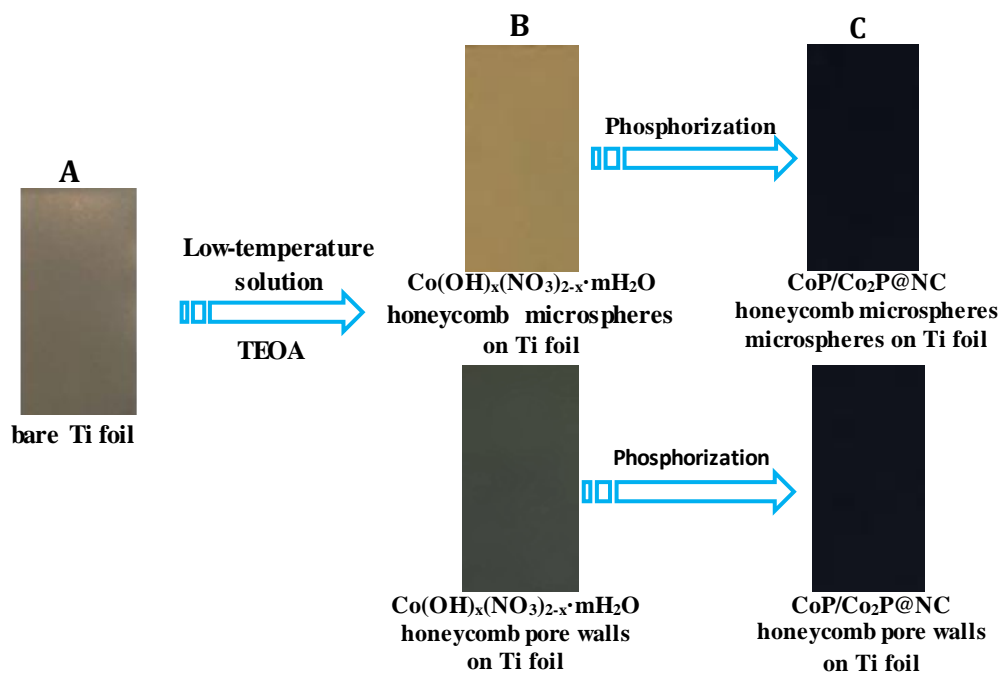


Figure S9. Optical photographs of (A) bare Ti foil, (B) $\text{Co(OH)}_x(\text{NO}_3)_{2-x} \cdot m\text{H}_2\text{O}$ -microspheres/Ti (upper) and $\text{Co(OH)}_x(\text{NO}_3)_{2-x} \cdot m\text{H}_2\text{O}$ -layer/Ti (bottom), and (C) CoP/Co₂P@NC-microspheres/Ti (upper) and CoP/Co₂P@NC-layer/Ti (bottom). Related to Figures 2 and 3.

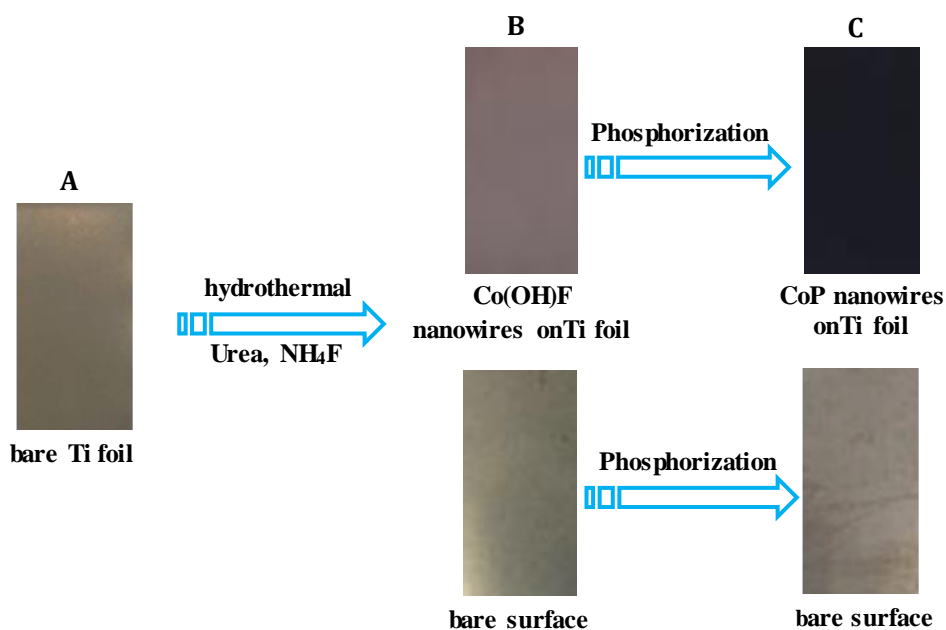


Figure S10. Optical photographs of (A) bare Ti foil, (B) Co(OH)F-NWs/Ti (upper) and bare surface Ti foil (bottom) and (C) CoP-NWs/Ti (upper) and bare surface Ti foil (bottom). Related to Figures 2 and 3.

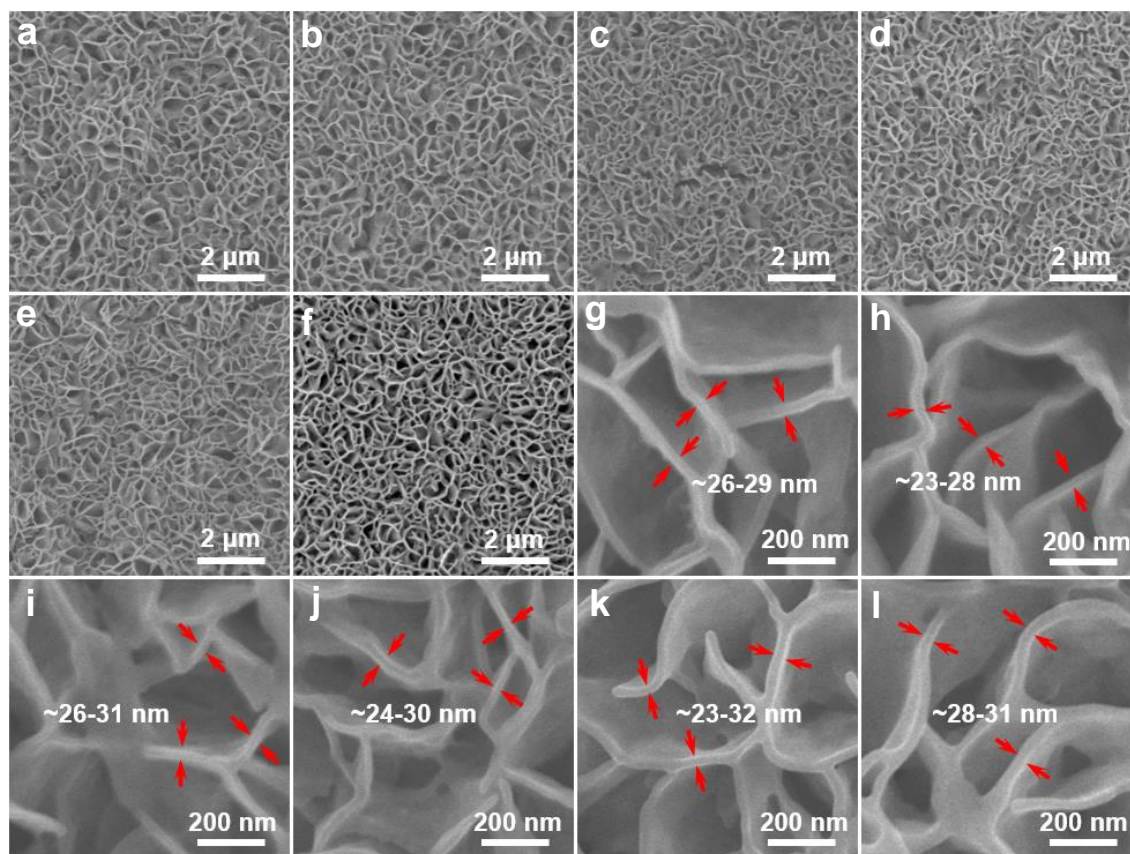


Figure S11. (a-f) SEM images of CoP/Co₂P@NC of honeycomb structured layer for 0°, 10°, 30°, 50°, 70°, and 90°; (g-l) CoP/Co₂P@NC honeycomb structured layer with thick pore walls (~23-32 nm thickness) for 0°-90°. Related to Figure 3.

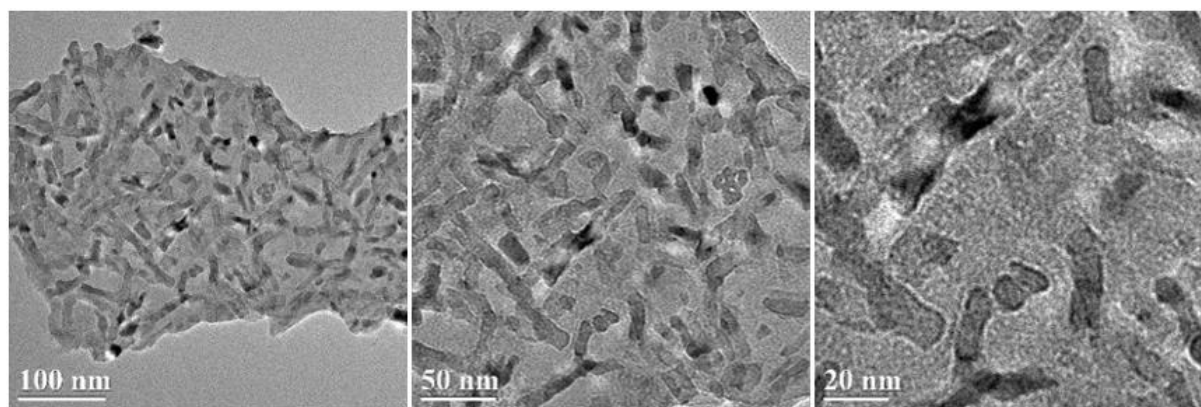


Figure S12. TEM images of the pore wall in CoP/Co₂P@NC specimen scratched down from CoP/Co₂P@NC/Ti-90-350 electrode. Related to Figure 3.

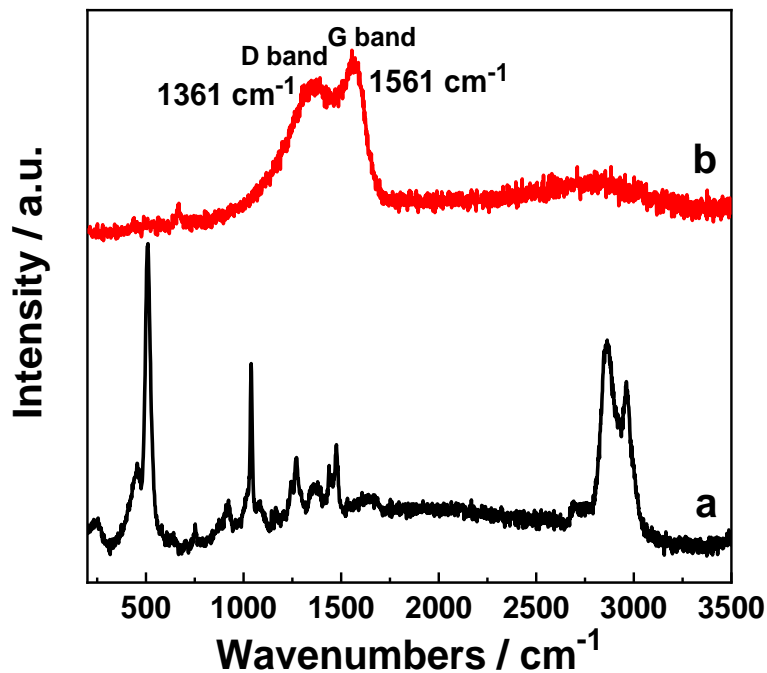


Figure S13. Raman spectra of (a) $\text{Co(OH)}_x(\text{NO}_3)_{2-x} \cdot m\text{H}_2\text{O}$ precursor and (b) $\text{CoP/Co}_2\text{P@NC-10-350}$ catalyst. Related to Figure 3.

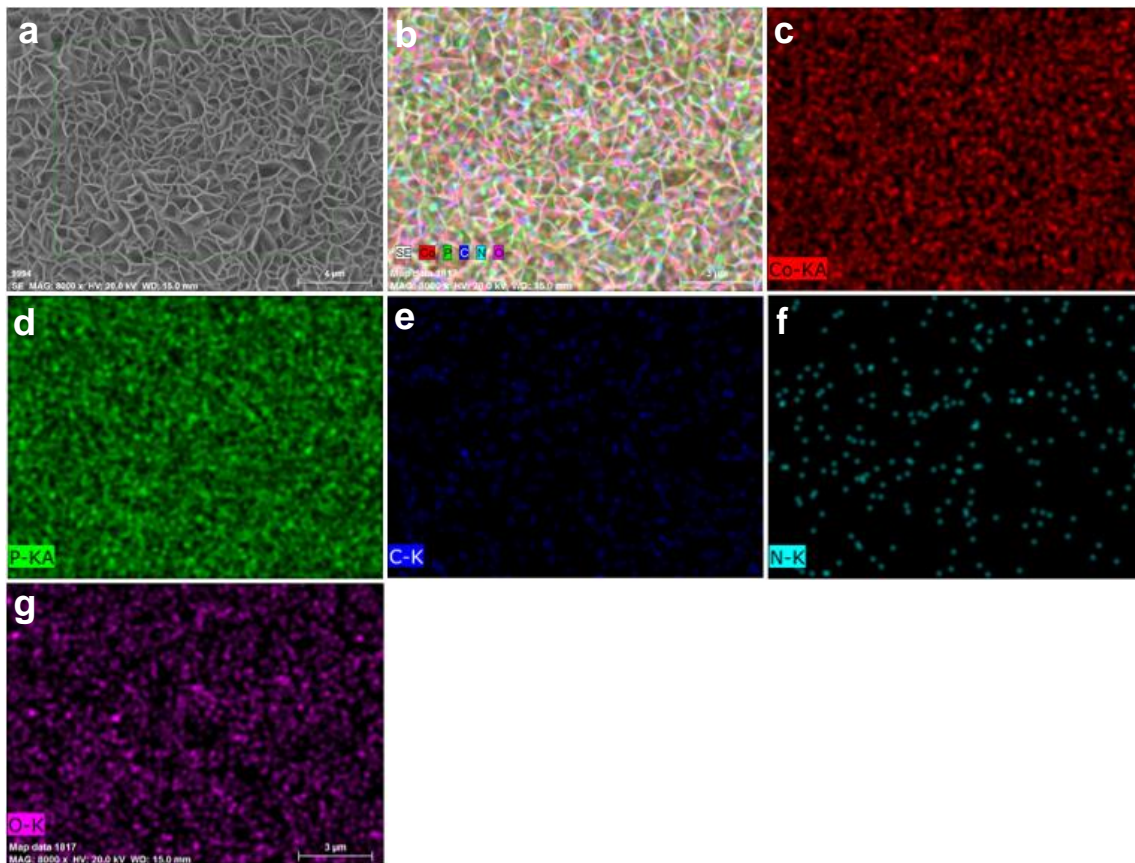


Figure S14. (a) SEM image of $\text{CoP/Co}_2\text{P@NC}$ honeycomb layer on Ti foil; (b-g) the EDX elemental mapping images of $\text{CoP/Co}_2\text{P@NC}$ layer on Ti foil showing the distributions of elements Co, P, C, N, and O. Related to Figure 3.

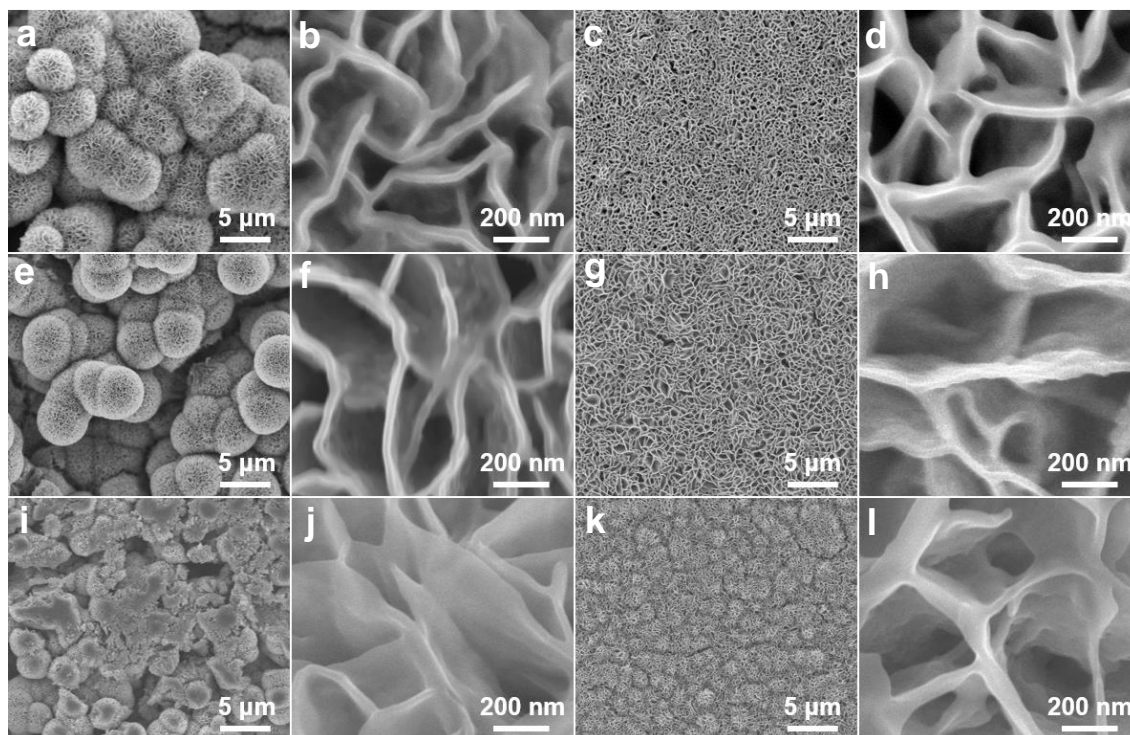


Figure S15. SEM images of CoP/Co₂P@NC honeycomb microspheres on Ti foil obtained at 300 °C (a, b), 400 °C (e, f), and 500 °C (i, j), respectively and SEM images of CoP/Co₂P@NC honeycomb layer on Ti foil obtained at 300 °C (c, d), 400 °C (g, h), and 500 °C (k, l), respectively. Related to Figure 3.

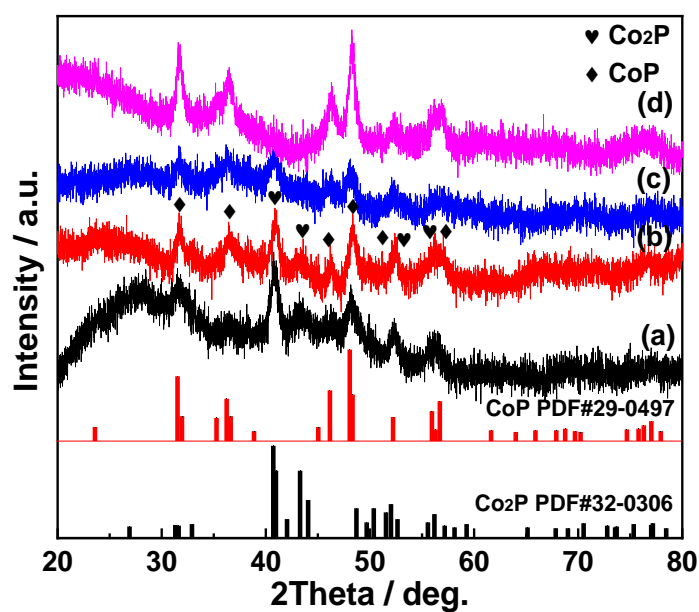


Figure S16. XRD patterns of (a) CoP/Co₂P@NC-10-300, (b) CoP/Co₂P@NC-10-350, (c) CoP/Co₂P@NC-10-400, and (d) CoP@NC-10-500 scratched down from Ti foil. Related to Figure 4.

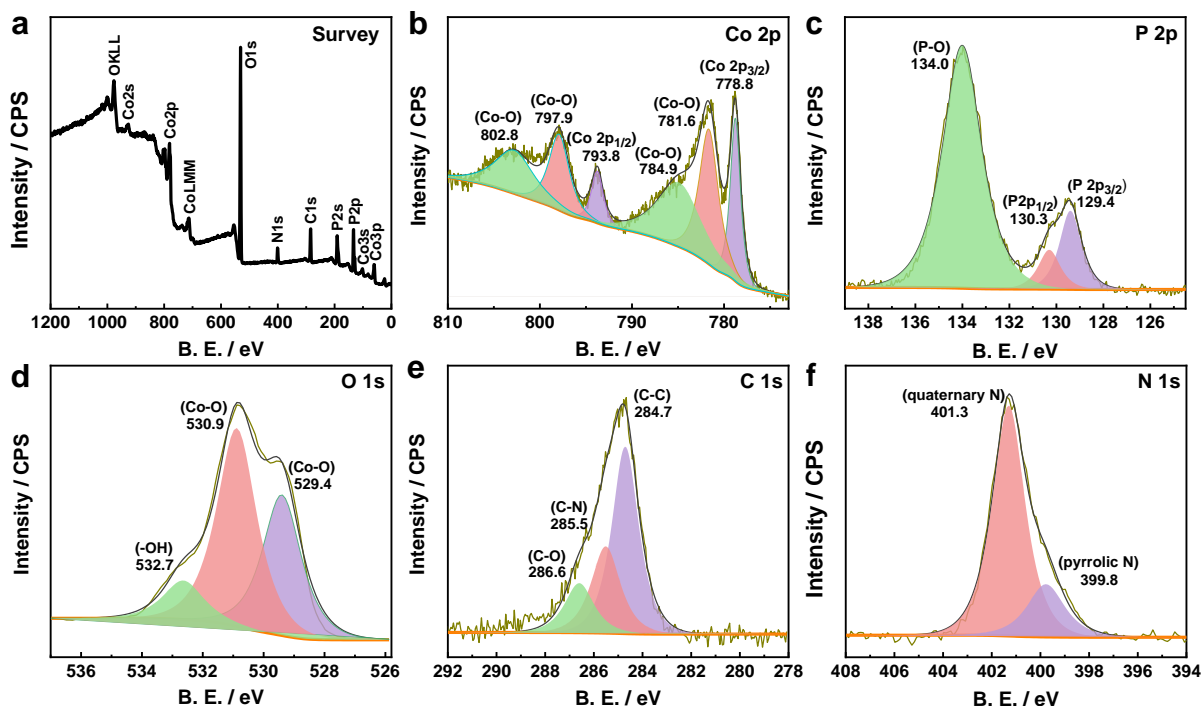


Figure S17. (a) Survey XPS spectrum of CoP/Co₂P@NC/Ti-10-350 electrode and high-resolution XPS spectra of (b) Co 2p, (c) P 2p, (d) O 1s, (e) C 1s, and (f) N 1s in CoP/Co₂P@NC/Ti-10-350 electrode. Related to Figure 4.

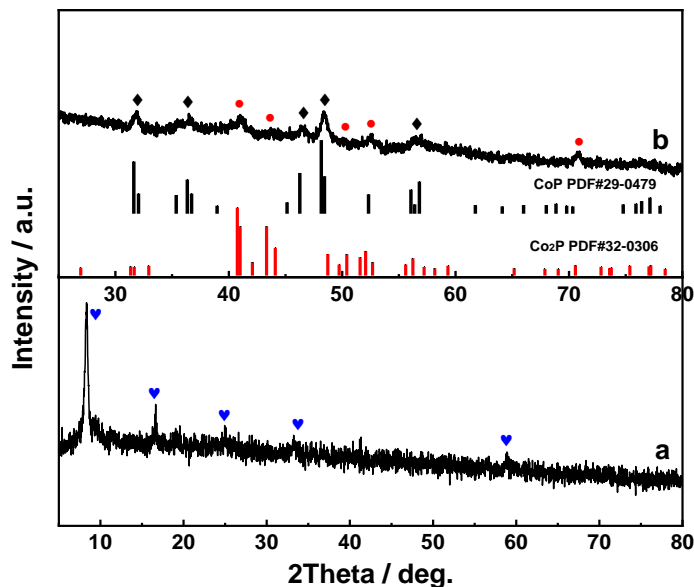


Figure S18. (a) XRD patterns of the Co(OH)_x(Cl)_{2-x}·mH₂O precursor and phosphatized product scratched from Ti foil (black diamonds represent the diffraction peaks from CoP; red circles correspond to the diffraction peaks from Co₂P; blue hearts signify the lamellar Co(OH)_x(Cl)_{2-x}·mH₂O precursor). Related to Figure 4.

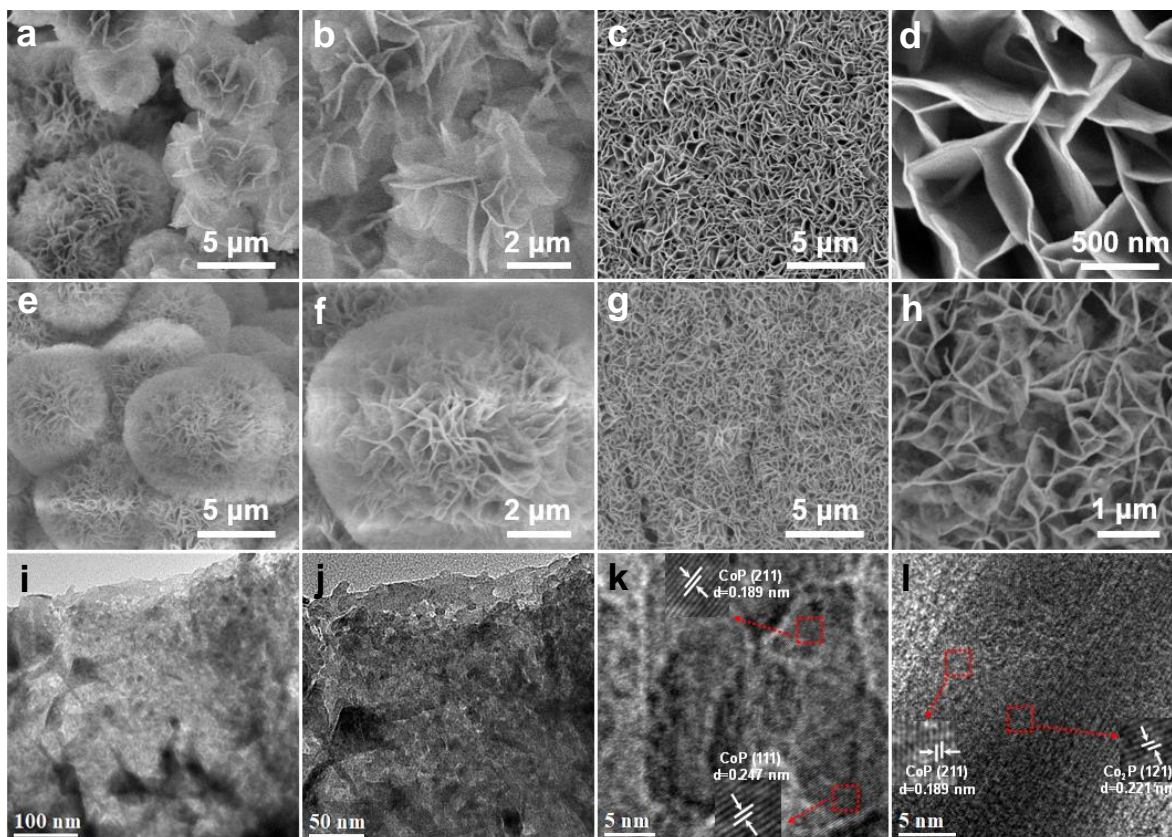


Figure S19. (a, b) SEM images of $\text{Co(OH)}_x(\text{Cl})_{2-x} \cdot m\text{H}_2\text{O}$ honeycomb microspheres on Ti foil; (c, d) SEM images of $\text{Co(OH)}_x(\text{Cl})_{2-x} \cdot m\text{H}_2\text{O}$ honeycomb layer on Ti foil; (e, f) SEM images of $\text{CoP/Co}_2\text{P@NC}$ honeycomb microspheres on Ti foil obtained at 350 °C; (g, h) SEM images of $\text{CoP/Co}_2\text{P@NC}$ honeycomb layer on Ti foil obtained at 350 °C; (i, g) TEM images of $\text{CoP/Co}_2\text{P@NC-10-350}$ scratched from Ti foil; (k, l) HRTEM image of $\text{CoP/Co}_2\text{P@NC-10-350}$. The $\text{CoP/Co}_2\text{P@NC}$ was synthesized by using $\text{Co(OH)}_x(\text{Cl})_{2-x} \cdot m\text{H}_2\text{O}$ as precursor. Related to Figure 4.

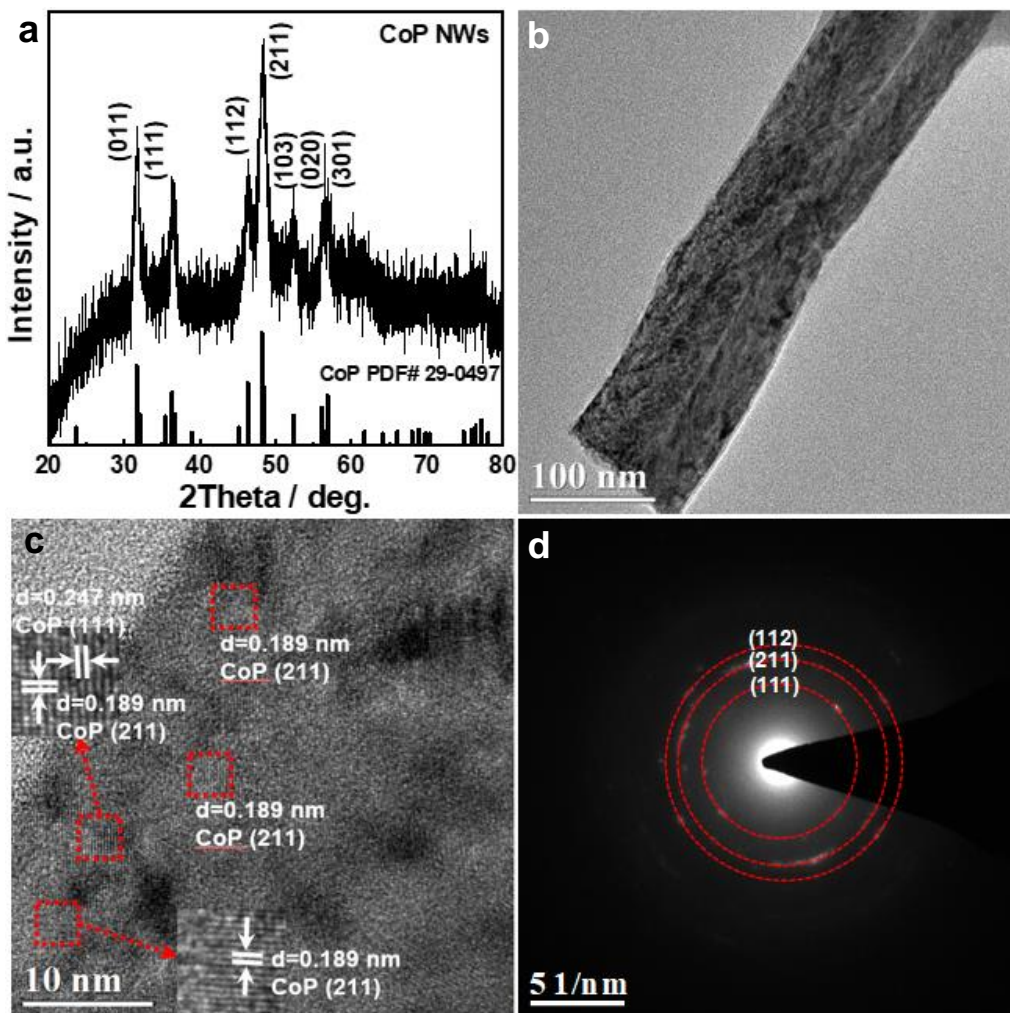


Figure S20. (a) XRD pattern of CoP specimen scratched down from Ti foil; (b) TEM images of CoP nanowires scratched down from Ti foil; (c) HRTEM image of CoP nanowires; (d) SAED pattern of CoP nanowires. The sample was synthesized by using urea as precipitant and NH_4F as etching agent. Related to Figure 4.

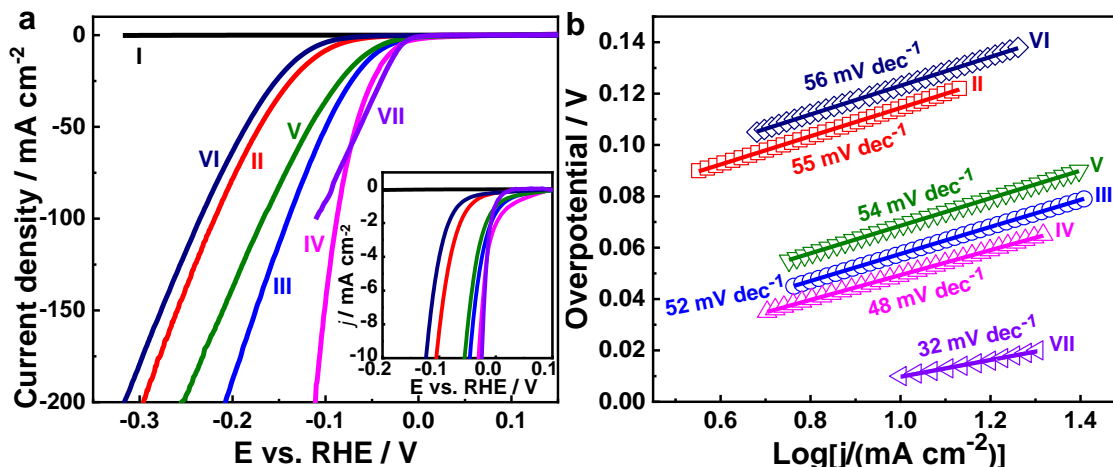


Figure S21. (a) LSV curves recorded at 2 mV s^{-1} and (b) Tafel plots of (I) bare Ti foil, (II) CoP-NWs/Ti, (III) CoP/Co₂P@NC/Ti-10-300, (IV) CoP/Co₂P@NC/Ti-10-350, (V) CoP/Co₂P@NC/Ti-10-400, (VI) CoP@NC/Ti-10-500, and (VII) Pt/C in $0.5 \text{ M H}_2\text{SO}_4$. Related to Figure 5.

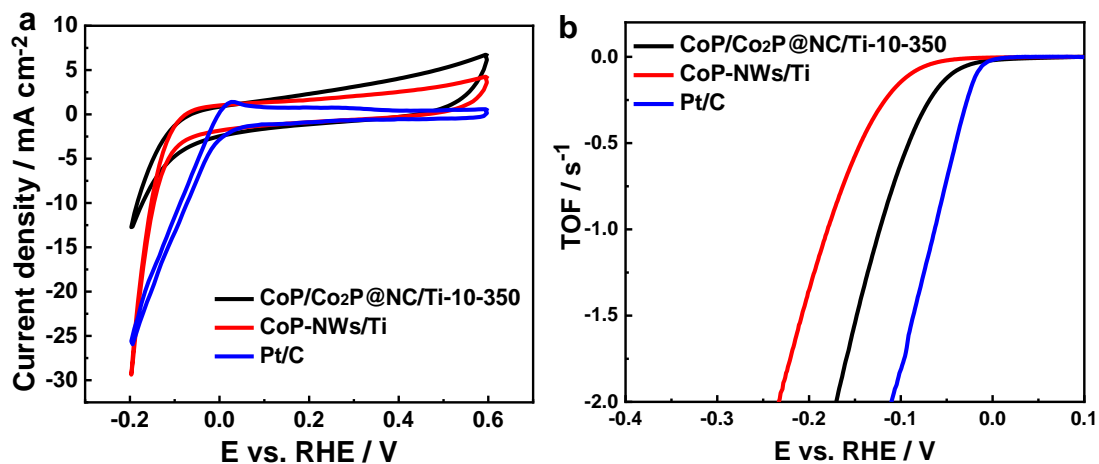


Figure S22. (a) CVs of CoP/Co₂P@NC/Ti-10-350, CoP-NWs/Ti and Pt/C electrodes in 1.0 M PBS (pH 7) with a scan rate of 50 mV s⁻¹, (b) Calculated TOFs for CoP/Co₂P@NC/Ti-10-350, CoP-NWs/Ti and Pt/C electrodes in 0.5 M H₂SO₄. Related to Figure 5.

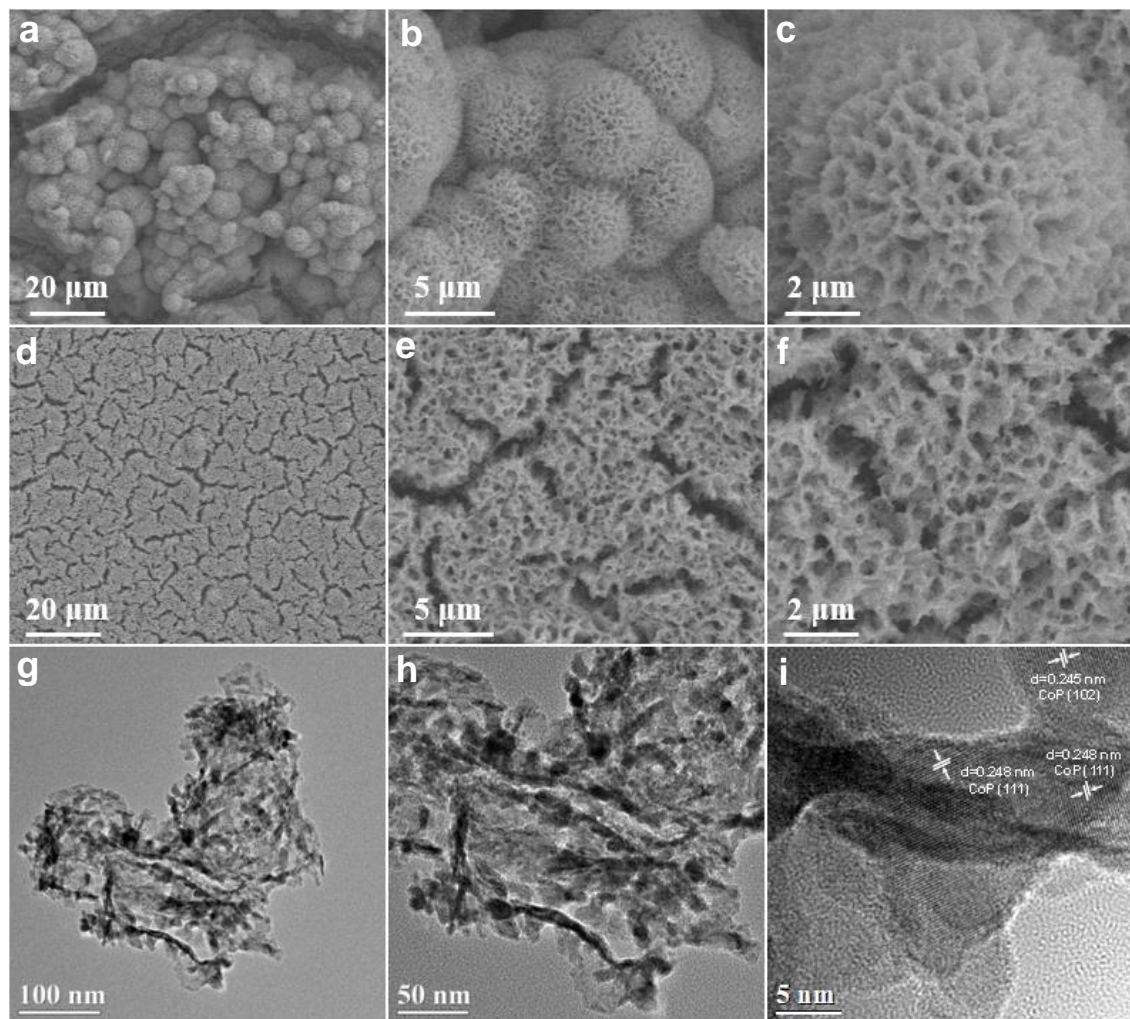


Figure S23. (a-c) SEM images of the used CoP/Co₂P@NC-10-350 honeycomb microspheres on Ti foil at different magnifications; (d-f) SEM images of the used CoP/Co₂P@NC-10-350 honeycomb layer on Ti foil at different magnifications; (g, h) TEM and (i) HRTEM images of the used CoP/Co₂P@NC-10-350 scratched down from Ti foil. Related to Figure 5.

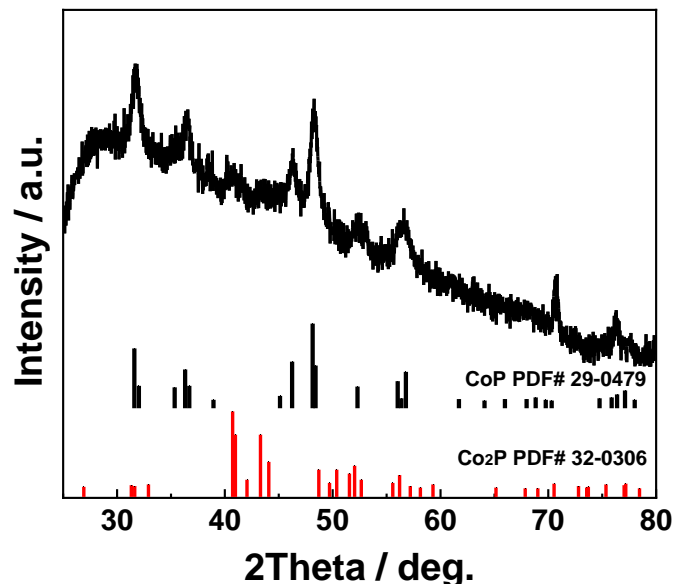


Figure S24. XRD pattern of the used CoP/Co₂P@NC-10-350 scratched down from Ti foil. Related to Figure 5.

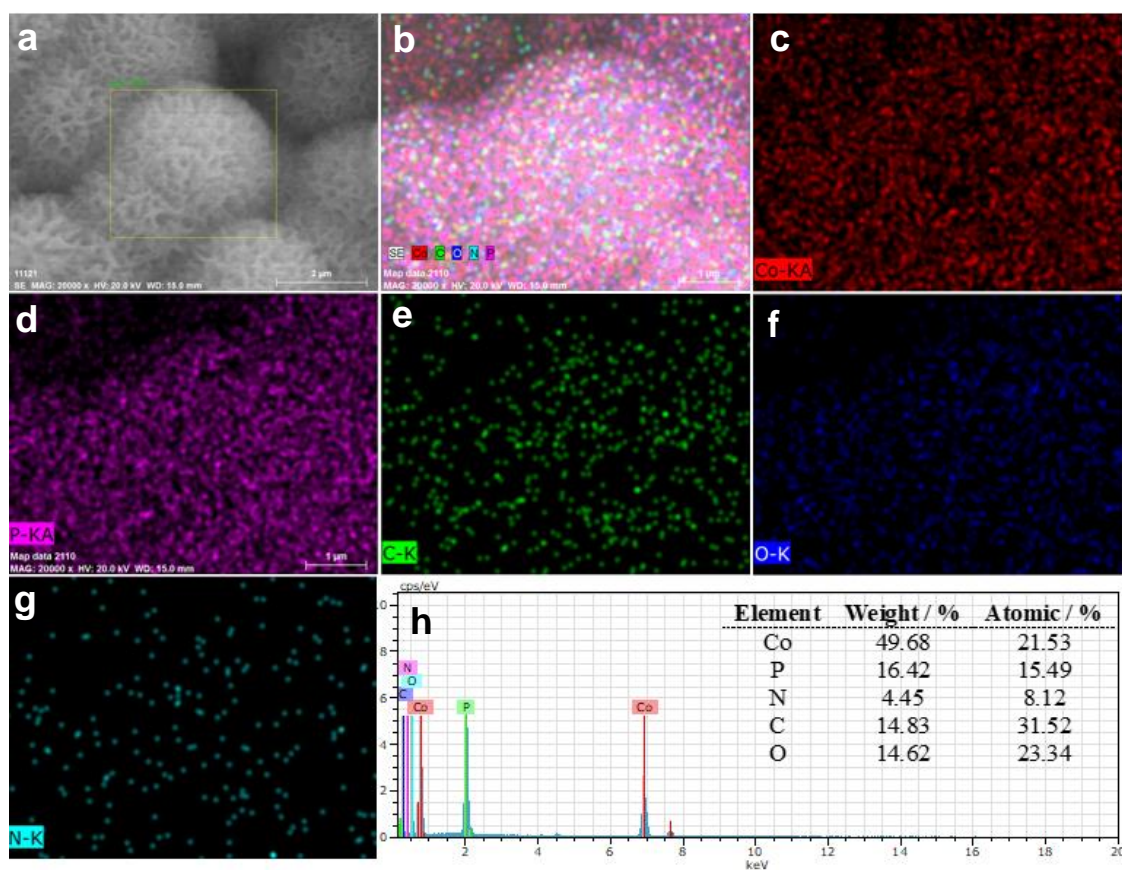


Figure S25. (a) SEM image of the used CoP/Co₂P@NC-10-350 honeycomb microspheres on Ti foil; (b-g) the EDX elemental mapping images of the used CoP/Co₂P@NC-10-350 honeycomb microspheres on Ti foil showing the element distributions of Co, P, C, N, and O; (g) EDX spectrum of the used CoP/Co₂P@NC-10-350 honeycomb microspheres on Ti foil. Related to Figure 5.

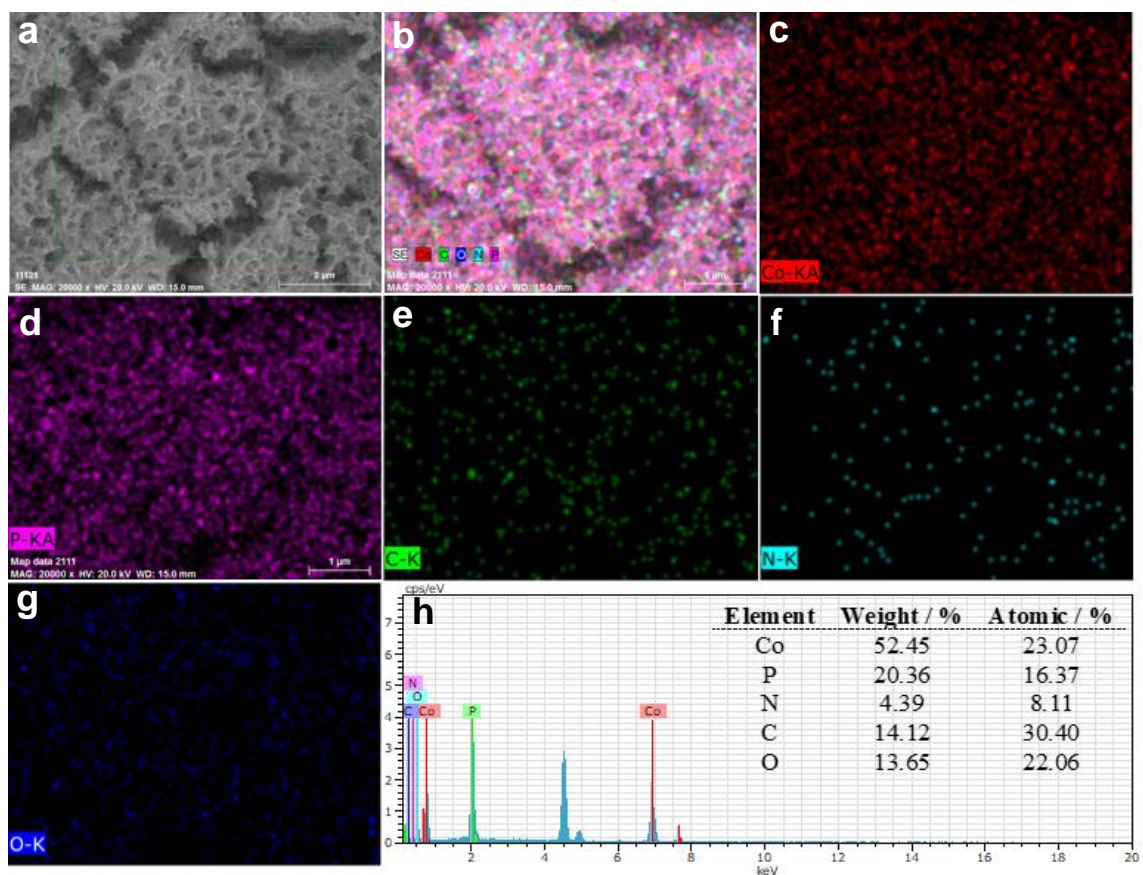


Figure S26. (a) SEM image of the used CoP/Co₂P@NC-10-350 honeycomb layer on Ti foil; (b-g) the EDX elemental mapping images of CoP/Co₂P@NC-10-350 honeycomb layer on Ti foil showing the element distributions of Co, P, C, N, and O; (h) EDX spectrum of CoP/Co₂P@NC-10-350 honeycomb layer on Ti foil. Related to Figure 5.

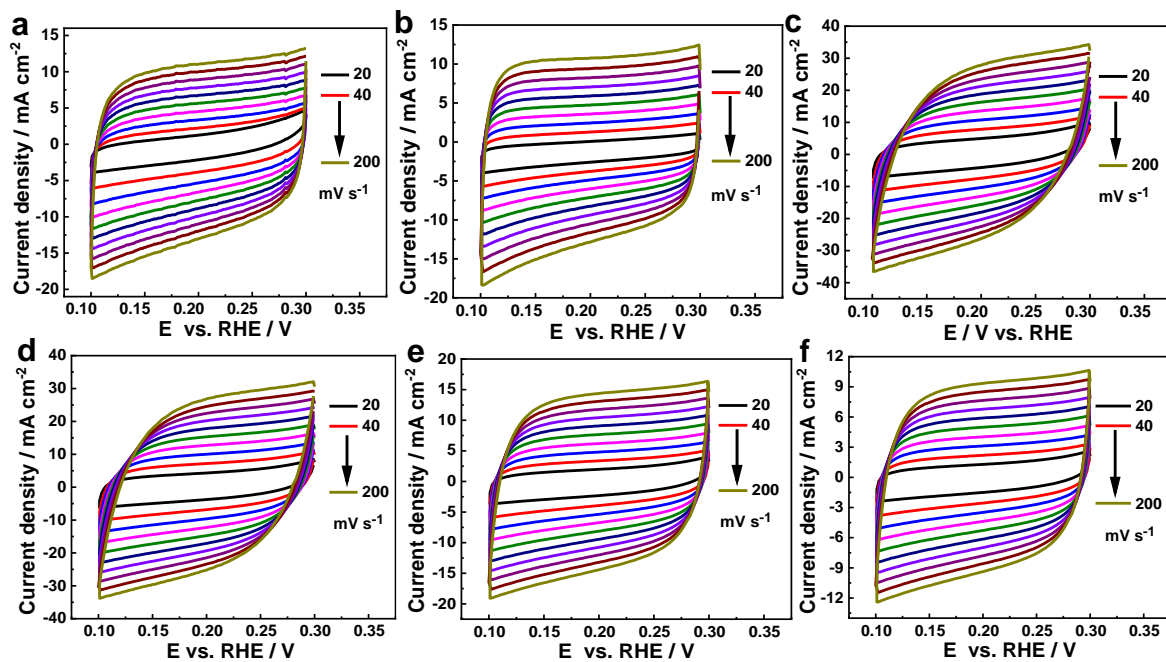


Figure S27. CVs performed at various scan rates in the region of 0.1 - 0.3 V vs. RHE in 0.5 M H₂SO₄ for (a) CoP NWs/Ti, (b) CoP/Co₂P@NC/Ti-0-350, (c) CoP/Co₂P@NC/Ti-30-350, (d) CoP/Co₂P@NC/Ti-50-350, (e) CoP/Co₂P@NC/Ti-70-350, (f) CoP/Co₂P@NC/Ti-90-350. Related to Figure 5.

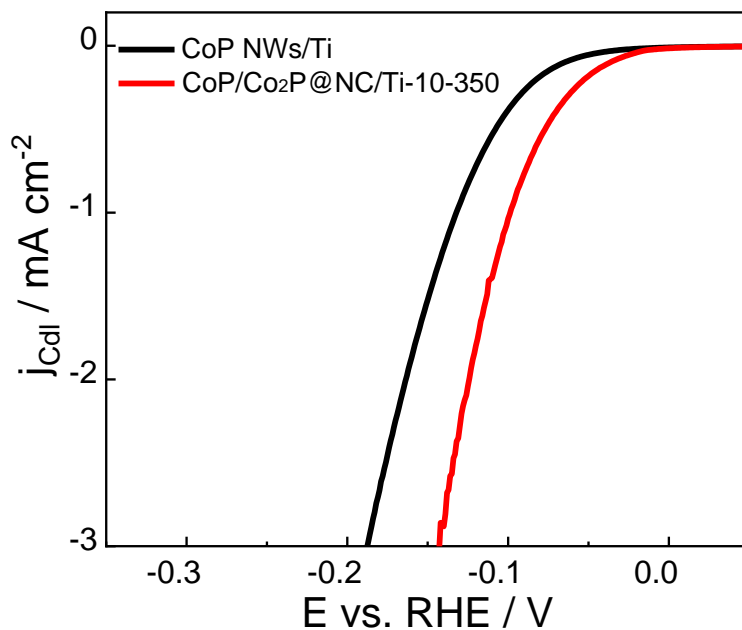


Figure S28. The C_{dl} normalized polarization curves for CoP-NWs/Ti and CoP/Co₂P@NC/Ti-10-350 in 0.5 m H₂SO₄ electrolyte at 2 mV s⁻¹. Related to Figure 5.

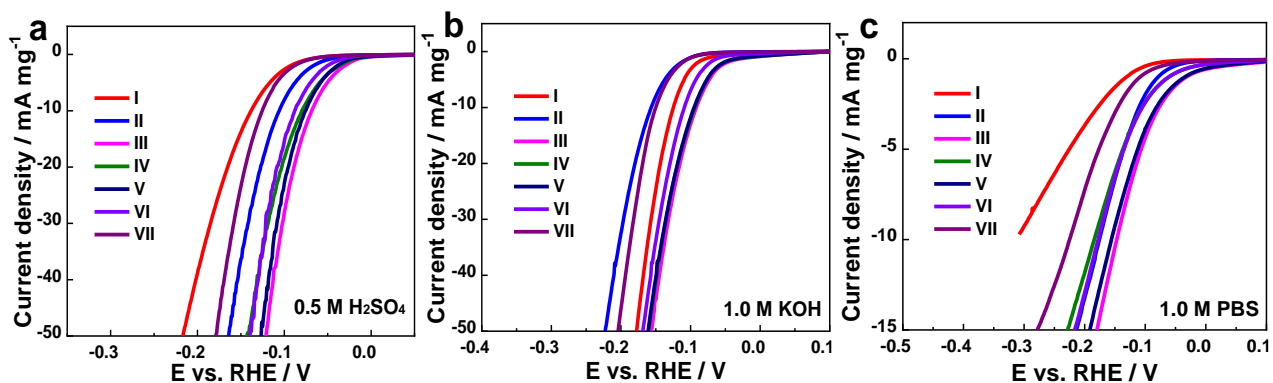


Figure S29. Mass-normalized HER activities of (I) CoP-NWs/Ti, (II) CoP/Co₂P@NC/Ti-0-350, (III) CoP/Co₂P@NC/Ti-10-350, (IV) CoP/Co₂P@NC/Ti-30-350, (V) CoP/Co₂P@NC/Ti-50-350, (VI) CoP/Co₂P@NC/Ti-70-350, (VII) CoP/Co₂P@NC/Ti-90-350 in (a) 0.5 M H₂SO₄, (b) 1.0 M KOH, and (c) 1.0 M PBS solutions. Related to Figures 5 and 6.

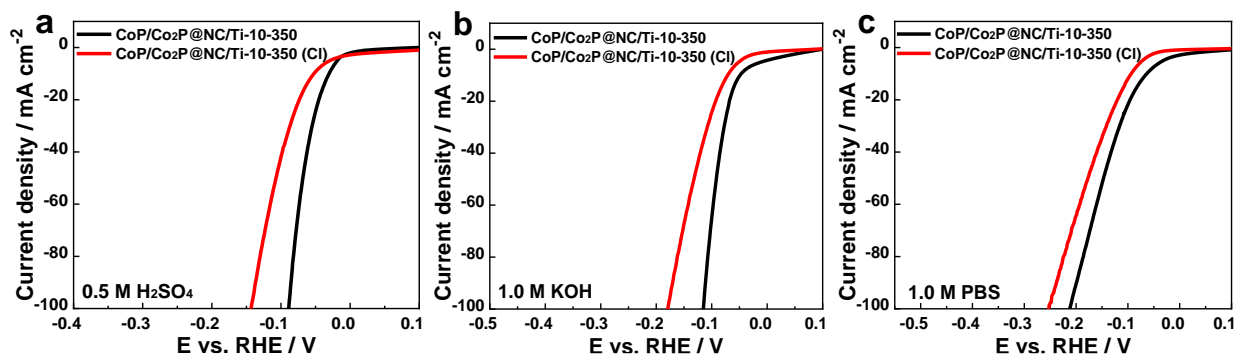


Figure S30. LSV curves of CoP/Co₂P@NC/Ti-10-350 and CoP/Co₂P@NC/Ti-10-350 (Cl) in (a) 0.5 M H₂SO₄, (b) 1.0 M KOH, and (c) 1.0 M PBS solutions. Related to Figures 5 and 6.

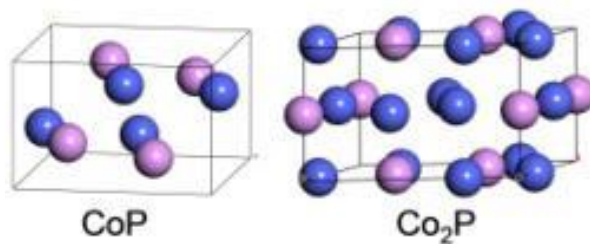


Figure S31. The unit cells of CoP and Co₂P, the Co and P atoms are in blue and pink, respectively. Related to Figure 7.

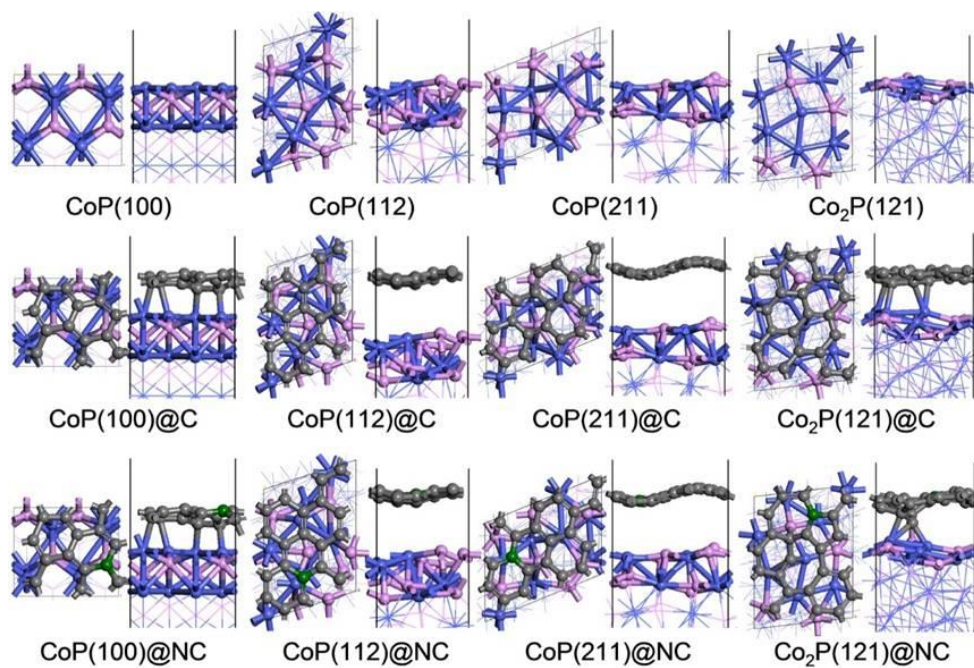


Figure S32. Top and side view structures of the clean, carbon (@C) and N-carbon (@NC) shell catalyst surfaces of CoP and Co₂P. In the surface models, Co, P, C, and N atoms are given in blue, pink, gray and green, respectively. Related to Figure 7.

Table S1. Comparison of the HER performance of different electrocatalysts. Related to Figures 5 and 6.

Electrocatalyst	Electrolytes	$\eta_{10}^a)$ [mV]	η_{20} [mV]	η_{100} [mV]	$b^b)$ [mV dec ⁻¹]
CoP/Co ₂ P@NC/Ti-10-350	0.5 M H ₂ SO ₄	31	46	89	44
	1.0 M KOH	49	68	116	51
	1.0 M PBS	64	96	213	98
CoP-NWs/Ti	0.5 M H ₂ SO ₄	106	129	220	55
	1.0 M KOH	91	117	239	58
	1.0 M PBS	225	308	–	106
Pt/C	0.5 M H ₂ SO ₄	26	41	115	28
	1.0 M KOH	30	55	–	45
	1.0 M PBS	58	134	–	70
CoP/Co ₂ P@NC/Ti-0-350	0.5 M H ₂ SO ₄	72	88	133	53
	1.0 M KOH	114	132	181	53
	1.0 M PBS	101	126	258	102
CoP/Co ₂ P@NC/Ti-30-350	0.5 M H ₂ SO ₄	33	49	96	46
	1.0 M KOH	54	72	119	53
	1.0 M PBS	92	126	283	103
CoP/Co ₂ P@NC/Ti-50-350	0.5 M H ₂ SO ₄	37	50	93	45
	1.0 M KOH	53	72	119	52
	1.0 M PBS	68	102	227	108
CoP/Co ₂ P@NC/Ti-70-350	0.5 M H ₂ SO ₄	47	61	103	50
	1.0 M KOH	73	88	130	55
	1.0 M PBS	92	124	261	101
CoP/Co ₂ P@NC/Ti-90-350	0.5 M H ₂ SO ₄	97	112	152	50
	1.0 M KOH	113	128	169	51
	1.0 M PBS	134	165	–	92
CoP/Co ₂ P@NC/Ti-10-300	0.5 M H ₂ SO ₄	46	66	140	52
CoP/Co ₂ P@NC/Ti-10-400	0.5 M H ₂ SO ₄	56	77	168	54
CoP@NC/Ti-10-500	0.5 M H ₂ SO ₄	123	145	235	56

^{a)} η : overpotential required to achieve the stated current density; ^{b)} b : Tafel slope.

Table S2. Comparison of the electrocatalytic activity of CoP/Co₂P@NC/Ti-10-350 electrode reported in this work and some other representative phosphide-based HER electrocatalysts that have been recently reported in acidic medium. Related to Figure 5.

Electrocatalyst	Electrolyte	Loading [mg cm ⁻²]	η_{10} [mV]	Tafel slope [mV dec ⁻¹]	Ref.
CoP/Co ₂ P@NC/Ti-10-350	0.5 M H ₂ SO ₄	5	31	44	This work
CoP/NCNHP	0.5 M H ₂ SO ₄	2	140	53	<i>J. Am. Chem. Soc.</i> 2018, 140, 2610.
CoP NFs	0.5 M H ₂ SO ₄	0.265	122	54.8	<i>ACS Catal.</i> 2020, 10, 412.
np-Co ₂ P	0.5 M H ₂ SO ₄	—	80	44	<i>Adv. Mater.</i> 2016, 28, 2951.
CoP@PC-750	0.5 M H ₂ SO ₄	1.0	49	72	<i>Small</i> 2019, 15, 1900550.
CoP-InNC@CNT	0.5 M H ₂ SO ₄	0.35	153	62	<i>Adv. Sci.</i> 2020, 7, 1903195.
CoP/NPC/TF	0.5 M H ₂ SO ₄	~1.5	91	54	<i>Adv. Energy Mater.</i> 2019, 9, 1803970.
CoP@NC-NG	0.5 M H ₂ SO ₄	0.28	135	59.3	<i>Small</i> 2018, 14, 1702895.
CoP-400	0.5 M H ₂ SO ₄	0.43	113	67	<i>Small</i> 2018, 14, 1802824.
CoP/Co ₂ P	0.5 M H ₂ SO ₄	~0.36	99	51.4	<i>Nanoscale</i> 2018, 10, 21019.
CoP@NC	0.5 M H ₂ SO ₄	0.306	78	49	<i>ACS Catal.</i> 2017, 7, 3824.
Co ₂ P-C	0.5 M H ₂ SO ₄	0.382	96	68	<i>J. Am. Chem. Soc.</i> 2017, 139, 11248.
CoP/CC	0.5 M H ₂ SO ₄	0.92	67	51	<i>J. Am. Chem. Soc.</i> 2014, 136, 7587.
CoP/Ti	0.5 M H ₂ SO ₄	2.0	75	50	<i>Angew. Chem. Int. Ed.</i> 2014, 53, 5427.
Ni _{0.67} Co _{1.33} P/N-C NFs	0.5 M H ₂ SO ₄	—	100	35	<i>Appl. Catal. B Environ.</i> 2019, 244, 620.
CoP/NiCoP	0.5 M H ₂ SO ₄	2	125	71	<i>Adv. Energy Mater.</i> 2019, 9, 1901213.
2D CoP/NiCoP/NC	0.5 M H ₂ SO ₄	0.318	60	58	<i>Adv. Funct. Mater.</i> 2019, 29, 1807976.
W-CoP NAs/CC	0.5 M H ₂ SO ₄	2.6	89	58	<i>Small</i> 2019, 15, 1902613.
Mn-Co-P/Ti	0.5 M H ₂ SO ₄	5.61	49	51	<i>ACS Catal.</i> 2017, 7, 98.
Co-Co ₂ P@NPC/rGO	0.5 M H ₂ SO ₄	0.357	61.5	50.64	<i>Adv. Funct. Mater.</i> 2018, 28, 1801332.
FeP HNSs	0.5 M H ₂ SO ₄	1.6	51.1	41.7	<i>Adv. Sci.</i> 2019, 6, 1801490.
FeP@PC	0.5 M H ₂ SO ₄	0.243	52	49	<i>Adv. Funct. Mater.</i> 2015, 25, 3899.
Co-Fe-P nanotubes	0.5 M H ₂ SO ₄	0.285	66	72	<i>Nano Energy</i> 2019, 56, 225.
Ni ₂ P@NPCNFs	0.5 M H ₂ SO ₄	0.337	63	56.7	<i>Angew. Chem. Int. Ed.</i> 2018, 57, 1963.
Ni-FeP/C	0.5 M H ₂ SO ₄	0.4	72	54	<i>Sci. Adv.</i> 2019, 5, eaav6009.
Ni ₁₂ P ₅ nanoparticles	0.5 M H ₂ SO ₄	3.0	107	63	<i>ACS Nano.</i> 2014, 8, 8121.
CP@Ni-P	0.5 M H ₂ SO ₄	—	98	59	<i>Adv. Funct. Mater.</i> 2016, 26, 4067.
Cu ₃ P@NPPC	0.5 M H ₂ SO ₄	0.29	89	76	<i>Adv. Mater.</i> 2018, 30, 1703711.
3D MoP/NPG	0.5 M H ₂ SO ₄	0.28	148	49	<i>Appl. Catal. B Environ.</i> 2020, 260, 118196.
MoP@C	0.5 M H ₂ SO ₄	6	49	54	<i>Adv. Energy Mater.</i> 2018, 8, 1801258.

MoP/CNTs-700	0.5 M H ₂ SO ₄	0.5	83	60	<i>Adv. Funct. Mater.</i> 2018, 28, 1706523.
MoP NWAs/CFP	0.5 M H ₂ SO ₄	2.8	56	49	<i>Adv. Funct. Mater.</i> 2018, 28, 1804600.
S-CoWP@(S,N)-C	0.5 M H ₂ SO ₄	0.75	35	35	<i>ACS Energy Lett.</i> 2018, 3, 1434.
Mo–W–P nanosheet	0.5 M H ₂ SO ₄	4.0	90	52	<i>Energy Environ. Sci.</i> 2016, 9, 1468.

Table S3. Comparison of the R_s and R_{ct} of different electrocatalysts in this work at the applied potential of -65 mV in 0.5 M H_2SO_4 . Related to Figure 5.

Electrocatalyst	Electrolyte	R_s [Ω]	R_{ct} [Ω]
CoP/Co ₂ P@NC-10-350	0.5 M H ₂ SO ₄	1.75	4.35
CoP-NWs/Ti	0.5 M H ₂ SO ₄	2.94	25.3
CoP/Co ₂ P@NC-0-350	0.5 M H ₂ SO ₄	2.05	19.29
CoP/Co ₂ P@NC-30-350	0.5 M H ₂ SO ₄	1.74	4.74
CoP/Co ₂ P@NC-50-350	0.5 M H ₂ SO ₄	1.77	4.39
CoP/Co ₂ P@NC-70-350	0.5 M H ₂ SO ₄	2.21	6.25
CoP/Co ₂ P@NC-90-350	0.5 M H ₂ SO ₄	2.67	25.07

Table S4. Comparison of the electrocatalytic activity of CoP/Co₂P@NC/Ti-10-350 electrode reported in this work and some other representative phosphide-based HER electrocatalysts that have been recently reported in alkaline medium. Related to Figure 6.

Electrocatalyst	Electrolyte	Loading [mg cm ⁻²]	η_{10} [mV]	Tafel slope [mV dec ⁻¹]	Ref.
CoP/Co ₂ P@NC/Ti-10-350	1.0 M KOH	5	49	51	This work
CoP/NCNHP	1.0 M KOH	2	115	66	<i>J. Am. Chem. Soc.</i> 2018, 140, 2610.
CoP NFs	1.0 M KOH	0.265	136	56.2	<i>ACS Catal.</i> 2020, 10, 412.
np-Co ₂ P	1.0 M KOH	—	60	40	<i>Adv. Mater.</i> 2016, 28, 2951.
CoP@PC-750	1.0 M KOH	1.0	52	76	<i>Small</i> 2019, 15, 1900550.
CoP-InNC@CNT	1.0 M KOH	0.35	159	56	<i>Adv. Sci.</i> 2020, 7, 1903195.
CoP/NPC/TF	1.0 M KOH	~1.5	80	50	<i>Adv. Energy Mater.</i> 2019, 9, 1803970.
CoP@NC-NG	1.0 M KOH	0.28	155	68.6	<i>Small</i> 2018, 14, 1702895.
CoP-400	1.0 M KOH	0.43	154	72	<i>Small</i> 2018, 14, 1802824.
CoP@NC	1.0 M KOH	0.306	129	58	<i>Nanoscale</i> 2018, 10, 21019.
CoP-A	1.0 M KOH	0.4	100	76	<i>Chem. Sci.</i> 2019, 10, 2019.
CoP NWs/CC	1.0 M KOH	—	65	42.8	<i>Adv. Mater.</i> 2018, 30, 1703322.
CoP NCs	1.0 M KOH	0.2	62.5	69.2	<i>Adv. Mater.</i> 2018, 30, 1705796.
Co ₂ P@C	1.0 M KOH	3.2	70	59.7	<i>ACS Energy Lett.</i> 2018, 3, 1360.
CoP ₂ /RGO	1.0 M KOH	0.285	88	50	<i>J. Mater. Chem. A</i> 2016, 4, 4686.
u-CoP/Ti	1.0 M KOH	6.32	60	49	<i>J. Mater. Chem. A</i> 2016, 4, 10114.
Co-P/Cu	1.0 M KOH	~2.6	94	42	<i>Angew. Chem. Int. Ed.</i> 2015, 54, 6251.
Ni _{0.67} Co _{1.33} P/N-C NFs	1.0 M KOH	—	130	70	<i>Appl. Catal. B Environ.</i> 2019, 244, 620.
CoP/NiCoP	1.0 M KOH	2	133	88	<i>Adv. Energy Mater.</i> 2019, 9, 1901213.
2D CoP/NiCoP/NC	1.0 M KOH	0.318	75	64	<i>Adv. Funct. Mater.</i> 2019, 29, 1807976.
W-CoP NAs/CC	1.0 M KOH	2.6	94	63	<i>Small</i> 2019, 15, 1902613.
Mn-Co-P/Ti	1.0 M KOH	5.61	76	52	<i>ACS Catal.</i> 2017, 7, 98.
N-NiCoP/NCF	1.0 M KOH	2.085	78	83.2	<i>Appl. Catal. B Environ.</i> 2019, 254, 414.
Co _{0.93} Ni _{0.07} P ₃ /CC	1.0 M KOH	1.05	97	60.7	<i>ACS Energy Lett.</i> 2018, 3, 1744.
Co-Fe-P nanotubes	1.0 M KOH	0.285	86	66	<i>Nano Energy</i> 2019, 56, 225.
Fe-CoP/Ti	1.0 M KOH	1.01	78	75	<i>Adv. Mater.</i> 2017, 29, 1602441.
Fe _{0.29} Co _{0.71} P/Ni	1.0 M KOH	—	74	53.56	<i>Nano Energy</i> 2020, 67, 104174.
Co _{0.6} Fe _{0.4} P	1.0 M KOH	0.27	133	61	<i>Chem. Sci.</i> 2019, 10, 464.
CF@FeCoP/NC	1.0 M KOH	0.4	89	75	<i>Nano Energy</i> 2019, 56, 82.
Ni ₂ P@NPCNFs	1.0 M KOH	0.337	104.2	79.7	<i>Angew. Chem. Int. Ed.</i> 2018, 57, 1963.
Ni-FeP/C	1.0 M KOH	0.4	95	72	<i>Sci. Adv.</i> 2019, 5, eaav6009.
Ni ₂ P/Ni/NF	1.0 M KOH	—	98	72	<i>ACS Catal.</i> 2016, 6, 714.
Ni _{1.8} Cu _{0.2} -P/NF	1.0 M KOH	2	78	70	<i>Appl. Catal. B Environ.</i> 2019, 243, 537.
CoMoP@C	1.0 M KOH	0.354	81	55.53	<i>Energy Environ. Sci.</i> 2017, 10, 788.
Ni _{2(1-x)} Mo _{2x} P/NF	1.0 M KOH	7.4	72	46.4	<i>Nano Energy</i> 2018, 53, 492.
3D MoP/NPG	1.0 M KOH	0.28	126	56	<i>Appl. Catal. B Environ.</i> 2020, 260, 118196.

MoP@C	1.0 M KOH	6	49	54	<i>Adv. Energy Mater.</i> 2018, 8, 1801258.
MoP/CNTs-700	1.0 M KOH	0.5	86	73	<i>Adv. Funct. Mater.</i> 2018, 28, 1706523.
MoP NWAs/CFP	1.0 M KOH	2.8	52	40	<i>Adv. Funct. Mater.</i> 2018, 28, 1804600.
S-CoWP@(S, N)-C	1.0 M KOH	0.75	67	61	<i>ACS Energy Lett.</i> 2018, 3, 1434.
MoP@NCHSs-900	1.0 M KOH	0.4	92	62	<i>Angew. Chem. Int. Ed.</i> 2020, 59, 4154.

Table S5. Comparison of the electrocatalytic activity of CoP/Co₂P@NC/Ti-10-350 electrode reported in this work and some other representative phosphide-based HER electrocatalysts recently reported in neutral medium. Related to Figure 6.

Electrocatalyst	Electrolyte	Loading [mg cm ⁻²]	η_{10} [mV]	Tafelslope [mV dec ⁻¹]	Ref.
CoP/Co ₂ P@NC/Ti-10-350	1.0 M PBS	5	64	98	This work
CoP@NC-NG	1.0 M PBS	0.28	178	99.5	<i>Small</i> 2018, 14, 1702895.
CoP-400	1.0 M PBS	0.43	161	81	<i>Small</i> 2018, 14, 1802824.
CoP/CC	1.0 M PBS	0.92	106	93	<i>J. Am. Chem. Soc.</i> 2014, 136, 7587.
CoP@BCN	1.0 M PBS	0.0204	122	59	<i>Adv. Energy Mater.</i> 2017, 7, 1601671.
CoPNW/Hb	1.0 M PBS	4.11	121	113	<i>Nano Res.</i> 2017, 10, 1010.
CoP/Ti	1.0 M PBS	2.0	149	58	<i>Chem. Mater.</i> 2014, 26, 4326.
np-CoP NWs/Ti	1.0 M PBS	0.8	100	71	<i>Phys. Chem. Chem. Phys.</i> 2014, 16, 16909.
N-CoP/CC	1.0 M PBS	—	74	69	<i>Appl. Catal. B Environ.</i> 2019, 253, 21.
W-CoP NAs/CC	1.0 M PBS	2.6	102	87	<i>Small</i> 2019, 15, 1902613.
V-CoP/CC	1.0 M PBS	3.18	123	72.6	<i>Chem. Sci.</i> 2018, 9, 1970.
Ni _{0.1} Co _{0.9} P-CFP	1.0 M PBS	0.58	103	125	<i>Angew. Chem. Int. Ed.</i> 2018, 57, 15445.
Ni _{0.67} Co _{1.33} P/N-C NFs	1.0 M PBS	—	110	69	<i>Appl. Catal. B Environ.</i> 2019, 244, 620.
2D CoP/NiCoP/NC	1.0 M PBS	0.318	123	78	<i>Adv. Funct. Mater.</i> 2019, 29, 1807976.
NiCoP/rGO	1.0 M PBS	0.15	124	91	<i>Adv. Funct. Mater.</i> 2016, 26, 6785.
CoNiP/NF	1.0 M PBS	1.0	120	103	<i>J. Mater. Chem. A</i> 2016, 4, 10195.
Mn-Co-P/Ti	1.0 M PBS	5.61	86	82	<i>ACS Catal.</i> 2017, 7, 98.
Co-Fe-P nanotubes	1.0 M PBS	0.285	138	138	<i>Nano Energy</i> 2019, 56, 225.
Ni ₂ P@NPCNFs	1.0 M PBS	0.337	185	230	<i>Angew. Chem. Int. Ed.</i> 2018, 57, 1963.
Ni-FeP/C	1.0 M PBS	0.4	117	70	<i>ACS Nano.</i> 2014, 8, 8121.
FeP NPs@NPC	1.0 M PBS	1.4	386	136	<i>Nanoscale</i> 2017, 9, 3555.
3D MoP/NPG	1.0 M PBS	0.28	150	102	<i>Appl. Catal. B Environ.</i> 2020, 260, 118196.
MoP/CNTs-700	1.0 M PBS	0.5	102	115	<i>Adv. Funct. Mater.</i> 2018, 28, 1706523.
MoP NWAs/CFP	1.0 M PBS	2.8	84	63	<i>Adv. Funct. Mater.</i> 2018, 28, 1804600.
S-MoP NPL	1.0 M PBS	—	142	98	<i>ACS Catal.</i> 2019, 9, 651.
MoP700	1.0 M PBS	0.25	196	79	<i>ACS Catal.</i> 2019, 9, 8712.

2. Transparent Methods

Chemicals

Cobalt nitrate hexahydrate [$\text{Co}(\text{NO}_3)_2 \cdot 6\text{H}_2\text{O}$, AR], monohydrate sodium hypophosphite ($\text{NaH}_2\text{PO}_2 \cdot \text{H}_2\text{O}$, AR), triethanolamine (AR), urea [$\text{CO}(\text{NH}_2)_2$, AR], ammonium fluoride (NH_4F , AR) and sulfuric acid (H_2SO_4 , AR) were purchased from Sinopharm chemical reagent Co., Ltd. Potassium hydroxide (KOH, 99.9%) was received from Aladdin. Platinum, nominally 20 wt% on carbon black, HiSPECTM 3000 (Pt/C), Iridium (IV) oxide (99.99%) and Titanium foil (0.032 mm, metals basis, 99.7%) were obtained from Alfa Aesar (China). All reagents were used as received without further purification. The water used throughout all experiments was purified through a Millipore system.

Materials Characterization

XRD was performed on a PANalytical Empyrean diffractometer with $\text{Cu K}\alpha_1$ radiation ($\lambda = 1.5405 \text{ \AA}$) operated at a scanning rate of 0.013° in the Bragg angle ranging between 5° and 80° . Transmission electron microscopy (TEM) and scanning transmission electron microscopy (STEM) characterizations were performed on a FEI Tecnai F20 field-emission transmission electron microscope (FE-TEM). Scanning electron micrographs were recorded with a Hitachi S-4800 field emission scanning electron microscope (FE-SEM). X-ray photoelectron spectroscopy (XPS) measurements were performed in a VG Scientific ESCALAB Mark II spectrometer equipped with two ultrahigh vacuum (UHV) chambers. All spectra were calibrated with the C-C peak of C 1s orbitals as 284.8 eV. Surface area measurements were performed on an ASAP 2020 Brunauer-Emmett-Teller (BET) analyzer. Raman spectroscopy characterizations were carried out using a Renishaw in via Raman microscope with a 532 nm laser source under vacuum conditions in an in-situ reaction cell. Thermogravimetric analysis (TGA) was carried out using a Rigaku TG-8120 instrument in the temperature range 25-800°C at a heating rate of $5^\circ\text{C} \cdot \text{min}^{-1}$ under a nitrogen flow. UV-vis diffuse reflectance spectrum was recorded at room temperature in air on a Shimadzu UV-2450 spectrophotometer.

Preparation of Large-Scale Lamellar Nitride-Hydroxide Cobalt Precursor of $\text{Co}(\text{OH})_x(\text{NO}_3)_{2-x} \cdot \text{mH}_2\text{O}$ on Inch-Sized Ti Foil

Large-scale $\text{Co}(\text{OH})_x(\text{NO}_3)_{2-x} \cdot \text{mH}_2\text{O}/\text{Ti}$ precursor was synthesized *via* low-temperature solution method as follows: typically, 21.825 g of $\text{Co}(\text{NO}_3)_2 \cdot 6\text{H}_2\text{O}$ was dissolved in a 700 mL of mixed solution of triethanolamine (600 mL) and water (100 mL). The mixed solution was then transferred into a beaker (1000 mL) and a piece of cleaned Ti plate (4 inch \times 4 inch) pre-treated using 2.0 M hydrochloric acid, water, and acetone for 15 min, respectively, was immersed into the mixed solution. Subsequently, the beaker with sealing film was heated to 80 °C for 12 h in an oil bath. After being naturally cooled down, the $\text{Co}(\text{OH})_x(\text{NO}_3)_{2-x} \cdot \text{mH}_2\text{O}/\text{Ti}$ precursor was taken out and washed with distilled water and ethanol several times before being dried at 80 °C for 6 h.

Preparation of $\text{CoP}/\text{Co}_2\text{P}@/\text{NC}/\text{Ti}$ Electrode

To obtain $\text{CoP}/\text{Co}_2\text{P}@/\text{NC}/\text{Ti}$ electrode, the $\text{Co}(\text{OH})_x(\text{NO}_3)_{2-x} \cdot \text{mH}_2\text{O}/\text{Ti}$, which is truncated to small pieces (3 cm \times 1.5 cm) to facilitate phosphidation, and NaH_2PO_2 were put at two separate positions in a tube furnace with 0.3 g of NaH_2PO_2 at the upstream side of the furnace. After flushing with N_2 for 30 min, the furnace was elevated to 350° with a heating speed of $2^\circ\text{C} \cdot \text{min}^{-1}$ and held at this temperature for 120 min in a flowing N_2 atmosphere. The $\text{CoP}/\text{Co}_2\text{P}@/\text{NC}/\text{Ti}$ electrode was obtained after being naturally cooled to ambient temperature under N_2 atmosphere. The loading for $\text{CoP}/\text{Co}_2\text{P}@/\text{NC}$ on Ti was determined to be $\sim 5 \text{ mg}/\text{cm}^2$ with the use of a high precision microbalance.

Preparation of $\text{Co}(\text{OH})\text{F-NWs}/\text{Ti}$ Precursor and $\text{CoP-NWs}/\text{Ti}$ Electrode

$\text{Co}(\text{OH})\text{F-NWs}/\text{Ti}$ was prepared via a hydrothermal method. In a typical synthesis, $\text{Co}(\text{NO}_3)_2 \cdot 6\text{H}_2\text{O}$ (0.291 g), NH_4F (0.093 g) and urea (0.30 g) were dissolved in 20 mL of water under vigorous stirring for 30 min. Then the solution was transferred into a Teflon-lined stainless autoclave (25 mL) and a piece of Ti foil (3 cm \times 1.5 cm), which was cleaned by sonication sequentially in acetone, water, and ethanol for 10 min each, was immersed into the solution. The autoclave was sealed and maintained at 120 °C for 6 h in an oven. Then the autoclave cooled down slowly at room temperature, the $\text{Co}(\text{OH})\text{F-NWs}/\text{Ti}$ was taken out and washed with water thoroughly before drying at 60 °C for 12 h. To prepare $\text{CoP-NWs}/\text{Ti}$ electrode, $\text{Co}(\text{OH})\text{F-NWs}/\text{Ti}$ and NaH_2PO_2 were put at two separate positions in a porcelain boat with NaH_2PO_2 at the upstream side of the furnace. The molar ratio for Co to P is 1:5. Subsequently, the samples were heated at 350 °C for 120 min in a static N_2 atmosphere, and then naturally cooled to ambient temperature under a flowing N_2 atmosphere.

Electrochemical Measurements

Electrochemical measurements were carried out on an electrochemical workstation (Zahner Zennium, Germany) in a standard three electrode system with a carbon rod electrode as the counter electrode, CoP/Co₂P@NC/Ti as the working electrode, and a saturated calomel electrode (SCE, 0.241 V vs RHE) as the reference electrode. All potentials were referenced to a reversible hydrogen electrode (RHE). Linear sweep voltammetry (LSV) polarization curves were acquired in H₂ saturated 0.5 M H₂SO₄, 1.0 M PBS, and 1.0 M KOH electrolytes with a sweep rate of 2 mV s⁻¹ in the range of +0.1 to -0.4 V. vs RHE. The Tafel plots are fitted from the corresponding linear sweep voltammetry (LSV) curves with internal resistance (iR) corrected according to the Tafel equation $\eta = a + b \log|j|$, where b is the Tafel slope and j₀ represents the exchange current density. The accelerated durability tests (ADTs) were conducted by performing up to 3000 CV cycles in 0.5 M H₂SO₄, 1.0 M PBS, and 1.0 M KOH electrolytes with a sweep rate of 100 mV s⁻¹ in the range of +0.1 to -0.25 V. vs RHE. The amperometric i-t curves were measured for 20 h in 0.5 M H₂SO₄, 1.0 M PBS, and 1.0 M KOH electrolytes under controlled potentials. Electrochemical impedance spectroscopy (EIS) measurements were carried out from 100000 to 0.1 Hz in 0.5 M H₂SO₄ and 1.0 M KOH solutions, respectively at different overpotentials. All currents in our work are corrected against the ohmic potential drop. All the potentials reported in our work were vs. RHE. In 0.5 M H₂SO₄, E (RHE) = E (SCE) + 0.281 V; In 1.0 M PBS, E (RHE) = E (SCE) + 0.655 V; In 1.0 M KOH, E (RHE) = E (SCE) + 1.068 V.

The Detail Calculation Process of TOF for HER

First, the CV measurements of CoP/Co₂P@NC/Ti-350, CoP-NWs/Ti and Pt/C electrodes were carried out in PBS electrolyte (pH 7). Then, the absolute components of the voltammetric charges (cathodic and anodic) reported during one single blank measurement was added. Assuming one electron redox process, this absolute charge was divided by two. The value was then divided by the Faraday constant to get the number of active sites (n) of the CoP/Co₂P@NC/Ti-350, CoP-NWs/Ti and Pt/C electrodes. The turnover frequency (s⁻¹) was calculated following equation: TOF = I/2nF where, I is Current (A) during the LSV measurement in 0.5 M H₂SO₄ solution, F is the Faraday constant (C/mol) and n is the number of active sites (mol). The factor 1/2 arrives by taking into account that two electrons are required to form one hydrogen molecule from two protons.

Theoretical Calculations

Computational Methods

All DFT calculations used the Vienna Ab Initio Simulation Package (VASP) (Kresse and Furthmüller, 1996; Kresse and Furthmüller, 1996). The electron-ion interaction was described using the Projector Augmented Wave (PAW) method (Kresse and Joubert, 1999; Blöchl, 1994). The electron exchange and correlation energies were treated within the generalized gradient approximation in the Perdew-Burke-Ernzerh of formalism (GGA-PBE) (Perdew et al., 1996). The plane wave basis was set up to 450 eV, and MP k-point sampling was used. Electron smearing was used *via* the Methfessel-Paxton technique, with a smearing width consistent to $\sigma = 0.2$ eV. Meanwhile, the spin polarization was included. The free energies were evaluated by $\Delta G(H^*) = \Delta E(H^*) + \Delta ZPE - T\Delta S$, where $\Delta E(H^*)$, ΔZPE and ΔS are the binding energy, zero-point energy change and entropy change of H* adsorption, respectively. In view of the ΔZPE and ΔS are very small for such packaged systems, so $\Delta ZPE \approx -1/2 ZPE(H_2)$ and $\Delta S \approx -1/2 S(H_2)$, and they are 0.27 and 0.40 eV in our work, which are similar with reference values (Yang et al., 2017).

Models

The calculated lattice constants of the CoP unit cell were a = 5.063 Å, b = 3.266 Å, c = 5.538 Å and $\alpha = \beta = \gamma = 90.00^\circ$, the Co₂P unit cell were a = b = 5.718 Å, c = 3.401 Å and $\gamma = 90.00^\circ$. The Co (HCP) unit cell dimensions were a = b = 2.493 Å, c = 4.026 Å and $\gamma = 120.00^\circ$. These two cells are shown in the Figure S36. Top and side view structures of CoP(100), (112), (211) and Co₂P(121) surfaces as well as their carbon (@C) and N-carbon (@NC) shell models are shown in Figure 7a, the unit cell p(1 × 1) is used for all these models. 5 × 5 × 1 k-point sampling was used for CoP(100), 5 × 3 × 1 for CoP(112) and Co₂P(121), and 3 × 5 × 1 for CoP(211). In total, CoP(100) has 24 Co and 20 P atoms, in which 8 Co and 8 P were fixed, both CoP(112) and (211) has 32 Co and 32 P atoms, in which 12 Co and 12 P were fixed, Co₂P(121) has 42 Co and 21 P atoms, in which 12 Co and 6 P were fixed.

Supplemental References

- Kresse, G., and Furthmüller, J. (1996). Efficiency of ab-initio total energy calculations for metals and semiconductors using a plane-wave basis set. *J. Comp. Mater. Sci.* 6, 15-50.
- Kresse, G., and Furthmüller, J. (1996). Efficient iterative schemes for ab initio total-energy calculations using a plane-wave basis set. *Phys. Rev. B* 54, 11169-11186.
- Kresse, G., and Joubert, D. (1999). From ultrasoft pseudopotentials to the projector augmented-wave method. *Phys. Rev. B* 59, 1758-1775.

Blöchl, P. E. (1994). Projector augmented-wave method. *Phys. Rev. B* *50*, 17953-17979.

Perdew, J. P., Burke, K., and Ernzerhof, M. (1996). Generalized Gradient Approximation Made Simple. *Phys. Rev. Lett.* *77*, 3865-3868.

Yang, F., Chen, Y., Cheng, G., Chen, S., and Luo, W. (2017). Ultrathin nitrogen-doped carbon coated with CoP for efficient hydrogen evolution. *ACS Catal.* *7*, 3824-3831.

Zhang, X., Gu, W., and Wang, E. (2017). Wire-on-flake heterostructured ternary $\text{Co}_{0.5}\text{Ni}_{0.5}\text{P}/\text{CC}$: an efficient hydrogen evolution electrocatalyst. *J. Mater. Chem. A* *5*, 982-987.

Silva, R., Voiry, D., Chhowalla, M., and Asefa, T. (2013). Efficient metal-free electrocatalysts for oxygen reduction: polyaniline-derived N- and O-doped mesoporous carbons. *J. Am. Chem. Soc.* *135*, 7823-7826.

Pan, Y., Sun, K., Liu, S., Cao, X., Wu, K., Cheong, W. -C., Chen, Z., Wang, Y., Li, Y., Liu, Y., Wang, D., Peng, Q., Chen, C., and Li, Y. (2018). Core-shell ZIF-8@ZIF-67-derived CoP nanoparticle-embedded N-doped carbon nanotube hollow polyhedron for efficient overall water splitting. *J. Am. Chem. Soc.* *140*, 2610-2618.

Ji, L., Wang, J., Teng, X., Meyer, T. J., and Chen, Z. (2020). CoP Nanoframes as bifunctional electrocatalysts for efficient overall water splitting. *ACS Catal.* *10*, 412-419.

Tan, Y., Wang, H., Liu, P., Cheng, C., Zhu, F., Hirata, A., and Chen, M. (2016). 3D nanoporous metal phosphides toward high-efficiency electrochemical hydrogen production. *Adv. Mater.* *28*, 2951-2955.

Wu, J., Wang, D., Wan, S., Liu, H., Wang, C., and Wang, X. (2019). An efficient cobalt phosphide electrocatalyst derived from cobalt phosphonate complex for all-pH hydrogen evolution reaction and overall water splitting in alkaline solution. *Small* *15*, 1900550.

Chai, L., Hu, Z., Wang, X., Xu, Y., Zhang, L., Li, T. -T., Hu, Y., Qian, J., and Huang, S. (2020). Stringing bimetallic metal-organic framework-derived cobalt phosphide composite for high-efficiency overall water splitting. *Adv. Sci.* *7*, 1903195.

Huang, X., Xu, X., Li, C., Wu, D., Cheng, D., and Cao, D. (2019). Vertical CoP nanoarray wrapped by N,P-doped carbon for hydrogen evolution reaction in both acidic and alkaline conditions. *Adv. Energy Mater.* *9*, 1803970.

Ma, J., Wang, M., Lei, G., Zhang, G., Zhang, F., Peng, W., Fan, X., and Li, Y. (2018). Polyaniline derived N-doped carbon-coated cobalt phosphide nanoparticles deposited on N-doped graphene as an efficient electrocatalyst for hydrogen evolution reaction. *Small* *14*, 1702895.

Li, H., Zhao, X., Liu, H., Chen, S., Yang, X., Lv, C., Zhang, H., She, X., and Yang, D. (2018). Sub-1.5 nm ultrathin CoP nanosheet aerogel: efficient electrocatalyst for hydrogen evolution reaction at all pH values. *Small* *14*, 1802824.

Chen, L., Zhang, Y., Wang, H., Wang, Y., Li, D., and Duan, C. (2018). Cobalt layered double hydroxides derived CoP/Co₂P hybrids for electrocatalytic overall water splitting. *Nanoscale* *10*, 21019-21024.

Yang, F., Chen, Y., Cheng, G., Chen, S., and Luo, W. (2017). Ultrathin nitrogen-doped carbon coated with CoP for efficient hydrogen evolution. *ACS Catal.* *7*, 3824-3831.

Zhang, T. -Q., Liu, J., Huang, L. -B., Zhang, X. -D., Sun, Y. -G., Liu, X. -C., Bin, D. -S., Chen, X., Cao, A. -M., Hu, J. -S., and Wan, L. -J. (2017). Microbial-phosphorus-enabled synthesis of phosphide nanocomposites for efficient electrocatalysts. *J. Am. Chem. Soc.* *139*, 11248-11253.

Tian, J., Liu, Q., Asiri, A. M., and Sun, X. (2014). Self-supported nanoporous cobalt phosphide nanowire arrays: an efficient 3D hydrogen-evolving cathode over the wide range of pH 0-14. *J. Am. Chem. Soc.* *136*, 7587-7590.

Popczun, E. J., Read, C. G., Roske, C. W., Lewis, N. S., and Schaak, R. E. (2014). Highly active electrocatalysis of the hydrogen evolution reaction by cobalt phosphide nanoparticles. *Angew. Chem., Int. Ed.* *53*, 5427-5430.

Mo, Q., Zhang, W., He, L., Yu, X., and Gao, Q. (2019). Bimetallic $\text{Ni}_{2-x}\text{Co}_x\text{P}/\text{N}$ -doped carbon nanofibers: solid-solution-alloy engineering toward efficient hydrogen evolution. *Appl. Catal. B Environ.* *244*, 620-627.

Lin, Y., Sun, K., Liu, S., Chen, X., Cheng, Y., Cheong, W. -C., Chen, Z., Zheng, L., Zhang, J., Li, X., Pan, Y., and Chen, C. (2019). Construction of CoP/NiCoP nanotadpoles heterojunction interface for wide pH hydrogen evolution electrocatalysis and supercapacitor. *Adv. Energy Mater.* *9*, 1901213.

Boppella, R., Tan, J., Yang, W., and Moon, J. (2019). Homologous CoP/NiCoP heterostructure on N-doped carbon for highly efficient and pH-universal hydrogen evolution electrocatalysis. *Adv. Funct. Mater.* *29*, 1807976.

Wang, X., Chen, Y., Yu, B., Wang, Z., Wang, H., Sun, B., Li, W., Yang, D., and Zhang, W. (2019). Hierarchically porous W-doped CoP nanoflake arrays as highly efficient and stable electrocatalyst for pH-universal hydrogen evolution. *Small* *15*, 1902613.

Liu, T., Ma, X., Liu, D., Hao, S., Du, G., Ma, Y., Asiri, A. M., and Sun, X. (2017). Mn doping of CoP nanosheets array: an efficient electrocatalyst for hydrogen evolution reaction with enhanced activity at all pH values. *ACS Catal.* *7*, 98-102.

Li, G., Yu, J., Jia, J., Yang, L., Zhao, L., Zhou, W., and Liu, H. (2018). Cobalt-cobalt phosphide nanoparticles@nitrogen-phosphorus doped carbon/graphene derived from cobalt ions adsorbed saccharomycete yeasts as an efficient, stable, and large-current-density electrode for hydrogen evolution reactions. *Adv. Funct. Mater.* *28*, 1801332.

Ma, F. -X., Xu, C. -Y., Lyu, F., Song, B., Sun, S. -C., Li, Y. Y., Lu, J., and Zhen, L., (2019). Construction of FeP hollow nanoparticles densely encapsulated in carbon nanosheet frameworks for efficient and durable electrocatalytic hydrogen production. *Adv. Sci.* *6*, 1801490.

Han, S., Feng, Y., Zhang, F., Yang, C., Yao, Z., Zhao, W., Qiu, F., Yang, L., Yao, Y., Zhuang, X., and Feng, X. (2015). Metal-phosphide-containing porous carbons derived from an ionic-polymer framework and applied as highly efficient electrochemical catalysts for water splitting. *Adv. Funct. Mater.* *25*, 3899-3906.

Chen, J., Liu, J., Xie, J. -Q., Ye, H., Fu, X. -Z., Sun, R., and Wong, C. -P. (2019). Co-Fe-P nanotubes electrocatalysts derived from metal-organic frameworks for efficient hydrogen evolution reaction under wide pH range. *Nano Energy* *56*, 225-233.

Wang, M. -Q., Ye, C., Liu, H., Xu, M. and Bao, S. -J. (2018). Nanosized metal phosphides embedded in nitrogen-doped porous carbon nanofibers for enhanced hydrogen evolution at all pH values. *Angew. Chem. Int. Ed.* *57*, 1963-1967.

Lu, X. F., Yu, L., and Lou, X. W. (2019), Highly crystalline Ni-doped FeP/carbon hollow nanorods as all-pH efficient and durable hydrogen evolving electrocatalysts. *Sci. Adv.* *5*, eaav6009.

Huang, Z., Chen, Z., Chen, Z., Lv, C., Meng, H. and Zhang, C. (2014). Ni₁₂P₅ nanoparticles as an efficient catalyst for hydrogen generation via electrolysis and photoelectrolysis. *ACS Nano* *8*, 8121-8129.

Wang, X., Li, W., Xiong, D., Petrovykh, D. Y., and Liu, L. (2016). Bifunctional nickel phosphide nanocatalysts supported on carbon fiber paper for highly efficient and stable overall water splitting. *Adv. Funct. Mater.* *26*, 4067-4077.

Wang, R., Dong, X. -Y., Du, J., Zhao, J. -Y., Zang, S. -Q. (2018). MOF-derived bifunctional Cu₃P nanoparticles coated by a N,P-codoped carbon shell for hydrogen evolution and oxygen reduction. *Adv. Mater.* *30*, 1703711.

Ge, R., Huo, J., Liao, T., Liu, Y., Zhu, M., Li, Y., Zhang, J., and Li, W. (2020). Hierarchical molybdenum phosphide coupled with carbon as a whole pH-range electrocatalyst for hydrogen evolution reaction. *Catal. B Environ.* *260*, 118196.

Li, G., Sun, Y., Rao, J., Wu, J., Kumar, A., Xu, Q. N., Fu, C., Liu, E., Blake, G. R., Werner, P., Shao, B., Liu, K., Parkin, S., Liu, X., Fahlman, M., Liou, S. -C., Auffermann, G., Zhang, J., Felsler, C., and Feng, X. (2018). Carbon-tailored semimetal MoP as an efficient hydrogen evolution electrocatalyst in both alkaline and acid media. *Adv. Energy Mater.* *8*, 1801258.

Zhang, X., Yu, X., Zhang, L., Zhou, F., Liang, Y., and Wang, R. (2018). Molybdenum phosphide/carbon nanotube hybrids as pH-universal electrocatalysts for hydrogen evolution reaction. *Adv. Funct. Mater.* *28*, 1706523.

Zhang, X., Zhou, F., Pan, W., Liang, Y., and Wang, R. (2018). General construction of molybdenum-based nanowire arrays for pH-universal hydrogen evolution electrocatalysis. *Adv. Funct. Mater.* *28*, 1804600.

Weng, B., Grice, C. R., Meng, W., Guan, L., Xu, F., Yu, Y., Wang, C., Zhao, D., and Yan, Y. (2018). Metal-organic framework-derived CoWP@C composite nanowire electrocatalyst for efficient water splitting. *ACS Energy Lett.* *3*, 1434-1442.

Wang, X. -D., Xu, Y. -F., Rao, H. -S., Xu, W. -J., Chen, H. -Y., Zhang, W. -X., Kuang, D. -B., and Su, C. -Y. (2016). Novel porous molybdenum tungsten phosphide hybrid nanosheets on carbon cloth for efficient hydrogen evolution. *Energy Environ. Sci.* *9*, 1468-1675.

Su, L., Cui, X., He, T., Zeng, L., Tian, H., Song, Y., Qi, K., and Xia, B. Y. (2019). Surface reconstruction of cobalt phosphide nanosheets by electrochemical activation for enhanced hydrogen evolution in alkaline solution. *Chem. Sci.* *10*, 2019-2024.

Xu, K., Cheng, H., Lv, H., Wang, J., Liu, L., Liu, S., Wu, X., Chu, W., Wu, C., and Xie, Y. (2018). Controllable surface reorganization engineering on cobalt phosphide nanowire arrays for efficient alkaline hydrogen evolution reaction. *Adv. Mater.* *30*, 1703322.

Li, H., Li, Q., Wen, P., Williams, T. B., Adhikari, S., Dun, C., Lu, C., Itanze, D., Jiang, L., Carroll, D. L., Donati, G. L., Lundin, P. M., Qiu, Y., and Geyer, S. M. (2018). Colloidal cobalt phosphide nanocrystals as trifunctional electrocatalysts for overall water splitting powered by a zinc-air battery. *Adv. Mater.* *30*, 1705796.

Zhang, Y., Gao, L., Hensen, E. J. M., and Hofmann, J. P. (2018). Evaluating the stability of Co₂P electrocatalysts in the hydrogen evolution reaction for both acidic and alkaline electrolytes. *ACS Energy Lett.* *3*, 1360-1365.

Wang, J., Yang, W., and Liu, J. (2016). CoP₂ nanoparticles on reduced graphene oxide sheets as a super-efficient bifunctional electrocatalyst for full water splitting. *J. Mater. Chem. A* *4*, 4686-4690.

Zhou, D., He, L., Zhu, W., Hou, X., Wang, K., Du, G., Zheng, C., Sun, X., and Asiri, A. M. (2016). Interconnected urchin-like cobalt phosphide microspheres film for highly efficient electrochemical hydrogen evolution in both acidic and basic media. *J. Mater. Chem. A* *4*, 10114-10117.

Jiang, N., You, B., Sheng, M., and Sun, Y. (2015). Electrodeposited cobalt-phosphorous-derived films as competent bifunctional catalysts for overall water splitting. *Angew. Chem., Int. Ed.* *54*, 6251-6254.

Zhang, R., Huang, J., Chen, G., Chen, W., Song, C., Li, C., and Ostrikov, K. (2019). In situ engineering bi-metallic phosphonitride bi-functional electrocatalysts for overall water splitting. *Appl. Catal. B Environ.* *254*, 414-423.

Fu, Q., Wu, T., Fu, G., Gao, T., Han, J., Yao, T., Zhang, Y., Zhong, W., Wang, X., and Song, B. (2018). Skutterudite-type ternary Co_{1-x}Ni_xP₃ nanoneedle array electrocatalysts for enhanced hydrogen and oxygen evolution. *ACS Energy Lett.* *3*, 1744-1752.

Tang, C., Zhang, R., Lu, W., He, L., Jiang, X., Asiri, A. M., and Sun, X. (2017). Fe-doped CoP nanoarray: a monolithic multifunctional catalyst for highly efficient hydrogen generation. *Adv. Mater.* *29*, 1602441.

Feng, H., Tang, L., Zeng, G., Yu, J., Deng, Y., Zhou, Y., Wang, J., Feng, C., Luo, T., and Shao, B. (2020). Electron density modulation of Fe_{1-x}Co_xP nanosheet arrays by iron incorporation for highly efficient water splitting. *Nano Energy* *67*, 104174.

Lian, Y., Sun, H., Wang, X., Qi, P., Mu, Q., Chen, Y., Ye, J., Zhao, X., Deng, Z., and Peng, Y. (2019). Carved nanoframes of cobalt-iron bimetal phosphide as a bifunctional electrocatalyst for efficient overall water splitting. *Chem. Sci.* *10*, 464-474.

Lin, R., Lei, H., Ruan, D., Jiang, K., Yu, X., Wang, Z., Mai, W. and Yan, H. (2019). Solar-powered overall water splitting system combining metal-organic frameworks derived bimetallic nanohybrids based electrocatalysts and one organic solar cell. *Nano Energy* 56, 82-91.

You, B., Jiang, N., Sheng, M., Bhushan, M. W., and Sun, Y. (2016). Hierarchically porous urchin-like Ni₂P superstructures supported on nickel foam as efficient bifunctional electrocatalysts for overall water splitting. *ACS Catal.* 6, 714-721.

Chu, S., Chen, W., Chen, G., Huang, J., Zhang, R., Song, C., Wang, X., and Li, C. (2019). Holey Ni-Cu phosphide nanosheets as a highly efficient and stable electrocatalyst for hydrogen evolution. *Appl. Catal. B Environ.* 243, 537-545.

Ma, Y. -Y., Wu, C. -X., Feng, X. -J., Tan, H. -Q., Yan, L. -K., Liu, Y., Kang, Z. -H., Wang, E. -B., and Li, Y. -G., (2017). Highly efficient hydrogen evolution from seawater by a low-cost and stable CoMoP@C electrocatalyst superior to Pt/C. *Energy Environ. Sci.* 10, 788-798.

Yu, L., Mishra, I. K., Xie, Y., Zhou, H., Sun, J., Zhou, J., Ni, Y., Luo, D., Yu, F., Yu, Y., Chen, S., and Ren, Z. (2018). Ternary Ni_{2(1-x)}Mo_{2x}P nanowire arrays toward efficient and stable hydrogen evolution electrocatalysis under large-current-density. *Nano Energy* 53, 492-500.

Cao, E., Chen, Z., Wu, H., Yu, P., Wang, Y., Xiao, F., Chen, S., Du, S., Xie, Y., Wu, Y., and Ren, Z. (2020). Boron-induced electronic-structure reformation of CoP nanoparticles drives enhanced pH-universal hydrogen evolution. *Angew. Chem. Int. Ed.* 59, 4154-4160.

Tabassum, H., Guo, W., Meng, W., Mahmood, A., Zhao, R., Wang, Q., and Zou, R. (2017). Hydrogen evolution: metal-organic frameworks derived cobalt phosphide architecture encapsulated into B/N co-doped graphene nanotubes for all pH value electrochemical hydrogen evolution. *Adv. Energy Mater.* 7, 1601671.

Huang, J., Li, Y., Xia, Y., Zhu, J., Yi, Q., Wang, H., Xiong, J., Sun, Y. and Zou, G. (2017). Flexible cobalt phosphide network electrocatalyst for hydrogen evolution at all pH values. *Nano Res.* 10, 1010-1020.

Pu, Z., Liu, Q., Jiang, P., Asiri, A. M., Obaid, A. Y., and Sun, X. (2014). CoP Nanosheet arrays supported on a Ti plate: an efficient cathode for electrochemical hydrogen evolution. *Chem. Mater.* 26, 4326-4329.

Gu, S., Du, H., Asiri, A. M., Sun, X., and Li, C. M. (2014). Three-dimensional interconnected network of nanoporous CoP nanowires as an efficient hydrogen evolution cathode. *Phys. Chem. Chem. Phys.* 16, 16909-16913.

Men, Y., Li, P., Yang, F., Cheng, G., Chen, S., and Luo, W. (2019). Nitrogen-doped CoP as robust electrocatalyst for high-efficiency pH-universal hydrogen evolution reaction. *Appl. Catal. B Environ.* 253, 21-27.

Xiao, X., Tao, L., Li, M., Lv, X., Huang, D., Jiang, X., Pan, H., Wang, M., and Shen, Y. (2018). Electronic modulation of transition metal phosphide via doping as efficient and pH-universal electrocatalysts for hydrogen evolution reaction. *Chem. Sci.* 9, 1970-1975.

Wu, R., Xiao, B., Gao, Q., Zheng, Y. -R., Zheng, X. -S., Zhu, J. -F., Gao, M. -R., and Yu, S. -H. (2018). A janus nickel cobalt phosphide catalyst for high-efficiency neutral-pH water splitting. *Angew. Chem. Int. Ed.* 57, 15445-15449.

Li, J., Yan, M., Zhou, X., Huang, Z. -Q., Xia, Z., Chang, C. -R., Ma, Y., and Qu, Y. (2016). Mechanistic insights on ternary Ni_{2-x}Co_xP for hydrogen evolution and their hybrids with graphene as highly efficient and robust catalysts for overall water splitting. *Adv. Funct. Mater.* 26, 6785-6796.

Han, A., Chen, H., Zhang, H., Sun, Z., and Du, P. (2016). Ternary metal phosphide nanosheets as a highly efficient electrocatalyst for water reduction to hydrogen over a wide pH range from 0 to 14. *J. Mater. Chem. A* 4, 10195-10202.

Pu, Z., Amiin, I. S., Zhang, C., Wang, M., Kou, Z., and Mu, S. (2017). Phytic acid-derivative transition metal phosphides encapsulated in N,P-codoped carbon: an efficient and durable hydrogen evolution electrocatalyst in a wide pH range. *Nanoscale* 9, 3555-3560.

Liang, K., Pakhira, S., Yang, Z., Nijamudheen, A., Ju, L., Wang, M., Aguirre-Velez, C. I., Sterbinsky, G. E., Du, Y., Feng, Z., Mendoza-Cortes, J. L., and Yang, Y. (2019). *ACS Catal.* 9, 651-659.

Xie, X., Song, M., Wang, L., Engelhard, M. H., Luo, L., Miller, A., Zhang, Y., Du, L., Pan, H., Nie, Z., Chu, Y., Estevez, L., Wei, Z., Liu, H., Wang, C., Li, D., and Shao, Y. (2019). Electrocatalytic hydrogen evolution in neutral pH solutions: dual-phase synergy. *ACS Catal.* 9, 8712-8718.